

**SPIN-ORBIT TORQUE MEASUREMENTS IN HEAVY
METAL/FERROMAGNET HETEROSTRUCTURES USING THE
MAGNETO-OPTIC KERR EFFECT**

by

Halise Celik

A dissertation submitted to the Faculty of the University of Delaware in partial fulfillment of the requirements for the degree of Doctor of Philosophy in Physics

Spring 2018

© 2018 Halise Celik
All Rights Reserved

**SPIN-ORBIT TORQUE MEASUREMENTS IN HEAVY
METAL/FERROMAGNET HETEROSTRUCTURES USING THE
MAGNETO-OPTIC KERR EFFECT**

by

Halise Celik

Approved:

Edmund R. Nowak, Ph.D.
Chair of the Department of Physics and Astronomy

Approved:

George H. Watson, Ph.D.
Dean of the College of Arts and Sciences

Approved:

Ann L. Ardis, Ph.D.
Senior Vice Provost for Graduate and Professional Education

I certify that I have read this dissertation and that in my opinion it meets the academic and professional standard required by the University as a dissertation for the degree of Doctor of Philosophy.

Signed:

John Q. Xiao, Ph.D.
Professor in charge of dissertation

I certify that I have read this dissertation and that in my opinion it meets the academic and professional standard required by the University as a dissertation for the degree of Doctor of Philosophy.

Signed:

Virginia O. Lorenz, Ph.D.
Member of dissertation committee

I certify that I have read this dissertation and that in my opinion it meets the academic and professional standard required by the University as a dissertation for the degree of Doctor of Philosophy.

Signed:

Edmund R. Nowak, Ph.D.
Member of dissertation committee

I certify that I have read this dissertation and that in my opinion it meets the academic and professional standard required by the University as a dissertation for the degree of Doctor of Philosophy.

Signed:

Lars Gundlach, Ph.D.
Member of dissertation committee

ACKNOWLEDGMENTS

First and foremost I would like to thank my advisors Prof. John Q. Xiao and Prof. Virginia (Gina) O. Lorenz for their guidance and support during my Ph.D experience. Prof. Xiao, I have enjoyed working in a research environment that stimulates original thinking and initiative that you have created. Your unwavering enthusiasm and excitement in physics will continue to be a mentor to me through my future career. Gina, it has been an honor and I have been truly fortunate to be able to work with you. It is due to your immense knowledge, valuable guidance, continuous support, and ever-friendly nature that I am able to complete my Ph.D study. Your motivational speeches and patience helped me a lot during tough times and I am very grateful for that. I am also thankful for the excellent example you have provided as a successful woman physicist and a professor.

I would like to express my sincere gratitude to Dr. Xin Fan for his tremendous contribution to this work. I appreciate all his contributions of ideas, time and discussions. I would like to acknowledge the following people in the department of Physics and Astronomy: Dr. Matthew DeCamp, Dr. Stephen Barr, Dr. Qaisar Shafi, Dr. Edmund Nowak, Dr. Lars Gundlach, Maura Perkins and Debra Morris for their help and kindness.

For helpful comments, discussions and motivational ideas I would like to thank my friends Ferda Yilmaz, Ozlem Batan and Harsha Kannan. Also past and present group members and grad students I have had the pleasure to work with are Dr. Seth Meiselman, Jamy Moreno, Dr. Fatih Kandaz, Dr. Jun Wu, Dr. Tao Wang, Dr.

Yunpeng Chen, Dr. Asif Warsi, Rasoul Barri, Kevin Haughey. They have been a source of friendships as well as good advice and collaboration.

I would like to thank my family: my parents, my brother and sisters and my encouraging, caring, patient husband for loving and supporting me.

TABLE OF CONTENTS

LIST OF TABLES	x
LIST OF FIGURES	xi
ABSTRACT	xx
Chapter	
1 INTRODUCTION	1
1.1 Introduction to Spintronics	1
1.2 Giant Magnetoresistance and Spin Valves	3
1.3 Magnetic Tunnel Junctions	5
1.4 Micromagnetic Modeling and the Dynamic Equation	8
1.4.1 Micromagnetic Model	8
1.4.1.1 Exchange Energy	10
1.4.1.2 Anisotropy Energy	11
1.4.1.2.1 Magnetocrystalline Anisotropy	12
1.4.1.2.2 Shape or Magnetostatic Anisotropy	13
1.4.1.2.3 Magnetoelastic Anisotropy	13
1.4.1.3 Zeeman Energy	14
1.4.2 The Landau–Lifshitz–Gilbert Equation	14
1.5 Spin Transfer Torque	17
1.6 Spin Hall Effect and Rashba Effect	22
REFERENCES	26
2 FABRICATION, CHARACTERIZATION AND EXPERIMENTAL TECHNIQUES	37
2.1 Fabrication Techniques	37
2.1.1 Magnetron Sputtering Thin Film Deposition	37

2.1.2	Photolithography	39
2.1.3	Ion Beam Etching	42
2.2	Characterization and Experimental Techniques	42
2.2.1	X-ray Diffraction	42
2.2.2	Vibrating Sample Magnetometer	43
2.2.3	Scanning Electron Microscope	44
2.2.4	Electrical Transport Measurements	45
2.2.5	Magneto-Optic Kerr Effect	46
2.2.5.1	Background	46
2.2.5.2	Theory of the Magneto-Optic Kerr Effect	49
REFERENCES	60
3	QUANTIFYING INTERFACE AND BULK CONTRIBUTIONS TO SPIN-ORBIT TORQUE IN MAGNETIC BILAYERS	63
3.1	Introduction	64
3.2	Sample Fabrication	65
3.3	Detection of DT and FT	66
3.3.1	Detection of DT with the Polar MOKE	67
3.3.1.1	Extraction of DT from Polar MOKE	70
3.3.2	Detection of FT with Second-order Planar Hall Effect	76
3.3.3	Detection of FT with Longitudinal MOKE	79
3.3.4	FM Layer Thickness Dependence of DT and FT	82
3.3.5	Determination of the Interface Contribution	85
3.3.6	Summary	88
REFERENCES	89
4	ALL-OPTICAL VECTOR-RESOLVED MEASUREMENT OF SPIN- ORBIT-INDUCED TORQUES USING BOTH POLAR AND QUADRATIC MAGNETO-OPTIC KERR EFFECTS	92
4.1	Introduction	92
4.2	Sample Fabrication	93
4.3	Determination of Polar and Quadratic MOKE signals	93
4.4	Experimental Results of DT and FT with Polar and Quadratic MOKE	100
4.4.1	Laser Polarization Angle Dependence of MOKE	106

4.5	Experimental Detection of DT and FT with ST-FMR	107
4.6	Comparison of Experimental Data on DT and FT by MOKE and ST-FMR.....	108
4.7	Summary	111
REFERENCES		113
5	QUANTIFYING THE ANGULAR DEPENDENCE OF SPIN-ORBIT TORQUES IN HM/FM/METAL-OXIDE TRILAYERS WITH PERPENDICULAR MAGNETIC ANISOTROPY	114
5.1	Introduction	115
5.2	Sample Fabrication and the Optimization of PMA in Ta/CoFeB/MgO Trilayers.....	116
5.3	Magnetization Reorientation due to the SOTs in Multilayer Thin Films with PMA	119
5.3.1	External Magnetic Field Parallel to the Current.....	121
5.3.2	External Magnetic Field Perpendicular to the Current.....	122
5.4	Detection of DT and FT with the Adiabatic Harmonic Hall Technique in Ta/CoFeB/MgO trilayers with PMA.....	124
5.5	Detection of DT and FT with MOKE in Ta/CoFeB/MgO trilayers with PMA	132
5.6	Summary	138
REFERENCES		140
6	VECTOR-RESOLVED MAGNETO-OPTIC KERR EFFECT MEASUREMENTS OF SPIN-ORBIT TORQUE	142
6.1	Introduction	142
6.2	Separation of MOKE signals.....	143
6.3	Measurement Setup and Determination of DT and FT with Vector-Resolved MOKE	148
6.4	Summary	154
REFERENCES		156
7	CONCLUSIONS	157

Appendix

A	SIGNAL OUTPUT CALCULATED USING MODIFIED REFLECTIVITIES FOR A MAGNETIC MATERIAL AND JONES MATRICES FOR OPTICAL ELEMENTS	160
B	CURRENT-INDUCED MAGNETIZATION REORIENTATION.....	165
C	USEFUL TIPS FOR MOKE MEASUREMENT SETUP.....	171
D	REPRINT PERMISSION LETTERS.....	172

LIST OF TABLES

Table 4.1: List of Jones matrices/vectors used in this calculation. The initial polarization is set along the x -axis. The Jones matrices M in the table for half wave plate, quarter wave plate and magnetic sample are assuming the principle axis (fast axis of the wave plate or in-plane magnetization direction of the magnetic sample) is along the x -axis. The matrices with arbitrary principle axis can be deduced as $R[\theta]MR[-\theta]$, where $R[\theta] = \begin{bmatrix} \cos \theta & -\sin \theta \\ \sin \theta & \cos \theta \end{bmatrix}$ and θ is the relative angle between the principle axis and the x -axis. The factor ξ in the Jones Matrix for the magnetic sample captures the reflection loss, which does not affect the polarization change. 97

LIST OF FIGURES

Figure 1.1:	Giant magnetoresistance effect: A triple-layer film in which a non-magnetic normal metal is sandwiched between two ferromagnetic metals. (a) FM1 parallel to FM2 → low resistance, (b) FM1 antiparallel to FM2 → high resistance.	4
Figure 1.2:	Illustration of TMR in a MTJ comprised of two ferromagnetic layers, FM1 and FM2, separated by an insulating barrier I. (a) For FM1 parallel to FM2, spin up electrons tunnel from majority to majority band and spin down electrons tunnel from minority to minority band → low resistance. (b) For FM1 antiparallel to FM2, spin up electrons tunnel from majority to minority band and spin down electrons tunnel from minority to majority band → high resistance.	6
Figure 1.3:	Illustration of magnetization precession (a) without damping (b) with damping.	17
Figure 1.4:	Illustration of spin transfer torque. Electron passing through a pinned magnetic layer get spin polarized. By conservation of angular momentum, the transverse spin angular momentum is transferred to the free magnetic layer.	18
Figure 1.5:	Illustration of the writing process in STT-MRAM. Reversing the current direction reverses the torque direction [51].	20
Figure 1.6:	Schematics of (a) the ordinary Hall effect: in the presence of an external field, current passing through a normal metal creates a voltage; and (b) the spin Hall effect: due to spin-orbit interaction, current passing through a normal metal creates a spin current.	23
Figure 1.7:	(a) Charge current through HM creates spin current through spin Hall effect. (b) Charge current through HM/FM interface creates spin polarization. Both mechanisms induce an effective field and a torque on the FM [52].	24
Figure 2.1:	Schematic of thin-film magnetron sputtering. Argon is ionized and accelerated to a target. After collision, target atoms are ejected and travel to the substrate where they form a thin film [72].	38

Figure 2.2:	(a) Positive photolithography including the steps of spin coating, baking, UV light exposure with photomask and developing. (b) Negative photolithography including the steps of spin coating, baking, UV light exposure with photomask, baking, UV light exposure without photomask and developing.....	40
Figure 2.3:	The detection mechanism of a vibrating sample magnetometer: a sample vibrates vertically with a constant frequency and an electromagnet provides a horizontal magnetic field [79]......	43
Figure 2.4:	A four-probe station with Hall bar structure. Two pairs of Helmholtz coils, big and small, produce magnetic fields in x and y directions, respectively.....	45
Figure 2.5:	(a) A schematic of the magneto-optic Faraday (transmission) and Kerr (reflection) effects. (b) Linearly polarized light (left plot) transforms into rotated elliptically polarized light (right plot) due to the magneto-optic effects.	48
Figure 2.6:	Three principle MOKE geometries. Polar: The magnetic field vector is perpendicular to the sample surface and parallel to the plane of incidence. Longitudinal: The magnetic field vector is parallel to both the sample surface and the plane of incidence. Transverse: The magnetic field vector parallel to the sample surface but perpendicular to the plane of incidence.....	49
Figure 2.7:	Linearly polarized light decomposes into LCP and RCP. The amplitude and the phase of the LCP and RCP changes after reflection, resulting in a rotated elliptical polarization.	52
Figure 2.8:	Light is incident from medium 0 to medium 1. The angle of incidence θ_0 and refraction θ_1 are related by Snell's law.....	55
Figure 2.9:	Sketch of the energy levels with exchange and spin-orbit interaction in a bulk ferromagnet showing the electric dipole transitions for left- and right-circular polarization.....	57
Figure 2.10:	Sketch of the energy levels without exchange interaction in a bulk paramagnet, showing the electric dipole transitions for left- and right-circular polarization.....	58

Figure 3.1: (a) Experimental setup for using polar MOKE to detect DT. A lock-in amplifier supplies an ac current through the sample along the z direction, which generates FT and DT that rotate the magnetization in-plane and out-of-plane from the xz plane, respectively. The reflected laser polarization changes with the magnetization of the sample because of MOKE. The change in the polarization is converted to a voltage signal through a series of optical components and a balanced detector. The voltage signal is detected by the same lock-in amplifier. (b) An example experimental result from Ti(1)/Co₄₀Fe₄₀B₂₀(0.85)/Pt(5) with a 12 mA bias current and 5 mW laser power. The inset is the magnetization hysteresis of the same sample..... 68

Figure 3.2 (a) The linear bias current dependence of the MOKE response The laser power is kept at 5 mW with a beam radius of 2 mm, which corresponds to a power density of $4 \times 10^8 \text{ W / m}^2$. (b) The linear laser power dependence of the MOKE response. The bias current is kept at 10 mA, which corresponds to a current density of $4 \times 10^{10} \text{ A / m}^2$ 69

Figure 3.3: (a) Measured offset of the line scan $\Delta V = V[+H, x] + V[-H, x]$ (top, black squares) and the corresponding numerical simulation (bottom, red line) based on Eq. (3.7). (b) Plot of the y-axis values of the numerical simulation and the measured data against one another (black squares). The parameters in Eq. (3.7) are calibrated from a linear least-squares fit (red line). For this example curve, we find $\eta I_c / w = 45.5 \pm 1.2 \mu V$. (c) Measured DT signal from line scan $\Delta V = V[+H, x] - V[-H, x]$ (top, black squares) and the corresponding numerical simulation (bottom, red line) based on Eq. (3.8). (d) Data and simulation plotted against each other (black squares) and linear least-squares fit (red line), which gives the parameter for DT as $\eta h_{SOT} = 166 \pm 3 \mu V$. Therefore, the DT coefficient is determined to be

$$\beta_T = \frac{h_{DT}}{j_{Pt}} = \frac{h_{DT}}{I_c / w} d_{Pt} = 18.3 \pm 0.7 \text{ nm} \dots\dots\dots 72$$

Figure 3.4: Representative DT measurement using polar MOKE for Ti/CoFeB/Pt, Ti/CoFeB/Cu, and CoFeB/Ta samples. The Ti/CoFeB/Cu (inset in the middle panel) shows very little DT signal, two orders smaller than those measured in CoFeB/Pt and CoFeB/Ta. The CoFeB/Pt and CoFeB/Ta has opposite sign to the DT, which is consistent with the opposite spin Hall angles of Pt and Ta. 74

- Figure 3.5: Two-dimensional raster scanning of the DT. (a) Image of the device under measurement. The imaging area is $100\ \mu\text{m} \times 100\ \mu\text{m}$ with a step size of $5\ \mu\text{m}$, illustrated by the green dashed line. (b) 2d imaging of the laser reflectivity as the laser scans the region. The area with Au, Si/SiO₂ and Ti/CoFeB/Pt has different reflectivity and can therefore be distinguished. (c) 2d imaging of the DT by taking the difference between the voltage response at positive saturated field and negative saturated field. In the middle regime, the magnitude is relatively uniform at $160 \pm 5\ \mu\text{V}$. The smearing of the boundary is due to the finite size of the laser beam diameter ($4\ \mu\text{m}$). (d) 2d imaging of the offset signal due to the out-of-plane Oersted field obtained by taking the average of the voltage response at positive saturated field and negative saturated field. As expected, the magnetization reorientation due to the out-of-plane Oersted field points toward opposite directions at the left side and right side of the sample. In the middle regime of the sample ($\sim 30\ \mu\text{m}$ vertical span), the distribution is reasonably uniform. 75
- Figure 3.6: (a) Experimental setup for using the second-order PHE to detect the in-plane magnetization reorientation and the FT. A transverse field h_{cal} is applied to calibrate the response of the second order PHE voltage in order to quantify the FT. (b) Example measured second-order PHE curve of the Ti(1)/CoFeB(0.75)/Pt(5) under several calibration field strengths. The applied dc current is 50 mA. 77
- Figure 3.7: (a) Linear regression algorithm to extract the FT. The x-axis is obtained by $\Delta V_{\text{fitting}} = \Delta V(h_{\text{cal}} = -270\ \text{Am}^{-1}) - \Delta V(h_{\text{cal}} = 270\ \text{Am}^{-1})$ and y-axis is the $\Delta V(h_{\text{cal}} = 0\ \text{Am}^{-1})$ at the corresponding magnetic field. The positively saturated data and negatively saturated data are fit separately with the average slope taken as the ratio between the total current-induced field and the calibration field. The inset shows the overall curve at both saturated and unsaturated fields. (b) The linear bias current dependence of the FT indicates that the measurement is still in linear regime. 78

Figure 3.8: (a) Experimental setup for using longitudinal MOKE to detect the FT. The set-up is identical with the polar MOKE shown in Figure 3.1 (a), except that the laser is obliquely incident on the sample in the xy plane. The incident angle is set to be about 20° . (b) Measured voltage from the lock-in amplifier when passing an ac current 100 mA through the sample (500 μm in width) (black squares, top curve). The curve is asymmetric owing to the out-of-plane magnetization reorientation because of the DT. The calibration is performed by applying an ac current through a metallic wire behind the sample, which generates an Oersted field of $216 \pm 8 \text{ Am}^{-1}$ that drives the in-plane magnetization reorientation. As shown in the lower graph (red circles), the curve is symmetric since the calibration field has no torque-like term. (c) The magnetization reorientation because of the FT (top curve) and DT (bottom curve) can be separated by their different symmetries. (d) The magnitude of the FT is extracted using a linear regression algorithm by comparing the top curve in (c) and the calibration curve in (b). Only data between 50 Oe and 300 Gauss are used in the fitting, where the magnetization is well-saturated. (e) The extracted FT is linearly proportional to the bias current, suggesting that the measurement is still in the linear regime. 80

Figure 3.9: (a) Measured DT coefficient of $\text{Ti}(1)/\text{CoFeB}(x)/\text{Pt}(5)$, where x spans from 0.65 to 5.75 nm. The inset shows the $1/d_{\text{CoFeB}}$ dependence of the DT coefficients. Here the error bar of the y -axis is obtained from the linear regression. The error bar of the x -axis is because of possible misalignment in fabricating the wedge-shaped sample. (b) Measured FT coefficient of the same series of samples as in (a). The FT remains nearly zero when CoFeB is thick and increases rapidly as the CoFeB becomes thinner than 1 nm. The inset shows the DT and FT of $\text{Ti}(1)/\text{CoFeB}(x)/\text{Cu}(2)/\text{Pt}(5)$, where the direct interface between CoFeB and Pt is removed. 83

Figure 3.10: (a) Measured FT and DT coefficients in Ti(0.7)/CoFeB(0.7)/Cu(x)/Pt(5). The FT coefficient shows an increase with very thin copper insertion and then decreases as the copper layer gets thicker, while the DT coefficient shows a monotonic decay with increasing copper layer thickness. (b) The ratio between the FT and DT coefficients manifests two regimes as highlighted in the graph. In the green regime, where copper is thick enough to remove the interface effect between CoFeB and Pt, the β_{FT} / β_{DT} values are near 0.2. In the red regime, where copper is too thin to form continuous film, the β_{FT} / β_{DT} is lower suggesting that there exists an interface effect that produces a FT and DT based on a different mechanism from the effect of the nonlocal spin current.	86
Figure 4.1: Experimental set-up for the optical detection of SOTs. For detecting the current-induced DT, we use a half wave plate, HWP-2, before the sample. This is replaced by a quarter wave plate, QWP-2, for detecting the current-induced FT.	96
Figure 4.2: Current-induced polar MOKE response with three different incident laser polarizations.....	101
Figure 4.3: Separation of the out-of-plane field due to the Oersted field and the DT by the spatial symmetry and dependence on the magnetization orientation.....	103
Figure 4.4: Current-induced Kerr response with circularly polarized light and 0° linearly polarized light. The former only contains a quadratic MOKE response ($1/H_{ex}$ -like) while the latter is a superposition of a quadratic MOKE response and a polar MOKE response (which has a step-like dependence on H_{ex})......	104
Figure 4.5: MOKE data when the calibration field is applied. The red curve is the fit using $\Delta\Psi = \beta_{\text{Quadratic}} \frac{h_{\text{Cal}}}{H_{\text{ex}} + H_{\text{anis}}}$	105
Figure 4.6: MOKE coefficients plotted as a function of laser polarization. The red curve in the bottom panel is a sinusoidal fit to $\cos 2\phi_{\text{pol}}$	107

Figure 4.7:	(a) The equivalent current-generated fields corresponding to the damping-like component h_{DT} and the in-plane effective-field-like component h_{FT} normalized by the total current per unit lateral width in the bilayer. The uncertainties for the MOKE technique mostly arise from the fitting, while the uncertainties for the ST-FMR are mainly due to the determination of the microwave current. Excellent agreement is found between the MOKE and ST-FMR techniques.	109
Figure 4.8:	$\tau_{AD,SO} / A$ normalized by the estimated current per unit sample width in the Pt layer.....	110
Figure 4.9:	The h_{FT} normalized by the estimated current per unit sample width in the Pt layer.....	111
Figure 5.1:	The anomalous Hall effect hysteresis loops of three groups of samples: (a) Ta (x)/CoFeB (1.2)/MgO (3), (b) Ta (2)/CoFeB (y)/MgO (3), and (c) Ta (2)/CoFeB (1.2)/ MgO (z).	118
Figure 5.2:	The sample structure of a trilayer system with PMA and the current induced DT and FT.....	119
Figure 5.3:	A sketch of DT and FT in the $H \parallel I$ configuration for multilayer thin films with PMA.....	122
Figure 5.4:	A sketch of DT and FT in the $H \perp I$ configuration for multilayer thin films with PMA.....	123
Figure 5.5:	(a) First-order harmonic loops under different applied fields; (b) second-harmonic loops under the $H \parallel I$ and $H \perp I$ geometries.....	126
Figure 5.6:	DC polar MOKE signal as a function of the external magnetic field. ..	127
Figure 5.7:	The fitting of second-harmonic curves under (a) $H \parallel I$ and (c) $H \perp I$ geometries. The fitted values are $h_{DT} = 1.2$ Oe and $h_{FT} = 2.9$ Oe.....	128
Figure 5.8:	(a) The coefficient of damping-like torque and (b) field-like torque as a function of the polar angle of \vec{m}	130
Figure 5.9:	The fitting curves of second-harmonic voltage with different values of perpendicular anisotropy field H_p in (a) the $H \parallel I$ and (b) the $H \perp I$ configurations.....	132

Figure 5.10: Measurement of DT and FT with the MOKE technique. Calibration is done by sending an AC current through a calibration wire that applies an out-of-plane magnetic field on the sample.	134
Figure 5.11: The MOKE response with 1 mA current (1.1×10^6 A/cm ² current density in Ta) applied in the sample (black) and 1.53 Oe calibration field (red) under the $H \parallel I$ configuration.	135
Figure 5.12: The MOKE response with 1 mA current (1.1×10^6 A/cm ² current density in Ta) applied in the sample (black) and 1.53 Oe calibration field (red) under the $H \perp I$ configuration.	136
Figure 5.13: The calculated coefficient of damping-like torque (a) and field-like torque (b) as a function of the magnetization angle. Both DT and FT reach the maximum near $\theta_0 = 90^\circ$, when the magnetization lies in the film plane.....	138
Figure 6.1: Polar, longitudinal, and transverse MOKE geometries for a sample with magnetization m	144
Figure 6.2: Geometry of the optical quadrant bridge detection system. A 40 \times objective focuses light transmitted to and collimates light reflected from the sample. The reflected light is detected in spatial quadrants a , b , c , and d . By adding and subtracting signals from appropriate quadrants, one can isolate the in-plane MOKE response from the out-of-plane MOKE response.	146
Figure 6.3: Experimental setup for the optical detection of spin-orbit torques. HWP: half-wave plate, QWP: quarter-wave plate.	149
Figure 6.4: The current-induced (a) polar and (b) longitudinal response as a function of swept magnetic field H_{ext} in Py(8)/Pt(6) bilayers. The red lines are least-squares fits to a step function and to $\sim 1/H_{ext}$ for the polar and longitudinal responses, respectively.....	150

Figure 6.5: (a) Line scan result for Py(4)/Pt(6) with balanced detector. Out-of-plane equivalent spin-orbit field detected by subtracting signals taken at positive and negative saturation field. Fit function (red line) is calculated as the integration of the SOT-induced magnetization reorientation weighted by the Gaussian function that describes the spatial distribution of the laser. (b) Out-of-plane Oersted field detected by addition of signals taken at positive and negative saturation field. The fit function for the Oersted field (red line) is similarly calculated as the integration of the local magnetization reorientation weighted by the Gaussian function that describes the spatial distribution of the laser. (c), (d) Line scan results for Py(4)/Pt(6) with quadrant detectors. 152

Figure 6.6: Measured voltage from the lock-in amplifier as a function of the external magnetic field for Py(8)/Pt(6) when passing an ac current (20 mA) through the sample (black squares) and an ac current (500 mA) through a wire underneath the sample (red circles). (b) Comparison of signals in two longitudinal configurations m_y (black squares) and m_x (red circles)..... 153

Figure 6.7: (a) Effective FT spin Hall angle measured via longitudinal with quadrant detection (black squares) and quadratic (red circles) MOKE vs. permalloy thickness d_{py} . (b) Effective DT spin Hall angle measured with polar MOKE with quadrant detection (black squares) and polar MOKE without quadrant detection (red circles) vs. permalloy thickness d_{py} 154

Figure B.1: Schematic of the magnetization orientation in a stationary state under an external magnetic field \vec{H}_{ex} , anisotropy field \vec{H}_a , demagnetizing field \vec{H}_d , Oersted field \vec{h}_{oe} and the effective fields of FT $(-a/\gamma \vec{\sigma})$ and DT $(-b/\gamma (\vec{\sigma} \times \vec{m}))$ 166

ABSTRACT

Spin-orbit coupling in heavy-metal/ferromagnet (HM/FM) bilayer heterostructures has attracted considerable attention because it provides an efficient way to manipulate the magnetization with strong current-driven spin-orbit torques (SOTs), which may lead to new technologies for nonvolatile magnetic memory and logic devices. An electric current flowing through a heavy metal generates a field-like spin-orbit torque (FT) and a damping-like spin-orbit torque (DT) on the magnetization of a neighboring ferromagnet. Two mechanisms have been proposed to explain the generation of SOTs: the Rashba-Edelstein effect due to interfacial spin-orbit coupling and the spin Hall effect in the bulk of materials with strong spin-orbit coupling (SOC). Much effort has been dedicated to identifying the dominant mechanism of the SOTs; however, the underlying mechanism for the SOC-driven phenomena remained unsettled. In this thesis, we develop a sensitive SOT magnetometer based on the magneto-optic Kerr effect (MOKE) that measures the SOTs for HM/FM bilayers over a wide thickness range. We observe that the DT inversely scales with the ferromagnet thickness, and the FT has a threshold effect that appears only when the ferromagnetic layer is thinner than 1 nm. Through a thickness-dependence study with an additional copper insertion layer at the interface, we conclude that both SHE and Rashba effect exist in HM/FM heterostructures. The relative strengths of their contributions depend on the material system.

We have also demonstrated that MOKE with normal incidence light can be used to obtain the DT and FT in HM/FM bilayers by analyzing the polar Kerr effect as

well as the quadratic Kerr effect. The two effects can be distinguished by properly selecting the polarization of the incident light. We study a series of Pt/Py bilayers to verify the accuracy of this method. The angular dependence of SOTs in Ta (2 nm)/CoFeB (1 nm)/MgO (3 nm) trilayers with perpendicular magnetization is quantified based on polar MOKE with field calibration. A strong angular dependence is observed that is different from the previous experimental observations. Based on this strong angle dependence, we conclude there is a strong Rashba effect in this system. Simultaneous detection of current-driven DT and FT in HM/FM bilayers by measuring all three magnetization components m_x , m_y and m_z using a vector-resolved MOKE technique based on quadrant detection has also been accomplished. The technique can be easily extended to measure SOTs in systems with perpendicular magnetization, as well as in systems with arbitrary magnetization direction.

Chapter 1

INTRODUCTION

1.1 Introduction to Spintronics

The study of the magnetic properties of materials has been of interest for centuries. Generating, storing and processing information is one of the main reasons for this interest. The invention of transistors in 1947 by John Bardeen, Walter Brattain, and William Shockley started the evolution of modern electronic devices. They were awarded the Nobel Prize in Physics in 1956 for their discovery [1]. Moore's law, based on Gordon Moore's prediction in the 1970s, describes how the computing power of silicon-based devices evolves in time and correctly predicted that the number of transistors in an integrated chip would double approximately every two years [2,3]. The demand on the capacity of computing power per unit area has increased to the point where it is limited by the size of the circuit elements. Alternative platforms are needed to increase the efficiency of memory and logic devices.

Magnetic core memory was the earliest form of non-volatile magnetic storage and was composed of wires through ferrite rings [4]. An electric current was sent through wires to generate fields in the rings clockwise or anticlockwise to encode information as ones and zeros. But this technology was not scalable due to its mechanical structure. The advancements in the semiconductor industry together with the scalability problem drove core memory off the market in 1970s [4].

Today's conventional electronics use the electron's charge as the information carrier. To transmit information, the flow of charges through wires per unit time is

used and charges are stored in capacitors to save information [5]. For devices built on monitoring currents passing through electronic circuits, the trend is progressive device miniaturization, but decreasing wire diameter creates thermal challenges which then limit the amount of current sent, and as the size of capacitors decreases, charges leak across the capacitors. So, the challenge is to scale into the nanometer regime while keeping the functionality of the devices the same as before as well as doing this with much less energy. At these length scales, more efficient technologies are needed. As materials become smaller and smaller, they enter the quantum regime where their properties change. Another property of the electron, a quantum mechanical phenomenon called spin, then enters the picture. The spin degree of freedom of electrons can be used to store and transmit information. This field of research is called spintronics, and enables scaling into the nanometer regime [6]. With spintronics, it is possible to develop new devices and phenomena by utilizing the spin of the electron in addition to, or sometimes in place of, the charge of the electron. Spintronic devices utilize two states of spin to encode information as zeros and ones. The advantages of spintronic devices over conventional electronic devices are high performance and high-density magnetic storage, non-volatility -- meaning information is not lost even in the absence of power -- reduced energy consumption and increased speed of data processing.

The evolution of spintronics started with the discovery of the giant magnetoresistance effect [7,8]. This effect was used in creating spin valve sensors in read heads of hard disk drives (HDD). IBM introduced HDDs with a real density of 1 Gbit /in² and 16.8 GB of storage in 1997 [9]. With the implementation of magnetic tunnel junctions (MTJs), which exhibit tunneling magnetoresistance (TMR), into read

heads of HDDs for the first time in 2004, the storage density of the magnetic disk drives increased to 80-100 Gbits/in² [10]. With the advancement of spintronic technology, Seagate announced production of 1.25 Tbits/ in² hard disk drives in 2013 [11]. Magnetic tunnel junctions are also used in magnetic random access memory (MRAM) devices [12]. Second generation MRAMs use spin transfer torque (STT) effects to write information [13].

Although the technological imperative of scalability is an important motivation for spintronics research, interesting physics and the potential for new discoveries are adding to the growing interest in this area. Some examples of recent research findings include current-induced magnetization switching [14,15], control of domain formation and motion [16–19], and manipulating the dynamics of spin relaxation [20].

1.2 Giant Magnetoresistance and Spin Valves

Giant magnetoresistance (GMR) is a crucial discovery of Albert Fert and Peter Gruenberg in 1988, and is generally accepted as the birth of spintronics [7,8]. In 2007 they were awarded the Nobel Prize in physics for their discovery [21].

As current flows through a non-magnetic conductor, electrons will scatter independent of spin polarization, but as it flows through a magnetic material, electron scattering depends on spin orientation [22]. This scattering determines the resistance of the material. If a non-magnetic normal metal (NM) is sandwiched between two ferromagnetic materials (FM1 and FM2), the resistance of this structure will depend on the relative orientation of the ferromagnetic layers. If the magnetizations of two ferromagnetic layers are parallel, the resistance of this multilayer structure is lower than when the two layers are antiparallel. Let us first assume that the two ferromagnetic layers are magnetized parallel, as illustrated in Figure 1.1 (a). Current

sent through the FM1 layer is composed of spin up and spin down electrons. For electrons whose spin is parallel to the magnetization of FM1, the probability of scattering at FM1/NM and NM/FM2 is low, so the resistance is low for both interfaces (r). For electrons whose spin is antiparallel to the magnetization of the FM1, the electrons will scatter strongly at both interfaces and result in a higher resistance (R), so the total resistance is $R_p = rR/(r + R)$ for the parallel case. If the two ferromagnetic layers are antiparallel, scattering happens for both spin directions at different interfaces as seen in Figure 1.1 (b) and results in a total resistance of $R_{AP} = (r + R)/2$.

The relative magnetoresistance is defined as

$$\frac{\Delta R}{R} = \frac{R_{AP} - R_p}{R_p}. \quad (1.1)$$

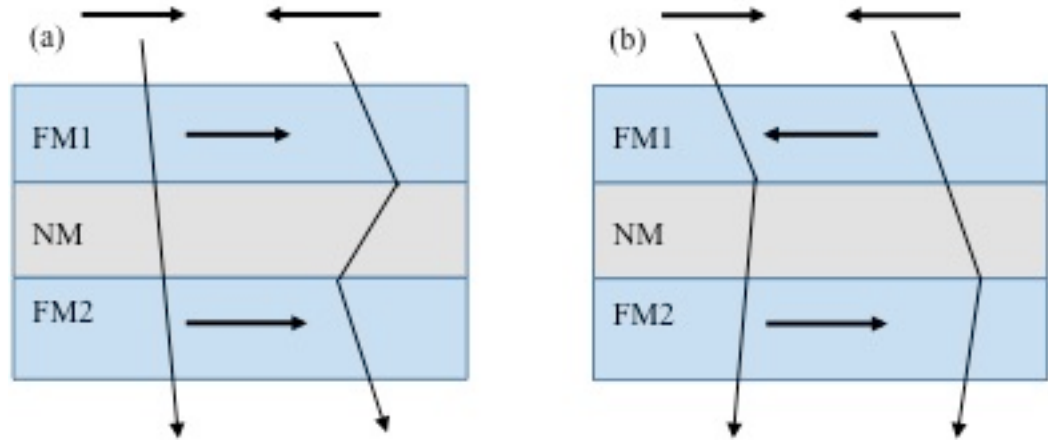


Figure 1.1: Giant magnetoresistance effect: A triple-layer film in which a non-magnetic normal metal is sandwiched between two ferromagnetic metals. (a) FM1 parallel to FM2 \rightarrow low resistance, (b) FM1 antiparallel to FM2 \rightarrow high resistance.

The main applications of this spin-dependent scattering effect are magnetic field sensors and magnetic memory elements.

Spin valve sensors are created based on the GMR effect [23]. In a spin valve, magnetization of one layer is fixed by placing an antiferromagnet next to it. At the interface of antiferromagnet and ferromagnet, an internal exchange coupling energy fixes the magnetic moment of that ferromagnetic layer. A non-magnetic conductor layer between the two ferromagnetic layers is thick enough to block any magnetic interaction between the ferromagnetic layers. The second magnetic layer, called the “free” layer, can change its magnetic moment in response to external magnetic fields. So, the resistance of this magnetic multilayer is very sensitive to the presence or absence of magnetic fields. IBM integrated GMR sensors in read heads of hard disk drives first the time in 1997, which increased the areal density of storage to 1 Gbit /in² [9]. This spintronic read head is extremely sensitive to small magnetic fields, so it is a very efficient way to read out information quickly and reliably.

1.3 Magnetic Tunnel Junctions

Tedrow and Meservey did a series of experiments studying the role of spin in determining the tunneling current, or spin-dependent tunneling, in the 1970s [24]. This led to the discovery of tunneling magnetoresistance (TMR) in magnetic tunnel junctions (MTJs). In MTJs, two magnetic layers are separated with a thin insulating material instead of a metal layer as in the case of GMR. TMR was measured in a structure composed of two ferromagnetic layers separated by an aluminum oxide layer, Al₂O₃, by Miyazaki and Tezuka in 1995, who found a TMR ratio of 30% at 4.2 K and 18% at 300 K [25]. The probability of electrons tunneling through the barrier depends on the relative orientation of the magnetic layers. Tunneling can be explained by Julliere’s model [26], which makes two assumptions. The first is that the tunneling electrons conserve their spin during the tunneling process, which means that

conductance occurs on two different channels for spin up and spin down electrons. In ferromagnets, the ground state energy bands split, creating majority and minority bands for the two spin directions near the Fermi level. If two magnetic layers are parallel to each other, the majority spins in FM1 tunnel into majority states of the FM2 and likewise minority spins of FM1 tunnel into minority states of FM2, as seen in Figure 1.2 (a), resulting in a low resistance. If the two magnetic layers are antiparallel, as shown in Figure 1.2 (b), the majority spins in FM1 tunnel to minority states in FM2 and vice versa, resulting in a high resistance.

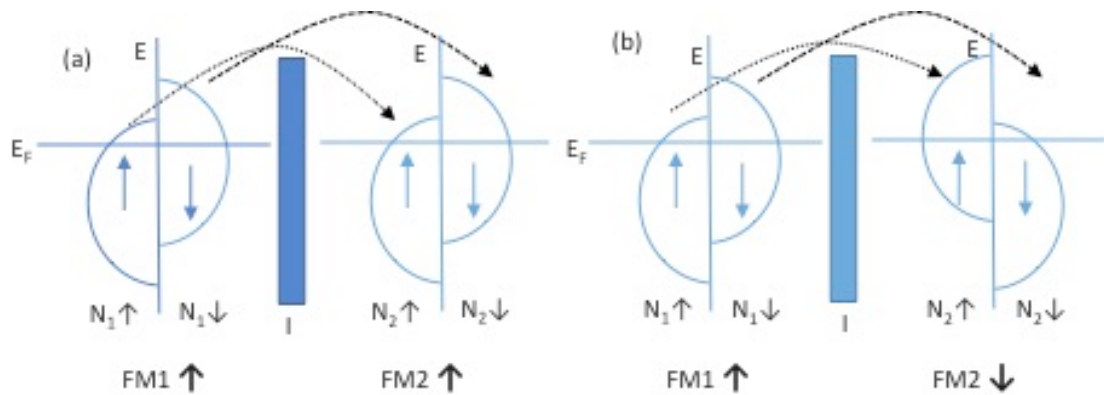


Figure 1.2: Illustration of TMR in a MTJ comprised of two ferromagnetic layers, FM1 and FM2, separated by an insulating barrier I. (a) For FM1 parallel to FM2, spin up electrons tunnel from majority to majority band and spin down electrons tunnel from minority to minority band → low resistance. (b) For FM1 antiparallel to FM2, spin up electrons tunnel from majority to minority band and spin down electrons tunnel from minority to majority band → high resistance.

The second assumption is that the tunneling current is proportional to the product of the density of states (DOS) at the Fermi level of the two ferromagnets. Based on these

assumptions, the conductivity of a junction for the parallel and antiparallel cases can be written respectively as

$$\begin{aligned} G_P &= N_1 \uparrow N_2 \uparrow + N_1 \downarrow N_2 \downarrow \\ G_{AP} &= N_1 \uparrow N_2 \downarrow + N_1 \downarrow N_2 \uparrow \end{aligned} \quad (1.2)$$

where $N_1 \uparrow$ and $N_1 \downarrow$ are the DOS for spin up and down electrons for FM1 and $N_2 \uparrow$ and $N_2 \downarrow$ are the DOS for spin up and down electrons for FM2 [12]. The tunneling magnetoresistance is then defined as

$$TMR = \frac{(G_P - G_{AP})}{G_{AP}}. \quad (1.3)$$

All of the early demonstrations of MTJs were based on Al_2O_3 as an insulating barrier [27], but theoretical calculations of this TMR were difficult due to the amorphous nature of Al_2O_3 . After experimental studies were done to understand which parameters were important to increase the TMR ratio, a TMR ratio of 70% was achieved with an Al_2O_3 barrier [28]. Theoretical calculations predicted a TMR ratio of 1000% at room temperature (RT) with a crystalline MgO tunnel barrier [29,30]. The first experimental demonstration of MTJs with an MgO barrier was performed in 2004 [31,32] and exhibited a TMR ratio of 180%, bigger than the Al_2O_3 -based MTJs. Increasing the TMR ratio is essential for many device applications such as magnetic-field sensors, as in the read head of HDD, and memory devices. In 2004, MTJs were implemented into read heads of HDD for the first time, achieving a storage density of 80-100 Gbits/in² [10]. With the advancement of nanofabrication technology, a TMR ratio of 500% was achieved at room temperature [33,34]. With new development techniques, MTJ dimensions rapidly scaled down to 100 nm together with higher TMR ratios, and another application of MTJs was developed, magnetic random access devices or MRAM [12]. In 2006, Freescale Semiconductor commercialized the first

MRAM [35]. MRAM is a fast, non-volatile and high-density memory device that uses a magnetic field generated from current through wires to manipulate the magnetization of a specific cell. At the nanoscale, it is difficult to efficiently control the magnetization, as the field generated on conducting lines decreases gradually over distance, resulting in the switching of unwanted cells, which then limits the scalability of the device. Another limitation of field-written MRAMs comes from the fact that as the size of the memory cell decreases, the anisotropy field required to avoid thermal excitations increases, due to $KV > 50 - 60k_B T$ where K is the anisotropy constant per unit volume, V is the volume of the cell, k_B is the Boltzmann constant, and T is the temperature. Due to these limitations, a lot of research has focused on spin transfer torque (STT) and its gradual implementation in memory devices as spin transfer torque magnetic random access memory (STT-MRAM) [36]. STT-MRAMs scale better than field-written MRAMs since the required current for switching decreases with the size of the MTJ cell. Also, since the current passes only through the MTJ cell, selectivity of a specific cell is achieved more reliably; but a disadvantage comes along with this. Since a high current passes through a thin spacer, it may overheat and damage the cell. This drawback may be overcome through the use of spin-orbit coupling-based spin transfer torque [14,15].

1.4 Micromagnetic Modeling and the Dynamic Equation

1.4.1 Micromagnetic Model

In the continuum hypothesis of the micromagnetic model of magnetism, atomic-length-scale interactions and macroscopic magnetic behaviors, which range from a few nanometers to a few micrometers, are simulated at the same time, ignoring

any discrete effects [37]. Short-scale interactions between magnetic moments, such as the exchange interaction, together with long-scale interactions, such as magnetostatic interactions, are combined and determine the spatial distribution of magnetization in a material. Considering a small volume δV containing a large amount of magnetic moments $\vec{\mu}_i$, which vary smoothly within this volume, the magnetization vector field, $\vec{M}(\vec{r}, t)$, which depends on spatial coordinate \vec{r} and time t with a constant magnitude M_s , can be defined as

$$\vec{M}(\vec{r}, t) = \frac{\sum_i \vec{\mu}_i}{\delta V} \quad (1.4)$$

with magnetization unit vector $\vec{m} = \vec{M}(\vec{r}, t)/M_s$. An effective field, H_{eff} , experienced by the magnetization inside that material should be defined such that all effects from different origins are taken into account. That effective field includes the exchange field, H_{exc} , anisotropy field, H_a , magnetostatic field, H_{ms} , together with the external applied field, H_{ext} , i.e.

$$H_{eff} = H_{exc} + H_a + H_{ms} + H_{ext} . \quad (1.5)$$

The relation between the effective field and the total energy density, ϵ_{tot} , is given by [38]

$$H_{eff} = \frac{1}{\mu_0 M_s} \frac{\delta \epsilon_{tot}}{\delta \vec{m}} . \quad (1.6)$$

The total energy then can be written as

$$E_{tot} = E_{exc} + E_a + E_{ms} + E_Z, \quad (1.7)$$

where E_Z is the Zeeman energy from the applied field. Each energy term will be expressed in terms of the continuous slowly varying magnetization unit vector, \vec{m} , of the medium.

1.4.1.1 Exchange Energy

The exchange interaction arises from a quantum mechanical phenomenon called the exchange force. Exchange forces originate from the overlap of the orbital wave functions. The wave function of indistinguishable particles either remains unchanged (symmetric) or changes its sign (anti-symmetric) when the two particles are exchanged. The presence of such symmetry indicates that there is a certain relation in the motion of identical particles that manifest itself as exchange energy. This relation results in a spin-spin interaction that couples neighboring spins and results in alignment of neighboring magnetic moments. The strength of the exchange interaction determines the Curie temperature; above which the spontaneous magnetization is lost and the material enters paramagnetic phase. The exchange interaction is short-range but the magnitude of the exchange energy density can be very strong. The product of the exchange energy density and volume of the unit cell gives the total exchange energy. Since it is a short-range interaction, the total energy arising from long-range interactions, such as magnetostatic energy, can exceed the exchange energy inside a material. Exchange coupling energy has the form

$$E_{ij}^{exc} = -2J_{ij}\vec{S}_i \cdot \vec{S}_j, \quad (1.8)$$

where J_{ij} is the exchange integral between the nearest neighbor atoms i and j and \vec{S}_i, \vec{S}_j are the spin angular momenta. The expression for the exchange energy is

derived following the formulation reported by Brown [39]:

$$E_{ij}^{exc} = -2J_{ij}\vec{S}_i \cdot \vec{S}_j = -2\sum_{i,j} J_{ij}\vec{S}_i \cdot \vec{S}_j, \quad (1.9)$$

where the sum is over nearest neighbors. Assuming the angle between neighboring spins, θ_{ij} , is small and the amplitude of the spins are constant within the crystal,

$$|\vec{S}_i| = S,$$

$$E_{exc} = -2JS^2 \sum \cos \theta_{ij} = -2JS^2 \sum \left(1 - \frac{\theta_{ij}^2}{2} \right) = -2JS^2 + JS^2 \sum \theta_{ij}^2. \quad (1.10)$$

Since \vec{m}_i is the unit vector of spins and \vec{r}_{ij} is the distance between neighboring spins, $|\theta_{ij}| = |\vec{m}_j - \vec{m}_i| = (\Delta\vec{r}_{ij} \cdot \nabla\vec{m})$. Substituting this value in Eq. (1.10),

$$\begin{aligned} E_{exc} &= Cst + JS^2 \sum \theta_{ij}^2 = Cst + JS^2 \sum (\Delta\vec{r}_{ij} \cdot \nabla\vec{m})^2 \\ E_{exc} &= Cst + JS^2 \sum_j \left[(\Delta\vec{r}_{ij} \cdot \nabla m_x)^2 + (\Delta\vec{r}_{ij} \cdot \nabla m_y)^2 + (\Delta\vec{r}_{ij} \cdot \nabla m_z)^2 \right]. \end{aligned} \quad (1.11)$$

Summing over all spins and neglecting the constant term, the exchange energy becomes

$$E_{exc} = \int_V A \left[(\nabla m_x)^2 + (\nabla m_y)^2 + (\nabla m_z)^2 \right] dV, \quad (1.12)$$

where A is a material-dependent exchange constant in energy per unit length, $A = \frac{JS^2}{a} C$, with a the lattice parameter of a cubic structure and C the number of atoms per unit cell. The isotropic nature of the exchange interaction, with no directional dependence, can be seen in Eq. (1.12).

1.4.1.2 Anisotropy Energy

Magnetic anisotropy in materials has various origins. In ferromagnets, and also in ferrimagnets and antiferromagnets, the magnetization tends to lie along a certain direction due to the crystalline structure, a phenomenon called magnetocrystalline anisotropy. The shape of the magnetic material also gives rise to anisotropy, called shape anisotropy or magnetostatic energy, which determines the demagnetizing energy. The surface anisotropy, or Néel surface energy is due to interface or surface effects that break the structural symmetry. Magnetoelastic anisotropy arising from the combination of magnetostriction and stress also contributes to the anisotropy energy.

1.4.1.2.1 Magnetocrystalline Anisotropy

In a crystal structure, electron orbits are aligned along certain crystal directions. Electron orbits are coupled to electron spins, and due to this spin-orbit coupling, electron spins prefer certain crystal directions, which manifests as magnetocrystalline anisotropy. Therefore, for magnetic materials, it is easier to magnetize in certain symmetry directions, referred as the easy axis, than in other directions. Typically, to derive the energy density, first the magnetocrystalline anisotropy energy is expressed in a power series expansion and then the symmetry of the crystal is taken into account.

In uniaxial anisotropy, there is only one easy axis. The magnetocrystalline energy density is expressed in terms of the angle between this easy axis and the magnetization, θ , as [40]

$$\varepsilon_{mc}^{uniaxial} = K_0 + K_1 \sin^2 \theta + K_2 \sin^4 \theta + \dots \quad (1.13)$$

where K_1 , K_2 and K_3 are the anisotropy coefficients having units of energy per volume. The anisotropy coefficients are temperature-dependent and at a given temperature their sign and magnitude determine the easy and hard directions, i.e., for positive (negative) K the energy is minimized by having $\theta = 0^\circ$ (90°). Surface anisotropy arises from the interface and usually creates a uniaxial easy axis along the surface normal, i.e., a positive anisotropy constant. An effective anisotropy constant is then defined as $K_{eff} = K_u + 2K_s/t$ where K_u , K_s are the bulk and surface contributions, respectively and t is the layer thickness.

In cubic anisotropy, there are three principle crystal axes. If the angle between the magnetization and principle axes are defined as a, b and c , then the magnetocrystalline energy density can be expressed in terms of directional cosines of these angles [40], $\alpha_1 = \cos a$, $\alpha_2 = \cos b$, $\alpha_3 = \cos c$,:

$$\epsilon_{mc}^{cubic} = K_0 + K_1(\alpha_1^2\alpha_2^2 + \alpha_2^2\alpha_3^2 + \alpha_3^2\alpha_1^2) + K_2\alpha_1^2\alpha_2^2\alpha_3^2 + \dots \quad (1.14)$$

1.4.1.2.2 Shape or Magnetostatic Anisotropy

Magnetostatic interactions are the result of interaction between individual magnetic moments over a long range. These interactions create a field that opposes the magnetization, called a demagnetizing field. Demagnetizing fields determine the domain structure of the magnetic material and depend on the macroscopic shape and size of the material. The demagnetizing field at a given point is given by the sum of the contributions of all magnetic moments within the magnetic volume, so it is not a local field. The demagnetizing field is given by

$$\vec{H}_d = -N_d \vec{M}, \quad (1.15)$$

where N_d is the demagnetizing factor. If a material is magnetized to saturation, the expression for the magnetostatic energy density or demagnetizing energy density stored in the material is given by [41]

$$\epsilon_{ms} = \mu_0 \int_0^{M_s} \vec{H}_d \cdot d\vec{M}. \quad (1.16)$$

1.4.1.2.3 Magnetoelastic Anisotropy

When an external field is applied to a ferromagnetic material, it creates stress on the ferromagnet, and in response the dimensions of the ferromagnet change. This interaction between magnetization and strain in the lattice is called magnetostriction. At strong fields, the dimensions change in three dimensions, but at low fields the change occurs in two dimensions. The inverse of this effect is the generation of a magnetic field due to application of external mechanical stress.

Linear saturation magnetostriction, λ_s , is strain due to the material being magnetized to saturation. It is expressed as [40] $\lambda_s = \Delta l/l$ and can be positive, negative or zero. A positive (negative) sign corresponds to expansion (contraction).

For an isotropic crystal with uniform stress, σ , the magnetoelastic energy density is given by

$$\varepsilon_{me} = \frac{3}{2} \lambda_s \sigma \sin^2 \theta, \quad (1.17)$$

where θ is the angle between the magnetization and the stress. The sign of the stress σ is positive (negative) for tensile (compressive) stress. The axis of the stress is an easy axis if $\lambda_s \sigma$ is positive. If this product is negative, the stress axis is a hard axis and the plane normal to the stress axis is an easy plane of magnetization.

1.4.1.3 Zeeman Energy

When a ferromagnetic material is subject to an external field, a torque, $\tau = -\mu_0 \vec{m} \times \vec{H}_{ext}$, is generated, giving rise to Zeeman energy. The energy density for Zeeman energy is given by

$$\varepsilon_Z = -\mu_0 \vec{M} \cdot \vec{H}_{ext}. \quad (1.18)$$

1.4.2 The Landau–Lifshitz–Gilbert Equation

Understanding magnetization dynamics plays an important role in achieving high speed, high density magnetic storage devices. In ferromagnetic materials, the dynamic evolution of the magnetic moment is described by the Landau and Lifshitz [42] or Landau-Lifshitz-Gilbert [43] equations. The Gilbert form is preferred for large damping; the two equations are equivalent for small damping [44].

The relation between the spin of an electron and its magnetic moment is given by

$$\vec{\mu} = -\gamma\vec{S}, \quad (1.19)$$

where $\gamma = g\mu_B/\hbar = ge/2m_e$ is the gyromagnetic ratio of the free electron where g is the Landé g factor, μ_B is Bohr magneton, e is charge of the electron and m_e is the mass of the electron. The electron spin angular momentum operator is given by $\vec{S} = \frac{\hbar}{2}\vec{\sigma}$, where $\vec{\sigma}$ is the Pauli operator. The Heisenberg equation of motion describes

the time evolution of a dynamical variable, in this case the magnetic moment, as

$$\frac{d\vec{\mu}}{dt} = \frac{1}{i\hbar}[\vec{\mu}, H] + \frac{\partial\vec{\mu}}{\partial t}, \quad (1.20)$$

where H is the Hamiltonian of the spin angular momentum operator and is given by

$$\begin{aligned} H &= -\gamma\vec{S} \cdot \vec{B}(t) \\ \vec{B}(t) &= \mu_0\vec{H}_{eff}(t), \end{aligned} \quad (1.21)$$

where μ_0 is the permeability of vacuum and $\vec{H}_{eff}(t)$ is the time-dependent effective magnetic field, which includes the field terms in Eq.1.5. The commutation of one component of the magnetic moment with this Hamiltonian is $[\mu_i, H] = [\gamma S_i, -\gamma S_i B_i]$ with $i = x, y, z$. Using commutation relations, Eq. (1.20) can be rewritten as

$$\frac{d\vec{\mu}}{dt} = -\gamma\vec{\mu} \times \vec{B} + \frac{\partial\vec{\mu}}{\partial t}. \quad (1.22)$$

Neglecting the second term on the right-hand side of the equation, since $\vec{\mu}$ does not explicitly depend on time, and using $\vec{B}(t) = \mu_0\vec{H}_{eff}(t)$, we get

$$\frac{d\vec{\mu}}{dt} = -\gamma_0(\vec{\mu} \times \vec{H}_{eff}), \quad (1.23)$$

with $\gamma_0 = \gamma\mu_0$. Replacing the single magnetic moment with the magnetization vector of a volume, based on Eq. (1.4), the equation becomes

$$\frac{d\vec{M}}{dt} = -\gamma_0(\vec{M} \times \vec{H}_{eff}), \quad (1.24)$$

describing the undamped precession of the magnetization under an effective field \vec{H}_{eff} . We can see from Eq. (1.24) that the magnitude of the magnetization vector is

constant and the magnetization precesses about the effective field at a constant angle, as illustrated in Figure 1.3(a). The precession frequency is called the Larmor frequency and is given by $f = \gamma_0 H_{eff} / 2\pi$.

To account for the fact that after a critical value of the external field, the magnetization aligns with the external magnetic field due to dissipation, Gilbert introduced a phenomenological term, preserving the magnetization magnitude, into the equation. The so-called Landau-Lifshitz-Gilbert (LLG) equation reads

$$\frac{d\vec{M}}{dt} = -\gamma_0 (\vec{M} \times \vec{H}_{eff}) + \frac{\alpha}{M_s} \left(\vec{M} \times \frac{d\vec{M}}{dt} \right), \quad (1.25)$$

where α is the Gilbert damping constant. The damping term points towards an effective field reducing the precession angle, as seen in Figure 1.3(b). To get the equivalent Landau-Lifshitz (LL) equation, $\vec{M} \times$ is applied to both sides of the LLG equation:

$$\vec{M} \times \frac{d\vec{M}}{dt} = -\gamma_0 \vec{M} \times (\vec{M} \times \vec{H}_{eff}) - \alpha M_s \frac{d\vec{M}}{dt}. \quad (1.26)$$

Substituting this equation into the second term of Eq. (1.25) gives

$$\frac{d\vec{M}}{dt} = -\frac{\gamma_0}{1+\alpha^2} (\vec{M} \times \vec{H}_{eff}) - \frac{\alpha}{1+\alpha^2} \frac{\gamma_0}{M_s} \vec{M} \times (\vec{M} \times \vec{H}_{eff}). \quad (1.27)$$

Defining $\gamma_L = \gamma_0 / (1+\alpha^2)$ and $\lambda = \gamma_0 \alpha / (1+\alpha^2)$ we get,

$$\frac{d\vec{M}}{dt} = -\gamma_L (\vec{M} \times \vec{H}_{eff}) - \frac{\lambda}{M_s} \vec{M} \times (\vec{M} \times \vec{H}_{eff}). \quad (1.28)$$

The first term describes precession with modified gyromagnetic ratio γ_L , and the second term accounts for the damping with modified damping coefficient λ .

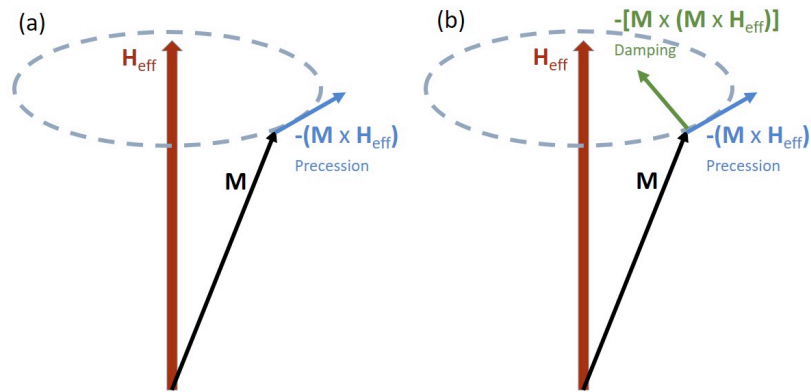


Figure 1.3: Illustration of magnetization precession (a) without damping (b) with damping.

1.5 Spin Transfer Torque

Spin transfer torque (STT) is the effect of spin-polarized current on the magnetization of a ferromagnetic body. It was discovered by Slonczewski [45] and Berger [46]. Switching the magnetization of nanomagnetic structures using the STT effect was first realized in metallic spin-valve structures [47] and then in magnetic tunnel junctions [48]. Spin transfer torque switching has attracted great attention due to its being an alternative to using a magnetic field, thus providing many exciting applications in magnetic storage technology. One application of the STT effect is spin transfer torque magnetic random access memory (STT-MRAM). STT-MRAM is a nonvolatile, high-density memory device with low power consumption and fast speed [13,49]. It has a better downsizing scalability than field-written MRAM because the current required for switching magnetization scales with the size of the structure. Also, addressing specific individual elements in a large array can be achieved more reliably due to current passing only through the multilayer structure. In 2016, Everspin announced the production of 256 Mb STT-MRAM chips [36]. Racetrack memory [50] is another potential memory application of spin transfer torque.

The mechanism of spin transfer torque can be explained for a multilayer structure as illustrated in Figure 1.4. The structure consists of two ferromagnetic layers separated by a nonmagnetic metallic spacer layer or an insulating layer as in the spin valve structure and MTJ, respectively. The first thin magnetic layer, called the pinned layer, has its magnetization fixed, \vec{M}_P , and the second thinner layer, called the free layer, has magnetization \vec{M}_F that is free to rotate. The pinned magnetic layer acts as a spin polarizer; the electric current passing through it gets spin polarized along its magnetization direction. If the magnetizations of the two magnetic layers are not collinear, as in Figure 1.4, a spin-polarized current passes through the spacer to the magnetic layer and the electrons tend to align their spins with \vec{M}_F due to the exchange interaction. During this process, the spin angular momentum component transverse to \vec{M}_F is lost. By conservation of angular momentum, this component exerts a torque on the magnetic moment of the free layer, called spin transfer torque.

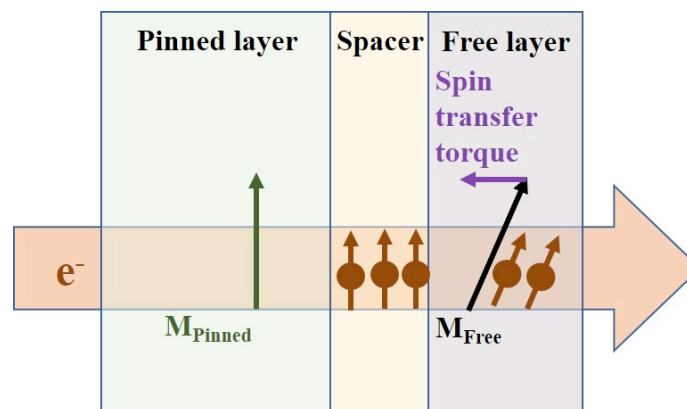


Figure 1.4: Illustration of spin transfer torque. Electron passing through a pinned magnetic layer get spin polarized. By conservation of angular momentum, the transverse spin angular momentum is transferred to the free magnetic layer.

The effect of spin transfer torque is described by adding a torque term, Slonczewski-like torque, to the LLG equation:

$$\gamma_0 \frac{\hbar}{2e \mu_0 M_s t} J \left[\vec{M}_F \times (\vec{M}_F \times \vec{M}_P) \right], \quad (1.29)$$

where $P(\theta)$ is the spin polarization function, which depends on the angle between the two magnetization directions, and t is the thickness of the free layer. Then the dynamic equation for the free layer is:

$$\frac{d\vec{M}_F}{dt} = -\gamma_0 (\vec{M}_F \times \vec{H}_{eff}) + \frac{\alpha}{M_s} \left(\vec{M}_F \times \frac{d\vec{M}_F}{dt} \right) + \gamma_0 \frac{\hbar}{2e \mu_0 M_s t} J \left[\vec{M}_F \times (\vec{M}_F \times \vec{M}_P) \right]. \quad (1.30)$$

The direction of the double cross-product term depends on the direction of current flow. If the electrons are flowing from the pinned layer to the free layer, the spin polarization passing through the spacer to the free layer is parallel to \vec{M}_P and the torque on the free layer rotates \vec{M}_F towards \vec{M}_P , realizing a parallel configuration of a spin valve or MTJ structure, as illustrated in Figure 1.5. If the electrons flow from free layer to pinned layer, the spin polarization passing through the spacer to the free layer is antiparallel to \vec{M}_P and the direction of the torque on the free layer reverses, rotating \vec{M}_F away from \vec{M}_P and thus realizing an antiparallel configuration.

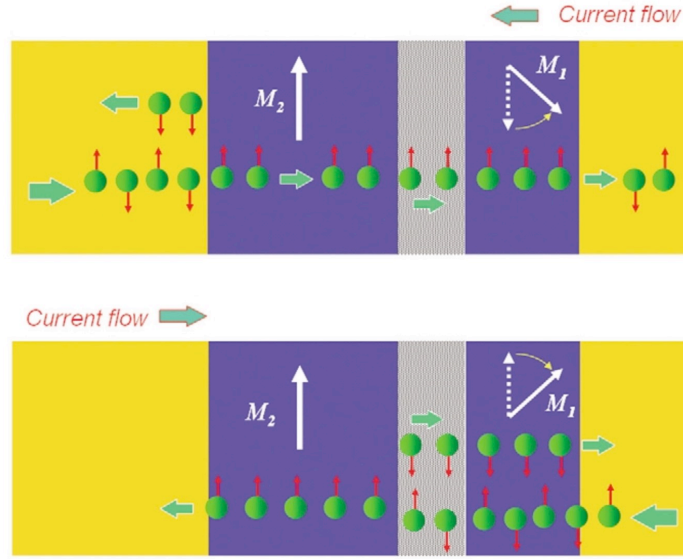


Figure 1.5: Illustration of the writing process in STT-MRAM. Reversing the current direction reverses the torque direction [51].

Depending on the current direction, the STT term can either be along the damping direction or antiparallel to it. If it is parallel, damping will get accelerated. If it is antiparallel, magnetization will either precess in an equilibrium state, which occurs when the energy lost through damping is equal to the energy gained from spin transfer torque, or switch when energy gain is greater than that lost through damping.

If the magnetizations of the fixed and free layers are not uniform, Eq. (1.30) is modified by an additional term, a field-like torque, accounting for the effect of electrons reflected at the spacer/free layer interface:

$$\frac{d\vec{M}_F}{dt} = -\gamma_0 (\vec{M}_F \times \vec{H}_{eff}) + \frac{\alpha}{M_s} \left(\vec{M}_F \times \frac{d\vec{M}_F}{dt} \right) + \tau_F (\vec{M}_F \times \vec{M}_P) + \tau_T (\vec{M}_F \times (\vec{M}_F \times \vec{M}_P)), \quad (1.31)$$

where τ_F and τ_T are the coefficients for field-like torque and Slonczewski-like torque, respectively. Slonczewski-like torque (also called in-plane or adiabatic torque),

is in the plane defined by the magnetizations of the pinned and free layers, and the field-like torque (also called perpendicular or non-adiabatic torque), is perpendicular to that plane.

If we rewrite Eq. (1.31) with the magnetization unit vector, $\vec{m} = \vec{M}(\vec{r}, t) / M_s$, and define the magnetization direction of the pinned layer, \vec{M}_p , as the direction of the injected spin $\vec{\sigma}$, the equation becomes

$$\frac{d\vec{m}}{dt} = -\gamma_0 (\vec{m} \times \vec{H}_{eff}) + \frac{\alpha}{M_s} \left(\vec{m} \times \frac{d\vec{m}}{dt} \right) + \tau_F (\vec{m} \times \vec{\sigma}) + \tau_T \vec{m} \times (\vec{m} \times \vec{\sigma}). \quad (1.32)$$

The magnitude of the two current-induced spin transfer torques depends on the material and device structure.

Recently, generating current-induced STT to manipulate magnetization in nonmagnetic/ferromagnetic metal (FM) bilayers [14,15,52,53] or topological insulator (TI)/FM bilayers [54] [55] has attracted great attention due to its high efficiency in magnetization switching, architectural simplicity and potential to couple with voltage-controlled magnetic anisotropy [56]. This new mechanism of switching magnetization is a potential candidate for writing in next-generation MRAMs. Writing bits using this bilayer scheme has advantages over STT writing of an MRAM cell. In STT writing, the high current passes through a thin spacer, which may overheat and damage the cell, but this drawback is not present in spin-orbit coupling torques since current passes through the HM or TI layer. This way of switching can be faster and can require less current than STT switching. Electric current applied to a nonmagnetic, typically HM or TI, layer exerts a field-like torque and a Slonczewski-like torque on the magnetization, which arise from spin-orbit coupling. Spin-orbit coupling-based torques (SOTs) arise from the bulk of the HM due to the spin Hall effect and from the HM/FM interface due to the Rashba effect. Besides magnetization switching, the SOT

effect also provides a convenient tool to manipulate magnetic domains [16–19,57], skyrmions [58] [59], and high-frequency oscillations [60–62].

1.6 Spin Hall Effect and Rashba Effect

In the ordinary Hall effect, electrons flowing through a normal metal are diverted by an external magnetic field \vec{B} applied perpendicular to the current direction due to the Lorentz force acting on the conduction electrons. The Lorentz force causes charges to accumulate on different sides of the metal, producing a voltage difference given by $V_{Hall} = R_H \vec{B} \times \vec{I}$, which is perpendicular to both \vec{I} and \vec{B} , as seen in Figure 1.6 (a). The anomalous Hall effect (AHE) describes the asymmetric separation of spin-up and spin-down electrons when current passes through a ferromagnet due to intrinsic and extrinsic (skew scattering and side-jump) contributions [63].

In the spin Hall effect (SHE), when current passes through a normal metal with spin-orbit coupling, electrons with spin up and spin down deflect to opposite sides of the metal due to the spin-orbit coupling. The electrons moving through the HM experience an effective magnetic field in their rest frame. Coupling between the spin of the electron and this effective magnetic field yields a spin accumulation occurring at the top and bottom of the normal metal, as seen in Figure 1.6 (b). The result is a pure spin current with no net charge generation. The spin current is transverse to the charge current and the spin polarization is perpendicular to the plane defined by the spin current and the charge current. The normal metal is usually chosen to be a heavy metal (HM) such as Pt or Ta, due to their strong spin-orbit coupling.

$$\vec{j}_s = \sigma_{SH} \vec{\sigma} \times \vec{j}_c \quad (1.33)$$

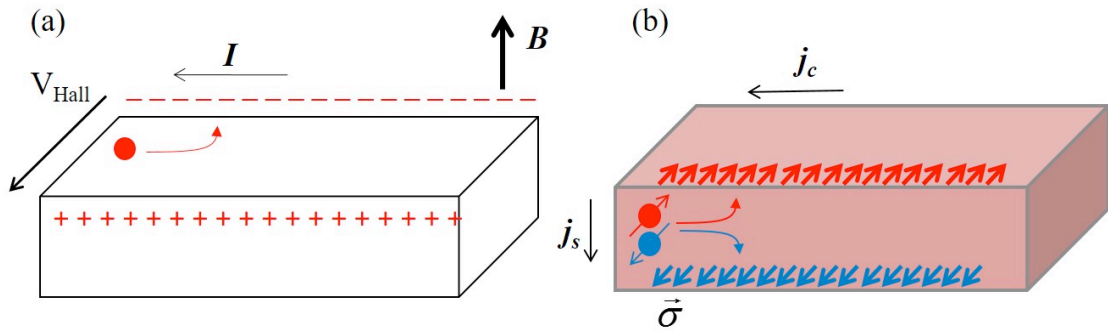


Figure 1.6: Schematics of (a) the ordinary Hall effect: in the presence of an external field, current passing through a normal metal creates a voltage; and (b) the spin Hall effect: due to spin-orbit interaction, current passing through a normal metal creates a spin current.

There are two mechanisms that contribute to the SHE arising from spin-orbit interactions: Intrinsic SHE and extrinsic SHE. Intrinsic SHE is due to the band structure of the crystal. An internal spin-orbit coupling force is experienced by electrons moving in a crystal. This force gives rise to transverse spin-dependent deflection of electrons even in the absence of impurity scattering [64]. In extrinsic SHE, transverse deflection (skew scattering and side jump) arises from scattering of the electrons off impurities due to spin orbit interaction [65].

The SHE was first discovered by Dyakonov and Perel in 1971 [66,67]. As there is no voltage generation present in SHE, the spin Hall angle was first measured by optical means [68,69] and then by the inverse spin Hall effect [70]. The inverse spin Hall effect is the production of a charge current due to the spin current, hence the name. Nowadays, HM/FM bilayer structures are used for magnetization switching and are a major focus of researchers due to their high potential as a writing mechanism in memory devices. In HM/FM bilayers both the SHE and Rashba effects arising from spin-orbit interactions contribute to the generation of spin orbit torques. In SHE, a spin

current is generated in the HM and the HM acts like a spin injector when placed adjacent to the FM, as seen in Figure 1.7(a). The injected spin current induces a field-like torque and Slonczewski-like torque on the FM due to the STT effect.

The Rashba effect enters the picture when inversion symmetry is broken, which is achieved by a HM/FM interface. An electric current through the interface between the HM and FM layers experiences a Rashba field via the spin-orbit interaction under structural inversion asymmetry and induces an in-plane nonequilibrium spin polarization perpendicular to the current at the interface, as seen in Figure 1.7 (b). Through exchange-coupling and spin relaxation, the current-induced polarization exerts an effective field as well as a torque on the FM.

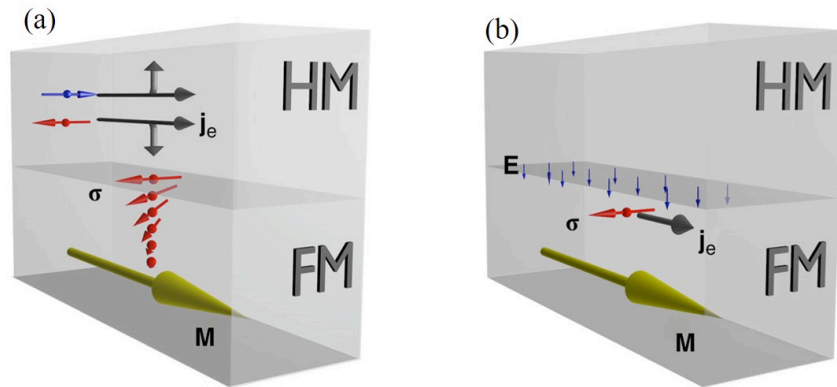


Figure 1.7: (a) Charge current through HM creates spin current through spin Hall effect. (b) Charge current through HM/FM interface creates spin polarization. Both mechanisms induce an effective field and a torque on the FM [52].

In this thesis, the main concentration is on the determination of the mechanisms of spin-orbit coupling based SOTs for writing magnetization in next-

generation MRAMs. We develop a sensitive current-driven spin-orbit torque magnetometer based on the magneto-optic Kerr effect to measure both field-like torque and damping-like torque. Magneto-optic Kerr effect results in changes to the light polarization reflected from a magnetized medium. We discuss the sample fabrication, characterization, experimental techniques and details of the MOKE technique in Chapter 2. In Chapter 3, with MOKE technique, we identify the contributions of the SHE and the Rashba effect to SOTs in HM/FM bilayers with in-plane magnetic anisotropy. The detection of current-driven SOTs using polar and quadratic MOKE is explained in Chapter 4. The angular dependence of SOTs in HM/FM/Metal-Oxide trilayers with perpendicular magnetic anisotropy is quantitatively measured via MOKE in Chapter 5. Simultaneous detection of SOTs using a vector-resolved MOKE technique based on quadrant detection in HM/FM bilayers is presented in Chapter 6.

REFERENCES

- [1] M. Riordan and L. Hoddeson, *Crystal Fire: The Birth of the Information Age* (1997).
- [2] G. Moore, *IEEE Spectr.* **16**, 30 (1979).
- [3] R. R. Schaller, *IEEE Spectr.* **34**, 52 (1997).
- [4] B. North and O. Nash, (2011).
- [5] C. Chappert, A. Fert, and F. N. Van Dau, *Nat. Mater.* **6**, 813 (2007).
- [6] S. Das Sarma, *Am. Sci.* **89**, 516 (2001).
- [7] G. Binasch, P. Grünberg, F. Saurenbach, and W. Zinn, *Phys. Rev. B* **39**, 4828 (1989).
- [8] M. N. Baibich, J. M. Broto, A. Fert, F. N. Van Dau, F. Petroff, P. Etienne, G. Creuzet, A. Friederich, and J. Chazelas, *Phys. Rev. Lett.* **61**, 2472 (1988).
- [9] R. Scranton, CHM Storage SIG Res. Notes (2012).
- [10] Sining Mao, Yonghua Chen, Feng Liu, Xingfu Chen, Bin Xu, Puling Lu, M. Patwari, Haiwen Xi, Clif Chang, B. Miller, D. Menard, B. Pant, J. Loven, K. Duxstad, Shaoping Li, Zhengyong Zhang, A. Johnston, R. Lamberton, M. Gubbins, T. McLaughlin, J. Gadbois, Juren Ding, B. Cross, Song Xue, and P. Ryan, *IEEE Trans. Magn.* **42**, 97 (2006).
- [11] *Bus. Wire* (2013).
- [12] M. Guth, G. Schmerber, and A. Dinia, *Mater. Sci. Eng. C* **19**, 129 (2002).
- [13] D. Apalkov, A. Ong, A. Driskill-Smith, M. Krounbi, A. Khvalkovskiy, S. Watts, V. Nikitin, X. Tang, D. Lottis, K. Moon, X. Luo, and E. Chen, *ACM J. Emerg. Technol. Comput. Syst.* **9**, 1 (2013).
- [14] I. M. Miron, K. Garello, G. Gaudin, P.-J. Zermatten, M. V. Costache, S. Auffret, S. Bandiera, B. Rodmacq, A. Schuhl, and P. Gambardella, *Nature* **476**,

- 189 (2011).
- [15] L. Liu, C.-F. Pai, Y. Li, H. W. Tseng, D. C. Ralph, and R. A. Buhrman, *Science* (80-.). **336**, 555 (2012).
 - [16] I. M. Miron, T. Moore, H. Szabolcs, L. D. Buda-Prejbeanu, S. Auffret, B. Rodmacq, S. Pizzini, J. Vogel, M. Bonfim, A. Schuhl, and G. Gaudin, *Nat. Mater.* **10**, 419 (2011).
 - [17] J. H. Franken, H. J. M. Swagten, and B. Koopmans, *Nat. Nanotechnol.* **7**, 499 (2012).
 - [18] P. P. J. Haazen, E. Murè, J. H. Franken, R. Lavrijsen, H. J. M. Swagten, and B. Koopmans, *Nat. Mater.* **12**, 299 (2013).
 - [19] S. Emori, U. Bauer, S.-M. Ahn, E. Martinez, and G. S. D. Beach, *Nat. Mater.* **12**, 611 (2013).
 - [20] K. Ando, S. Takahashi, K. Harii, K. Sasage, J. Ieda, S. Maekawa, and E. Saitoh, *Phys. Rev. Lett.* **101**, 36601 (2008).
 - [21] Nobel Media AB (2014).
 - [22] I. Ennen, D. Kappe, T. Rempel, C. Glenske, and A. Hütten, *Sensors (Basel)*. **16**, (2016).
 - [23] B. Dieny, V. S. Speriosu, S. S. P. Parkin, B. A. Gurney, D. R. Wilhoit, and D. Mauri, *Phys. Rev. B* **43**, 1297 (1991).
 - [24] P. M. Tedrow and R. Meservey, *Phys. Rev. Lett.* **26**, 192 (1971).
 - [25] T. Miyazaki and N. Tezuka, *J. Magn. Magn. Mater.* **139**, 231 (1995).
 - [26] M. Julliere, *Phys. Lett. A* **54**, 225 (1975).
 - [27] H. J. M. Swagten and P. V. Paluskar, in *Encycl. Mater. Sci. Technol.* (Elsevier, 2010), pp. 1–7.
 - [28] D. Wang, C. Nordman, J. Daughton, Z. Qian, and J. Fink, *IEEE Trans. Magn* **40**, 2269 (2004).
 - [29] W. H. Butler, X.-G. Zhang, T. C. Schulthess, and J. M. MacLaren, *Phys. Rev. B* **63**, 54416 (2001).
 - [30] J. Mathon and A. Umerski, *Phys. Rev. B* **63**, 220403 (2001).

- [31] S. Yuasa, A. Fukushima, T. Nagahama, K. Ando, and Y. Suzuki, Japan. J. Appl. Phys. **43**, L588 (2004).
- [32] S. Yuasa, T. Nagahama, A. Fukushima, Y. Suzuki, and K. Ando, Nat. Mater. **3**, 868 (2004).
- [33] Y. M. Lee, J. Hayakawa, S. Ikeda, F. Matsukura, and H. Ohno, Appl. Phys. Lett. **90**, 212507 (2007).
- [34] S. Yuasa and D. D. Djayaprawira, J. Phys. D. Appl. Phys. **40**, R337 (2007).
- [35] R. W. Dave, G. Steiner, J. M. Slaughter, J. J. Sun, B. Craigo, S. Pietambaram, K. Smith, G. Grynkewich, M. DeHerrera, J. Åkerman, and S. Tehrani, IEEE Trans. Magn. **42**, 8 (2006).
- [36] R. Mertens, Mram-Info.com (2016).
- [37] A. Aharoni, *Introduction to the Theory of Ferromagnetism* (Clarendon Press, 2000).
- [38] J. E. Miltat and M. J. Donahue, *Handbook of Magnetism and Advanced Magnetic Materials* (John Wiley & Sons, Ltd., 2007).
- [39] W. F. Brown, *Magnetostatic Principles in Ferromagnetism* (North-Holland Publishing Company, 1962).
- [40] K. M. Krishnan, *Fundamentals and Applications of Magnetic Materials* (Oxford University Press, 2016).
- [41] M. D'Aquino, Nonlinear Magnetization Dynamics in Thin Films and Nanoparticles, UNIVERSITÀ DEGLI STUDI DI NAPOLI "FEDERICO II", 2004.
- [42] L. D. Landau and E. M. Lifshitz, *Electrodynamics of Continuous Media* (Pergamon Press, 1960).
- [43] T. L. Gilbert, IEEE Trans. Magn. **40**, 3443 (2004).
- [44] J. C. Mallison, IEEE Trans. Magn **23**, 2003 (1987).
- [45] J. C. Slonczewski, J. Magn. Magn. Mater. **159**, L1 (1996).
- [46] L. Berger, Phys. Rev. B **54**, 9353 (1996).
- [47] J. A. Katine, F. J. Albert, R. A. Buhrman, E. B. Myers, and D. C. Ralph, Phys.

- Rev. Lett. **84**, 3149 (2000).
- [48] Y. Huai, F. Albert, P. Nguyen, M. Pakala, and T. Valet, *Appl. Phys. Lett.* **84**, 3118 (2004).
- [49] E. Chen, D. Apalkov, Z. Diao, A. Driskill-Smith, D. Druist, D. Lottis, V. Nikitin, X. Tang, S. Watts, S. Wang, S. A. Wolf, A. W. Ghosh, J. W. Lu, S. J. Poon, M. Stan, W. H. Butler, S. Gupta, C. K. A. Mewes, T. Mewes, and P. B. Visscher, *IEEE Trans. Magn.* **46**, 1873 (2010).
- [50] S. S. P. Parkin, M. Hayashi, and L. Thomas, *Science (80-.)*. **320**, 190 (2008).
- [51] J.-G. (Jimmy) Zhu and C. Park, *Mater. Today* **9**, 36 (2006).
- [52] X. Fan, J. Wu, Y. Chen, M. J. Jerry, H. Zhang, and J. Q. Xiao, *Nat. Commun.* **4**, 1799 (2013).
- [53] X. Fan, H. Celik, J. Wu, C. Ni, K. Lee, V. O. Lorenz, and J. Q. Xiao, *Nat. Commun.* **5**, 3042 (2014).
- [54] A. R. Mellnik, J. S. Lee, A. Richardella, J. L. Grab, P. J. Mintun, M. H. Fischer, A. Vaezi, A. Manchon, E.-A. Kim, N. Samarth, and D. C. Ralph, *Nature* **511**, 449 (2014).
- [55] Y. Fan, P. Upadhyaya, X. Kou, M. Lang, S. Takei, Z. Wang, J. Tang, L. He, L.-T. Chang, M. Montazeri, G. Yu, W. Jiang, T. Nie, R. N. Schwartz, Y. Tserkovnyak, and K. L. Wang, *Nat. Mater.* **13**, 699 (2014).
- [56] K.-S. Lee, S.-W. Lee, B.-C. Min, and K.-J. Lee, *Appl. Phys. Lett.* **102**, 112410 (2013).
- [57] K.-S. Ryu, L. Thomas, S.-H. Yang, and S. Parkin, *Nat. Nanotechnol.* **8**, 527 (2013).
- [58] W. Jiang, P. Upadhyaya, W. Zhang, G. Yu, M. B. Jungfleisch, F. Y. Fradin, J. E. Pearson, Y. Tserkovnyak, K. L. Wang, O. Heinonen, S. G. E. te Velthuis, and A. Hoffmann, *Science (80-.)*. **349**, 283 (2015).
- [59] G. Yu, P. Upadhyaya, X. Li, W. Li, S. K. Kim, Y. Fan, K. L. Wong, Y. Tserkovnyak, P. K. Amiri, and K. L. Wang, *Nano Lett.* **16**, 1981 (2016).
- [60] S. I. Kiselev, J. C. Sankey, I. N. Krivorotov, N. C. Emley, R. J. Schoelkopf, R. A. Buhrman, and D. C. Ralph, *Nature* **425**, 380 (2003).
- [61] L. Liu, C.-F. Pai, D. C. Ralph, and R. A. Buhrman, *Phys. Rev. Lett.* **109**,

- 186602 (2012).
- [62] L. Liu, T. Moriyama, D. C. Ralph, and R. A. Buhrman, *Phys. Rev. Lett.* **106**, 36601 (2011).
- [63] N. Nagaosa, J. Sinova, S. Onoda, A. H. MacDonald, and N. P. Ong, *Rev. Mod. Phys.* **82**, 1539 (2010).
- [64] J. Sinova, D. Culcer, Q. Niu, N. A. Sinitsyn, T. Jungwirth, and A. H. MacDonald, *Phys. Rev. Lett.* **92**, 126603 (2004).
- [65] J. Sinova, S. O. Valenzuela, J. Wunderlich, C. H. Back, and T. Jungwirth, *Rev. Mod. Phys.* **87**, 1213 (2015).
- [66] M. I. Dyakonov and V. I. Perel, *Pis'ma Zh. Eksp. Teor.* **13**, 657 (1971).
- [67] M. I. Dyakonov and V. I. Perel, *Phys. Lett. A* **35**, 459 (1971).
- [68] Y. K. Kato, R. C. Myers, A. C. Gossard, and D. D. Awschalom, *Science* (80-.). **306**, 1910 (2004).
- [69] J. Wunderlich, B. Kaestner, J. Sinova, and T. Jungwirth, *Phys. Rev. Lett.* **94**, 47204 (2005).
- [70] E. Saitoh, M. Ueda, H. Miyajima, and G. Tatara, *Appl. Phys. Lett.* **88**, 182509 (2006).
- [71] P. . Kelly and R. . Arnell, *Vacuum* **56**, 159 (2000).
- [72] M. Hughes, Semicore Equip. Inc. (2014).
- [73] J. E. Mahan, *Physical Vapor Deposition of Thin Films*, 1 edition (Wiley-Interscience, New York, 2000).
- [74] W. D. Sproul, D. J. Christie, and D. C. Carter, *Thin Solid Films* **491**, 1 (2005).
- [75] C. A. Mack, *SPIE* **Vol. 4440**, 59 (2001).
- [76] Oxford Instruments Plasma Technol. (2012).
- [77] A. Yamano, *Rigaku J.* **34**, (2018).
- [78] S. Foner, *J. Appl. Phys.* **79**, 4740 (1996).
- [79] Wikipedia Free Encycl. (n.d.).

- [80] L. Reimer, *Scanning Electron Microscopy : Physics of Image Formation and Microanalysis* (Springer, 1998).
- [81] W. H. Bragg, *Rev. Mod. Phys.* **3**, 449 (1931).
- [82] E. Hecht, *Optics*, 3rd Editio (Addison-Wesley Publishing Company, 1998).
- [83] P. Weinberger, *Philos. Mag. Lett.* **88**, 897 (2008).
- [84] W. J. Geerts, *A High Field Magneto-Optical Kerr Probe* (1999).
- [85] A. Khurshudov, in *Essent. Guid. to Comput. Data Storage*, 1st editio (Prentice Hall Ptr, 2001), pp. 201–216.
- [86] H. Ohldag, N. B. Weber, F. U. Hillebrecht, and E. Kisker, *J. Appl. Phys.* **91**, 2228 (2002).
- [87] P. Vavassori, *Appl. Phys. Lett.* **77**, 1605 (2000).
- [88] J. M. Florczak and E. D. Dahlberg, *J. Appl. Phys.* **67**, 7520 (1990).
- [89] C. Nistor, G. S. D. Beach, and J. L. Erskine, *Rev. Sci. Instrum.* **77**, 103901 (2006).
- [90] T. Gerrits, P. Krivosik, M. L. Schneider, C. E. Patton, and T. J. Silva, *Phys. Rev. Lett.* **98**, 207602 (2007).
- [91] X. Fan, A. R. Mellnik, W. Wang, N. Reynolds, T. Wang, H. Celik, V. O. Lorenz, D. C. Ralph, and J. Q. Xiao, *Appl. Phys. Lett.* **109**, 122406 (2016).
- [92] S. D. Bader, *J. Magn. Magn. Mater.* **100**, 440 (1991).
- [93] J. Hamrlová, J. Hamrle, K. Postava, and J. Pištora, *Phys. Status Solidi Basic Res.* **250**, 2194 (2013).
- [94] M. Buchmeier, R. Schreiber, D. E. Bürgler, and C. M. Schneider, *Phys. Rev. B* **79**, 64402 (2009).
- [95] P. N. Argyres, *Phys. Rev.* **97**, 334 (1955).
- [96] J. D. Jackson, *Classical Electrodynamics* (Wiley and Sons Inc, 1975).
- [97] G. R. Fowles, *Introduction to Modern Optics* (Holt, New York, 1975).
- [98] Z. Q. Qiu and S. D. Bader, *Rev. Sci. Instrum.* **71**, 1243 (2000).

- [99] W. Reim and J. Schoenes, in *Ferro-magnetic Mater. Vol. 5*, edited by K. H. J. Buschow and E. P. Wohlfarth (1990).
- [100] C. You and S. Shin, *Appl. Phys. Lett.* **69**, 1315 (1996).
- [101] R. P. Hunt, *J. Appl. Phys.* **38**, 1652 (1967).
- [102] P. S. Pershan, *J. Appl. Phys.* **38**, 1482 (1967).
- [103] J. Zak, E. R. Moog, C. Liu, and S. D. Bader, *J. Appl. Phys.* **68**, 4203 (1990).
- [104] T. Nakagawa, in *Compend. Surf. Interface Anal.* (Springer Singapore, Singapore, 2018), pp. 667–671.
- [105] J. L. Erskine and E. A. Stern, *Phys. Rev. B* **8**, 1239 (1973).
- [106] P. Bruno, Y. Suzuki, and C. Chappert, *Phys. Rev. B* **53**, 9214 (1996).
- [107] J. Park, *Optical and Magneto-Optic Kerr Effects of MnBi, Ni₂MnGa, and Gd₅Si₂Ge₂*, Iowa State University, 2004.
- [108] Myers, Ralph, Katine, Louie, and Buhrman, *Science* **285**, 867 (1999).
- [109] M. Weisheit, S. Fahler, A. Marty, Y. Souche, C. Poinignon, and D. Givord, *Science (80-.)*. **315**, 349 (2007).
- [110] Y.-H. Chu, L. W. Martin, M. B. Holcomb, M. Gajek, S.-J. Han, Q. He, N. Balke, C.-H. Yang, D. Lee, W. Hu, Q. Zhan, P.-L. Yang, A. Fraile-Rodríguez, A. Scholl, S. X. Wang, and R. Ramesh, *Nat. Mater.* **7**, 478 (2008).
- [111] T. Maruyama, Y. Shiota, T. Nozaki, K. Ohta, N. Toda, M. Mizuguchi, A. A. Tulapurkar, T. Shinjo, M. Shiraishi, S. Mizukami, Y. Ando, and Y. Suzuki, *Nat. Nanotechnol.* **4**, 158 (2009).
- [112] J. A. Katine and E. E. Fullerton, *J. Magn. Magn. Mater.* **320**, 1217 (2008).
- [113] J. Kim, J. Sinha, M. Hayashi, M. Yamanouchi, S. Fukami, T. Suzuki, S. Mitani, and H. Ohno, *Nat. Mater.* **12**, 240 (2013).
- [114] G. Yu, P. Upadhyaya, Y. Fan, J. G. Alzate, W. Jiang, K. L. Wong, S. Takei, S. A. Bender, L.-T. Chang, Y. Jiang, M. Lang, J. Tang, Y. Wang, Y. Tserkovnyak, P. K. Amiri, and K. L. Wang, *Nat. Nanotechnol.* **9**, 548 (2014).
- [115] X. Zhang, C. H. Wan, Z. H. Yuan, Q. T. Zhang, H. Wu, L. Huang, W. J. Kong, C. Fang, U. Khan, and X. F. Han, (2016).

- [116] K. Garello, I. M. Miron, C. O. Avci, F. Freimuth, Y. Mokrousov, S. Blügel, S. Auffret, O. Boulle, G. Gaudin, and P. Gambardella, *Nat. Nanotechnol.* **8**, 587 (2013).
- [117] C. Zhang, S. Fukami, H. Sato, F. Matsukura, and H. Ohno, *Appl. Phys. Lett.* **107**, 12401 (2015).
- [118] V. E. Demidov, S. Urazhdin, H. Ulrichs, V. Tiberkevich, A. Slavin, D. Baither, G. Schmitz, and S. O. Demokritov, *Nat. Mater.* **11**, 1028 (2012).
- [119] P. M. Haney, H.-W. Lee, K.-J. Lee, A. Manchon, and M. D. Stiles, (2013).
- [120] C. O. Avci, K. Garello, M. Gabureac, A. Ghosh, A. Fuhrer, S. F. Alvarado, and P. Gambardella, *Phys. Rev. B* **90**, 224427 (2014).
- [121] L. Liu, R. A. Buhrman, and D. C. Ralph, (2011).
- [122] T. Moriya, *Phys. Rev. Lett.* **4**, 228 (1960).
- [123] S. Zhang, P. M. Levy, and A. Fert, *Phys. Rev. Lett.* **88**, 236601 (2002).
- [124] J. Zhang, P. Levy, S. Zhang, and V. Antropov, *Phys. Rev. Lett.* **93**, 256602 (2004).
- [125] D. A. Pesin and A. H. MacDonald, *Phys. Rev. B* **86**, 14416 (2012).
- [126] X. Wang and A. Manchon, *Phys. Rev. Lett.* **108**, 117201 (2012).
- [127] K.-W. Kim, S.-M. Seo, J. Ryu, K.-J. Lee, and H.-W. Lee, *Phys. Rev. B* **85**, 180404 (2012).
- [128] Y. Tserkovnyak, A. Brataas, and G. E. W. Bauer, *Phys. Rev. B* **66**, 224403 (2002).
- [129] J. Bass and W. P. Pratt, *J. Phys. Condens. Matter* **19**, 183201 (2007).
- [130] N. Nakajima, T. Koide, T. Shidara, H. Miyauchi, H. Fukutani, A. Fujimori, K. Iio, T. Katayama, M. Nývlt, and Y. Suzuki, *Phys. Rev. Lett.* **81**, 5229 (1998).
- [131] S. Y. Huang, X. Fan, D. Qu, Y. P. Chen, W. G. Wang, J. Wu, T. Y. Chen, J. Q. Xiao, and C. L. Chien, *Phys. Rev. Lett.* **109**, 107204 (2012).
- [132] G.-M. Choi and D. G. Cahill, *Phys. Rev. B* **90**, 214432 (2014).
- [133] Z. Q. Qiu and S. D. Bader, *Rev. Sci. Instrum.* **71**, 1243 (2000).

- [134] M. Montazeri, P. Upadhyaya, M. C. Onbasli, G. Yu, K. L. Wong, M. Lang, Y. Fan, X. Li, P. Khalili Amiri, R. N. Schwartz, C. A. Ross, and K. L. Wang, *Nat. Commun.* **6**, 8958 (2015).
- [135] C. Dehesa-Martínez, L. Blanco-Gutierrez, M. Vélez, J. Díaz, L. M. Alvarez-Prado, and J. M. Alameda, *Phys. Rev. B* **64**, 24417 (2001).
- [136] R. . Osgood III, S. . Bader, B. . Clemens, R. . White, and H. Matsuyama, *J. Magn. Mater.* **182**, 297 (1998).
- [137] U. H. Pi, K. Won Kim, J. Y. Bae, S. C. Lee, Y. J. Cho, K. S. Kim, and S. Seo, *Appl. Phys. Lett.* **97**, 162507 (2010).
- [138] T. Suzuki, S. Fukami, N. Ishiwata, M. Yamanouchi, S. Ikeda, N. Kasai, and H. Ohno, *Appl. Phys. Lett.* **98**, 142505 (2011).
- [139] F. Freimuth, S. Blügel, and Y. Mokrousov, *Phys. Rev. B* **90**, 174423 (2014).
- [140] I. Mihai Miron, G. Gaudin, S. Auffret, B. Rodmacq, A. Schuhl, S. Pizzini, J. Vogel, and P. Gambardella, *Nat. Mater.* **9**, 230 (2010).
- [141] P. M. Haney, H.-W. Lee, K.-J. Lee, A. Manchon, and M. D. Stiles, *Phys. Rev. B* **87**, 174411 (2013).
- [142] V. P. Amin and M. D. Stiles, *Phys. Rev. B* **94**, 104420 (2016).
- [143] A. Manchon, (2012).
- [144] X. Fan, H. Celik, J. Wu, C. Ni, K. J. Lee, V. O. Lorenz, and J. Q. Xiao, *Nat. Commun.* **5**, 1 (2014).
- [145] S. Ikeda, K. Miura, H. Yamamoto, K. Mizunuma, H. D. Gan, M. Endo, S. Kanai, J. Hayakawa, F. Matsukura, and H. Ohno, *Nat. Mater.* **9**, 721 (2010).
- [146] W.-G. Wang, M. Li, S. Hageman, and C. L. Chien, *Nat. Mater.* **11**, 64 (2012).
- [147] S. Kanai, M. Yamanouchi, S. Ikeda, Y. Nakatani, F. Matsukura, and H. Ohno, *Appl. Phys. Lett.* **101**, 122403 (2012).
- [148] W.-G. Wang, S. Hageman, M. Li, S. Huang, X. Kou, X. Fan, J. Q. Xiao, and C. L. Chien, *Appl. Phys. Lett.* **99**, 102502 (2011).
- [149] H. X. Yang, M. Chshiev, B. Dieny, J. H. Lee, A. Manchon, and K. H. Shin, *Phys. Rev. B* **84**, 54401 (2011).

- [150] C. Zhang, M. Yamanouchi, H. Sato, S. Fukami, S. Ikeda, F. Matsukura, and H. Ohno, *Appl. Phys. Lett.* **103**, 262407 (2013).
- [151] X. Qiu, P. Deorani, K. Narayanapillai, K.-S. Lee, K.-J. Lee, H.-W. Lee, and H. Yang, *Sci. Rep.* **4**, 4491 (2015).
- [152] K. Garello, I. M. Miron, C. O. Avci, F. Freimuth, Y. Mokrousov, S. Blügel, S. Auffret, O. Boulle, G. Gaudin, and P. Gambardella, *Nat. Nanotechnol.* **8**, 587 (2013).
- [153] C. O. Avci, K. Garello, C. Nistor, S. Godey, B. Ballesteros, A. Mugarza, A. Barla, M. Valvidares, E. Pellegrin, A. Ghosh, I. M. Miron, O. Boulle, S. Auffret, G. Gaudin, and P. Gambardella, *Phys. Rev. B* **89**, 214419 (2014).
- [154] K.-S. Lee, D. Go, A. Manchon, P. M. Haney, M. D. Stiles, H.-W. Lee, and K.-J. Lee, *Phys. Rev. B* **91**, 144401 (2015).
- [155] S. Peng, M. Wang, H. Yang, L. Zeng, J. Nan, J. Zhou, Y. Zhang, A. Hallal, M. Chshiev, K. L. Wang, Q. Zhang, and W. Zhao, *Sci. Rep.* **5**, 18173 (2016).
- [156] M. Hayashi, J. Kim, M. Yamanouchi, and H. Ohno, *Phys. Rev. B* **89**, 144425 (2014).
- [157] S. Emori, T. Nan, A. M. Belkessam, X. Wang, A. D. Matyushov, C. J. Babroski, Y. Gao, H. Lin, and N. X. Sun, *Phys. Rev. B* **93**, 180402 (2016).
- [158] X. Fan, A. R. Mellnik, W. Wang, N. Reynolds, T. Wang, H. Celik, V. O. Lorenz, D. C. Ralph, and J. Q. Xiao, *Appl. Phys. Lett.* **109**, (2016).
- [159] C. Stamm, C. Murer, M. Berritta, J. Feng, M. Gabureac, P. M. Oppeneer, and P. Gambardella, *Phys. Rev. Lett.* **119**, 87203 (2017).
- [160] A. Berger and M. R. Pufall, *J. Appl. Phys.* **85**, 4583 (1999).
- [161] T. Kuschel, H. Bardenhagen, H. Wilkens, R. Schubert, J. Hamrle, J. Pištora, and J. Wollschläger, *J. Phys. D: Appl. Phys.* **44**, 265003 (2011).
- [162] H. F. Ding, S. Pütter, H. P. Oepen, and J. Kirschner, *Phys. Rev. B* **63**, 134425 (2001).
- [163] Z. J. Yang and M. R. Scheinfein, *J. Appl. Phys.* **74**, 6810 (1993).
- [164] P. S. Keatley, V. V. Kruglyak, A. Neudert, E. A. Galaktionov, R. J. Hicken, J. R. Childress, and J. A. Katine, *Phys. Rev. B* **78**, 214412 (2008).

- [165] K. Postava, A. Maziewski, A. Stupakiewicz, A. Wawro, L. T. Baczewski, Š. Višňovský, and T. Yamaguchi, *J. Eur. Opt. Soc. Rapid Publ.* **1**, 6017 (2006).
- [166] H. . Ding, S. Pütter, H. . Oepen, and J. Kirschner, *J. Magn. Magn. Mater.* **212**, 5 (2000).
- [167] J. Hamrle, S. Blomeier, O. Gaier, B. Hillebrands, H. Schneider, G. Jakob, K. Postava, and C. Felser, *J. Phys. D. Appl. Phys.* **40**, 1563 (2007).
- [168] K. Chen and S. Zhang, *Phys. Rev. B* **96**, 134401 (2017).

Chapter 2

FABRICATION, CHARACTERIZATION AND EXPERIMENTAL TECHNIQUES

2.1 Fabrication Techniques

2.1.1 Magnetron Sputtering Thin Film Deposition

Magnetron sputtering is a physical vapor deposition technique used to fabricate thin films with a variety of materials such as metals, alloys, insulators, and semiconductors [71]. It is a commonly preferred technique due to its versatility, reliability and the resultant high film quality.

The magnetron sputtering process involves ejecting atoms from a source material, called a target, onto a substrate such as a silicon wafer. The process begins with placing a substrate into a vacuum chamber that is filled with an inert gas such as argon. Then an electric field is applied between the target material and the substrate, which ionizes the inert gas atoms ($\text{Ar} \rightarrow \text{Ar}^+ + e$). A magnet behind the target provides a magnetic field to trap the free electrons over the target surface, which enhances the efficiency of ionization and thus increases the deposition rate. Collisions between these electrons and the inert gas atoms further increase the ionization efficiency and generate a plasma. The electric field accelerates the ions toward the target, which is negatively biased, and they bombard the atoms of the target. Atomic-size particles are ejected from the target material due to the collisions. By conservation of momentum, these particles move through the vacuum chamber and are deposited onto the substrate

as a thin film. Most commonly used magnetron sputtering targets are in circular or rectangular form. A schematic of a magnetron sputtering system is given in Figure 2.1 [72].

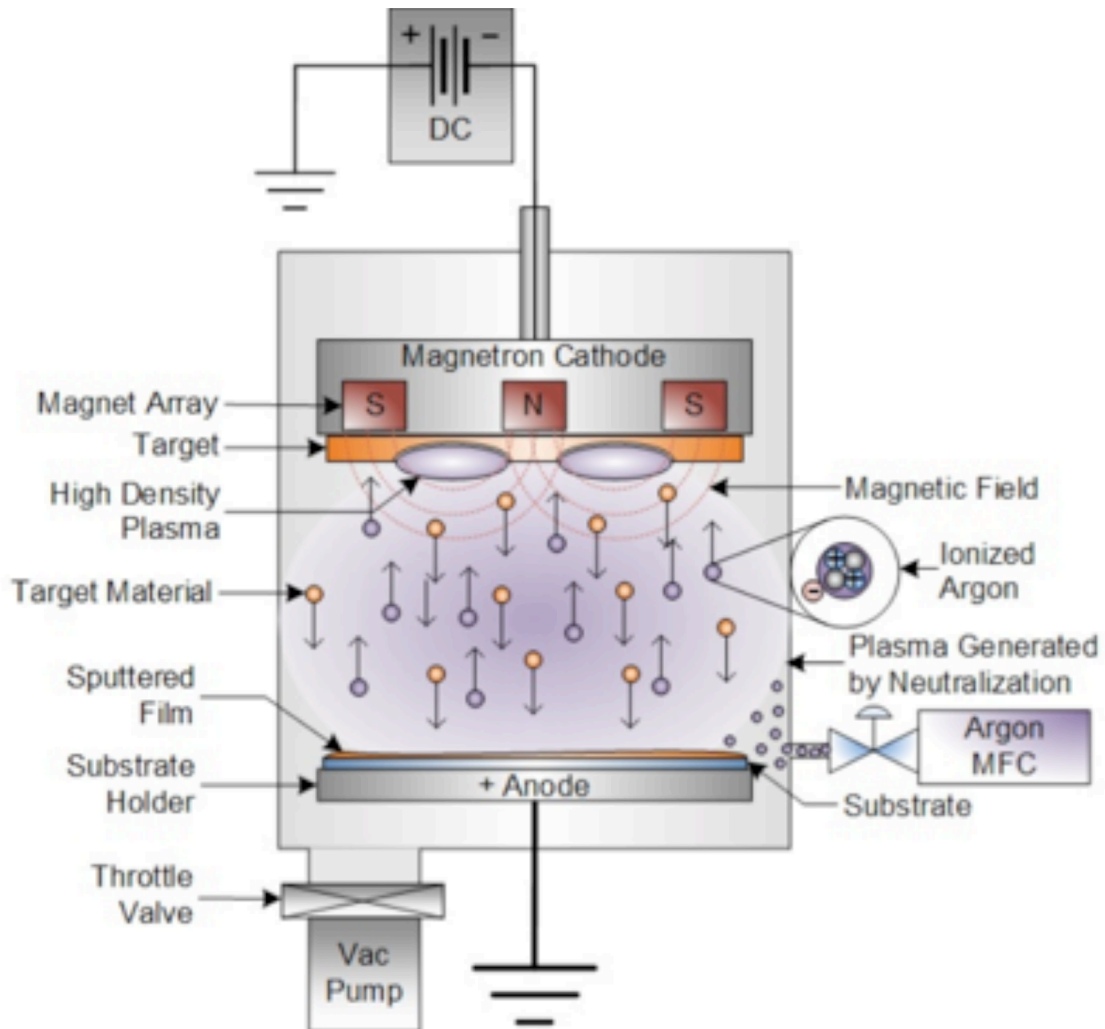


Figure 2.1: Schematic of thin-film magnetron sputtering. Argon is ionized and accelerated to a target. After collision, target atoms are ejected and travel to the substrate where they form a thin film [72].

Different types of power sources are used to sputter the atoms from the target material, such as direct current (DC) and radio frequency (RF) sputtering [73], and pulsed DC and high power impulse magnetron sputtering (HIPIMS). A DC power supply is used to deposit conductive materials like metals. For insulators like oxides, an RF power supply is used to avoid positive charge accumulation on the surface of the target due to collisions between the ions and the target. An alternating electric field with high frequency is applied to the target to neutralize the target surface. Reactive sputtering [74] is an alternative way of fabricating insulating thin films in which metallic targets are DC sputtered in the presence of reactive gasses such as nitrogen or oxygen. These gasses react with the target material to form a molecular compound. For example, a silicon target reactively sputtered with nitrogen produces silicon nitride film.

Thin films used in this thesis are deposited in a custom-made magnetron sputtering system in Prof. Xiao's Lab, which has seven magnetron sputtering cathodes and ten sample holders. A CTI cryo-pump is used to obtain high vacuum. A wedge technique, in which the sample holder is placed off-axis of the plasma to create a thickness gradient, is employed to get thin films with different thicknesses.

2.1.2 Photolithography

Photolithography, the formation of devices from a continuous film, is a process used in microfabrication [75]. It is one of the processes performed on a semiconductor substrate to create integrated circuits used in many electronic devices today such as phones, computers, and sensors. In photolithography, patterns are transferred from a photomask to a substrate with a light-sensitive polymer called a photoresist (PR). The photoresist is exposed to UV light and developed to form three-dimensional images on

the substrate. There are two types of PR, positive and negative, that react differently when exposed to the UV light. Positive PR becomes more soluble and negative PR becomes extremely difficult to dissolve in the photoresist developer when exposed to the UV light. For positive PR, the pattern on the mask will be transferred onto the sample, but for negative PR, the transparent area on the mask will be transferred. The procedures for positive and negative photolithography are illustrated in Figure 2.2.

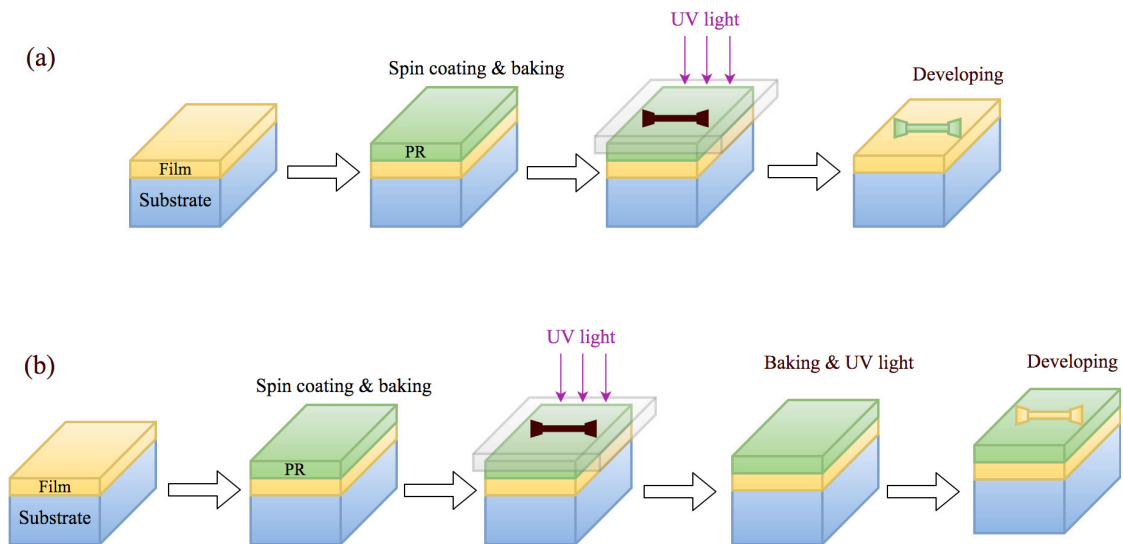


Figure 2.2: (a) Positive photolithography including the steps of spin coating, baking, UV light exposure with photomask and developing. (b) Negative photolithography including the steps of spin coating, baking, UV light exposure with photomask, baking, UV light exposure without photomask and developing.

The processing steps for positive photolithography performed as part of this thesis research are as follows:

1. Spin coating: Photoresist AZ1512 is dispensed onto the sample placed on a spinner and it is spun at 4000 rpm for 60 s to produce a uniform layer of PR covering the surface of the sample. The thickness of the PR

layer depends on the spin speeds and times, volume of the dispensed PR and the properties of the PR.

2. The PR-covered sample is baked at 110°C for 60s.
3. The PR-covered sample is aligned with the mask on a mask aligner (OAI Hybralign series 200) and exposed to UV light for 6 s. The patterns on the mask block the UV light, so only the parts of the PR exposed to UV light will change their properties.
4. The sample is immersed in the developer solvent MF-319 for about 20 s. The parts of the PR exposed to UV light became soluble in the developer and are removed, leaving an identical pattern of PR as the mask on the sample .

Negative photolithography processing steps:

1. Spin-coat with PR AZ5214 at 4000 rpm for 60 s.
2. Baking at 90°C for 60 s (called soft baking).
3. The PR-covered sample is aligned with the mask and exposed to UV light for 0.7 s.
4. The PR-coated sample is baked at 110°C for 60 s (called hard baking).
5. UV light exposure without photomask for 45 s.
6. The sample is immersed into developer solvent AZ-300 for about 25 s. The parts of the PR exposed to UV light are not dissolved in the developer, so only the parts of the PR protected with the mask are washed away.

2.1.3 Ion Beam Etching

Ion beam etching is a subtractive pattern transfer mechanism [76]. After patterns have been printed on PR-coated sample by photolithography, these patterns are transferred to the sample by removing the part of the film on the surface of the sample that was not covered by the PR. The PR resists the etching and the parts of the sample covered with it will be protected. Ion-beam etching can be classified into two categories, wet and dry etching. The dry etching process, called ion beam milling, is used to fabricate the samples used in this thesis. In ion beam milling, argon gas is pumped into the system. The bombardment of electrons emitted from a hot cathode filament with the argon gas generates Ar^+ . An accelerating grid is used to accelerate the Ar^+ towards the sample. The sample is bombarded by Ar^+ to remove atoms from the surface of the sample that is not covered by the PR. Once the etching is complete, the PR is washed away using acetone, resulting in the desired pattern etched into the deposited layer.

2.2 Characterization and Experimental Techniques

2.2.1 X-ray Diffraction

X-ray diffraction is a non-destructive analytical technique used to identify and characterize compound materials and thin films [77]. When X-rays interact with a target material, they scatter from the atoms in the target material. As the scattered X-rays interfere, diffraction patterns reveal information about the crystalline structure of the material. Bragg's Law describes the condition for constructive interference of the diffracted X-rays:

$$n\lambda = 2d \sin\theta, \quad (2.1)$$

where n is an integer number, λ is the X-ray wavelength, d is spacing between atomic layers in a crystal and θ is the angle of incidence. The thickness of thin films can be determined by Bragg's Law for small incidence angles, where d becomes the film thickness, and is used to calibrate the sputtering rate.

2.2.2 Vibrating Sample Magnetometer

The vibrating sample magnetometer (VSM) is widely used to characterize the magnetic properties of magnetic materials such as coercivity, remanence and saturation magnetization [78]. The detection mechanism of a VSM is depicted in Figure 2.3.

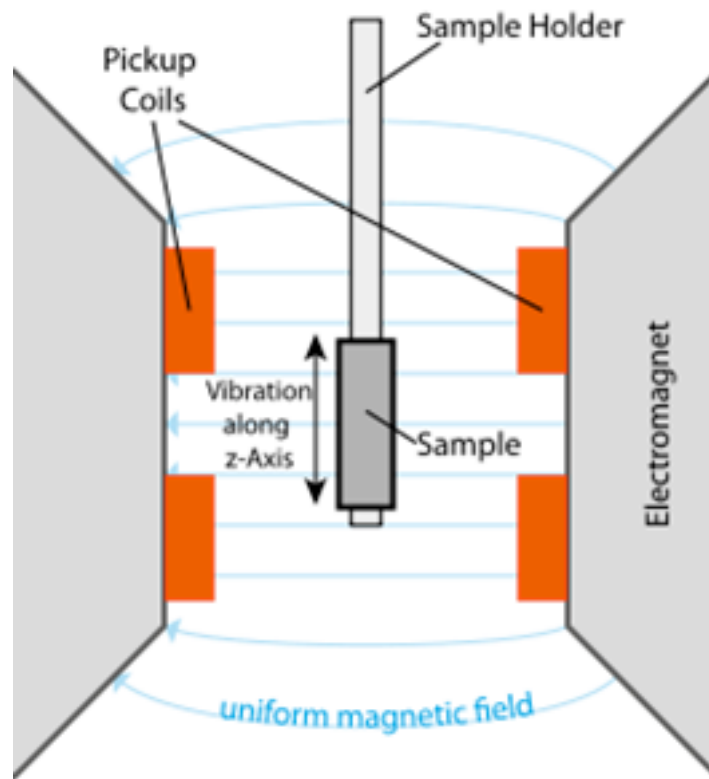


Figure 2.3: The detection mechanism of a vibrating sample magnetometer: a sample vibrates vertically with a constant frequency and an electromagnet provides a horizontal magnetic field [79].

The magnetic sample to be studied is attached to a sample holder that vibrates vertically with a constant frequency. A uniform magnetic field is applied, generated by an electromagnet. Pick-up coils detect the magnetic flux generated via the vibration of the sample. Due to Faraday's law, the change in the magnetic flux induces an AC voltage. A lock-in amplifier, using the signal driving the sample as a reference, measures the induced voltage, which is proportional to the magnetic moment of the sample. A hysteresis of the sample can also be measured by sweeping the external magnetic field.

2.2.3 Scanning Electron Microscope

A scanning electron microscope (SEM) is a type of electron microscope that scans the surface of a sample with a focused beam of high-energy electrons to create images of the sample surface [80]. Scanning the electron beam in a raster scan pattern generates high-resolution 2-dimensional images of a selected area. The electron-sample interaction produces a variety of signals containing information about the sample's surface topography, chemical composition and crystalline structure. The energy exchange between the high-energy electrons and the sample produces secondary electrons, backscattered electrons, diffracted backscattered electrons, electromagnetic radiation and heat. A specific emission can be detected with an SEM equipped with a specific detector. Secondary electrons detected by a secondary electron detector are commonly used for to gain information about the morphology and the topography of the sample.

2.2.4 Electrical Transport Measurements

Electrical transport measurements are performed by a four-point-probe set-up consisting of a current source (Keithley 220), a multimeter (Keithley 2001), a nanovoltmeter, a pair of Helmholtz coils and a power supply (BOP Kepco 20-20M). Control of the instruments and data collection is achieved remotely by National Instruments LabVIEW software. A Hall bar is used to perform current-in-plane transport measurements. Figure 2.4 shows a schematic representation of the four-probe station and a typical Hall bar structure. The current, I , is applied between contacts 5 and 6. A longitudinal voltage drop, V_L , is measured either between contacts 1 and 2 (or 3 and 4). Hall voltage, V_H is measured either between contacts 1 and 3 (or 2 and 4).

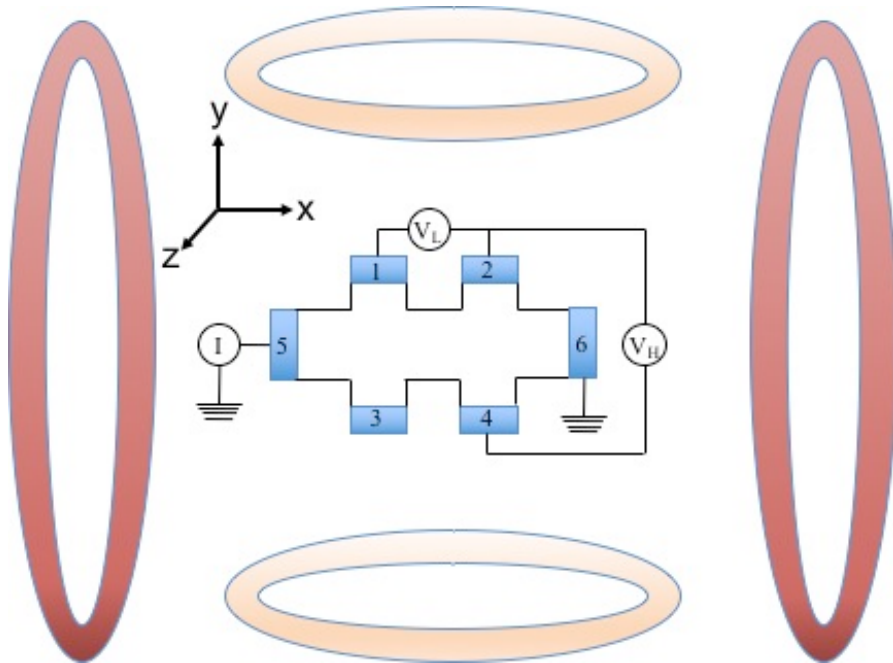


Figure 2.4: A four-probe station with Hall bar structure. Two pairs of Helmholtz coils, big and small, produce magnetic fields in x and y directions, respectively.

2.2.5 Magneto-Optic Kerr Effect

2.2.5.1 Background

Precise material characterization is essential for progress in modern information technology. Development of new concepts for practical applications such as data storage with spintronics relies on the characterization of magnetic materials and magnetic structures. Magneto-optic effects, interactions between magnetic fields and light, are used to study the properties of magnetic materials. Zeeman, Faraday, Voigt, Cotton-Mouton and Kerr effects are examples of magneto-optical effects. The microscopic origins of these effects are the spin-orbit interaction and exchange interaction, which depend on the optical transitions. In this work, we employ the magneto-optic Kerr effect to the measurement of current-induced spin-orbit torques.

Michael Faraday discovered the magneto-optic effect by discovering the connection between light and magnetism in the middle of the 19th century. His first attempt was to find a relation between light and an external electric field but was unsuccessful. He then tried a magnetic field instead of an electric field and saw the effect of rotation of the polarization plane of the transmitted light when a beam of linearly polarized light passes through a glass that is subject to a magnetic field [81]. This rotation is due to the difference of the index of refraction for right circular polarization and left circular polarization. The absorption coefficient difference between the two circular polarizations causes transmitted light to become elliptically polarized [82]. This phenomenon is called the Faraday effect.

The effect of the magnetic field on reflected light, rather than transmitted, was discovered by John Kerr in 1877. First he repeated Faraday's light-electric field interaction experiment and demonstrated the electro-optic effect in 1875. Then, by

using a horseshoe electromagnet and a paraffin flame as a light source, he found that the polarization plane of linearly polarized light rotates and the polarization state changes as it reflects from a magnetized medium [83]. As a result of this so-called magneto-optic Kerr effect (MOKE), the axis of polarization of linearly polarized light rotates (Kerr rotation angle θ_K) and a slight ellipticity is introduced (Kerr ellipticity ϵ_K). These two quantities form the complex Kerr angle $\phi_K = \theta_K + i\epsilon_K$. The Kerr rotation θ_K is the rotation angle of the major polarization axis, and Kerr ellipticity ϵ_K is defined as the ratio of major to minor axes. The Kerr rotation and ellipticity give a measure of the magnetization of the sample and are strong in highly reflecting ferromagnetic surfaces such as iron, nickel, and cobalt. In addition to the material type, the size of the effect depends upon the saturation magnetization of the surface domains, the wavelength of the incident light, and the angle of incidence [84]. A schematic of the Faraday and Kerr effects is shown in Figure 2.5.

The MOKE is a very useful technique and can be used in various applications. Some of them are: modern data storage technology in which 0s and 1s are determined by the polarization state of the reflected light [85], measuring the complete rotation of the magnetization during a hysteresis loop [86], determining the orientation of the magnetization vector during the reversal process in ferromagnetic films [87], detecting in-plane magnetization components in ferromagnetic materials [88], studying domain-wall dynamics in magnetic nanostructures [89], directly detecting nonlinear ferromagnetic resonance in thin films [90] and determining the current-induced spin-orbit torques [53,91]. The MOKE technique is commonly preferred over other techniques such as VSM, superconducting quantum interference device susceptometry, and magnetic force microscopy to obtain magnetization loops because

of its simplicity and capability to probe magnetization in small regions of the sample, and its sensitivity down to monolayer resolution [92].

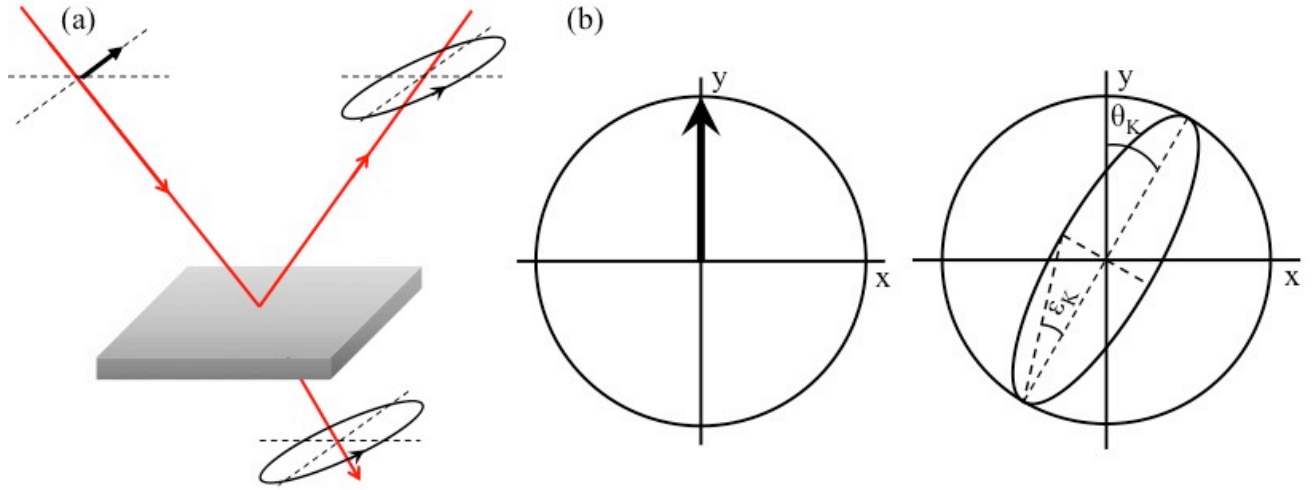


Figure 2.5: (a) A schematic of the magneto-optic Faraday (transmission) and Kerr (reflection) effects. (b) Linearly polarized light (left plot) transforms into rotated elliptically polarized light (right plot) due to the magneto-optic effects.

The magneto-optical properties of a material can be described by the permittivity tensor ϵ_{ij} , which can be expanded in the components of the magnetization \vec{m} acting on the material [93]:

$$\epsilon_{ij} = \epsilon_{ij}^{(0)} + K_{ijk} m_k + G_{ijkl} m_k m_l + \dots, \quad (2.2)$$

where the Einstein summation convention over the x , y , and z coordinates is used. The dielectric tensor $\epsilon_{ij}^{(0)}$ represents the components of the permittivity tensor in the absence of any magnetization \vec{m} , K_{ijk} is the linear magneto-optic tensor and G_{ijkl} is the quadratic magneto-optic tensor, which corresponds to a second-order MOKE response, often referred to as quadratic MOKE [94]. The linear response can be

separated into terms corresponding to relative orientations of the unit vector of the magnetization \hat{m} , plane of incidence (POI) and sample plane (SP), with polar geometry corresponding to $\hat{m} \parallel POI$ and $\hat{m} \perp SP$, longitudinal to $\hat{m} \parallel POI$ and $\hat{m} \parallel SP$ and transverse to $\hat{m} \perp POI$ and $\hat{m} \parallel SP$, as shown in Figure 2.6.

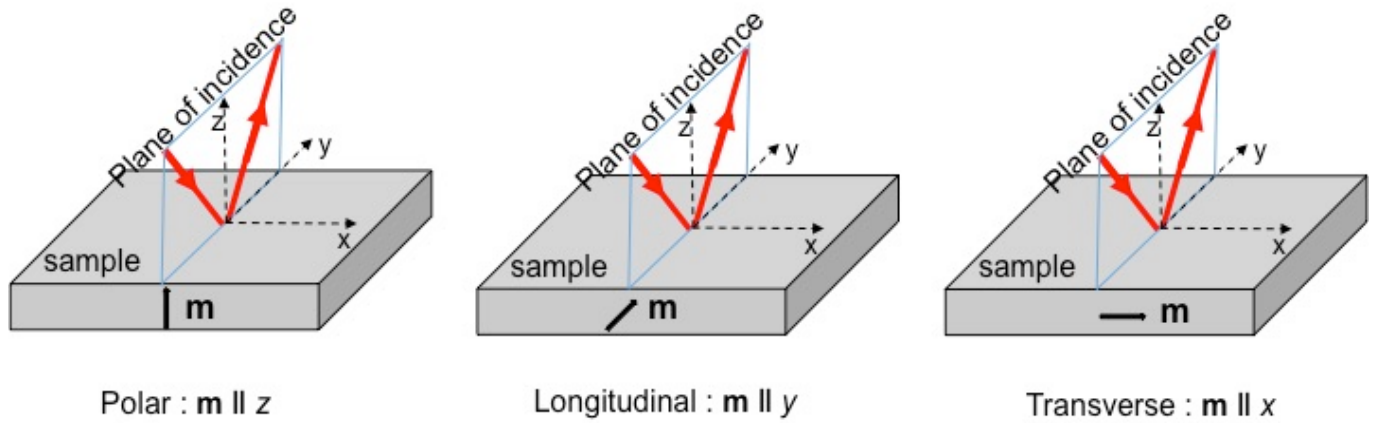


Figure 2.6: Three principle MOKE geometries. Polar: The magnetic field vector is perpendicular to the sample surface and parallel to the plane of incidence. Longitudinal: The magnetic field vector is parallel to both the sample surface and the plane of incidence. Transverse: The magnetic field vector parallel to the sample surface but perpendicular to the plane of incidence.

2.2.5.2 Theory of the Magneto-Optic Kerr Effect

Classical electromagnetics with Maxwell's equations can be used to describe the optical and magneto-optical properties of materials. Maxwell's equations describing the interaction of an electromagnetic wave with matter in cgs units are:

$$\begin{aligned}
\nabla \cdot \vec{D} &= 4\pi\rho \\
\nabla \cdot \vec{B} &= 0 \\
\nabla \times \vec{E} &= -\frac{1}{c} \frac{\partial \vec{B}}{\partial t} \\
\nabla \times \vec{H} &= \frac{4\pi}{c} \vec{J} + \frac{1}{c} \frac{\partial \vec{D}}{\partial t}
\end{aligned} \tag{2.3}$$

where electric displacement \vec{D} and magnetic inductance \vec{B} are connected to electric field \vec{E} and magnetic field \vec{H} by

$$\vec{D} = \epsilon \vec{E} \text{ and } \vec{B} = \mu \vec{H}, \tag{2.4}$$

where ϵ is the complex dielectric (permittivity) tensor and μ is the magnetic permeability. The dielectric tensor, a 3×3 matrix with each component complex, is used to obtain magneto-optic properties of materials such as refractive index, reflection coefficient and absorption coefficient:

$$\begin{pmatrix} D_x \\ D_y \\ D_z \end{pmatrix} = \begin{pmatrix} \epsilon_{xx} & \epsilon_{xy} & \epsilon_{xz} \\ \epsilon_{yx} & \epsilon_{yy} & \epsilon_{yz} \\ \epsilon_{zx} & \epsilon_{zy} & \epsilon_{zz} \end{pmatrix} \begin{pmatrix} E_x \\ E_y \\ E_z \end{pmatrix}. \tag{2.5}$$

For isotropic crystals with cubic symmetry, all diagonal terms are equal and the off-diagonal terms are zero if there is no magnetic field. If an external magnetic field is applied in the z -direction, the tensor has the form of [95]:

$$\epsilon = \begin{pmatrix} \epsilon_{xx} & \epsilon_{xy} & 0 \\ -\epsilon_{xy} & \epsilon_{xx} & 0 \\ 0 & 0 & \epsilon_{zz} \end{pmatrix}. \tag{2.6}$$

Optical properties of materials are related to diagonal elements of the dielectric tensor, whereas magneto-optical properties are related to the off-diagonal elements. The relation between the dielectric tensor and conductivity tensor σ_{ij} , is given by [96]:

$$\epsilon_{ij} = \delta_{ij} + \frac{4\pi i}{\omega} \sigma_{ij}, \quad (i, j = x, y, z) \quad (2.7)$$

where $\delta_{ij} = 1$ ($i = j$), 0 ($i \neq j$) and ω is the angular frequency.

Jones vectors are used to describe the polarization state of the light. The electric field vector describing a plane wave propagating in the z direction is given by $\vec{E} = \vec{E}_0 e^{i(kz - \omega t)}$ where $\vec{E}_0 = \tilde{E}_x \hat{x} + \tilde{E}_y \hat{y}$. Ignoring the common exponential terms, the electric field vector can be written as [97]:

$$\vec{E} = \begin{pmatrix} \tilde{E}_x \\ \tilde{E}_y \end{pmatrix} = \begin{pmatrix} |\tilde{E}_x| e^{i\phi_x} \\ |\tilde{E}_y| e^{i\phi_y} \end{pmatrix}. \quad (2.8)$$

This vector, depending on the phase relations between x and y components, can describe linearly or circularly polarized states. Linearly polarized light can be decomposed into two equal-amplitude circularly polarized fields of opposite handedness and different phase. Light linearly polarized in the x direction can be expressed as

$$\vec{E}_x = E_0 \begin{pmatrix} 1 \\ 0 \end{pmatrix} = \frac{E_0}{\sqrt{2}} (\vec{E}_+ + \vec{E}_-) = \frac{E_0}{\sqrt{2}} \left(\frac{1}{\sqrt{2}} \begin{pmatrix} 1 \\ -i \end{pmatrix} + \frac{1}{\sqrt{2}} \begin{pmatrix} 1 \\ i \end{pmatrix} \right) \quad (2.9)$$

where \vec{E}_+ (\vec{E}_-) is right-circularly (left-circularly) polarized components. The two circular polarizations interact differently with the magnetic material. When light is propagating through a medium, left-circularly polarized (LCP) light will drive electrons to move in left-circular motion. When a magnetic field is applied, the radius of the circular motion will be expanded by the Lorentz force law:

$$\vec{F} = q [\vec{E} + (\vec{v} \times \vec{B})]. \quad (2.10)$$

The opposite effect happens with right circularly polarized (RCP) light, resulting in a smaller radius of circular motion, as seen in Figure 2.7. The difference of the index of

refraction for RCP and LCP causes reflected light to rotate and the ellipticity of the polarization is affected by the different absorption rates of RCP and LCP [82].

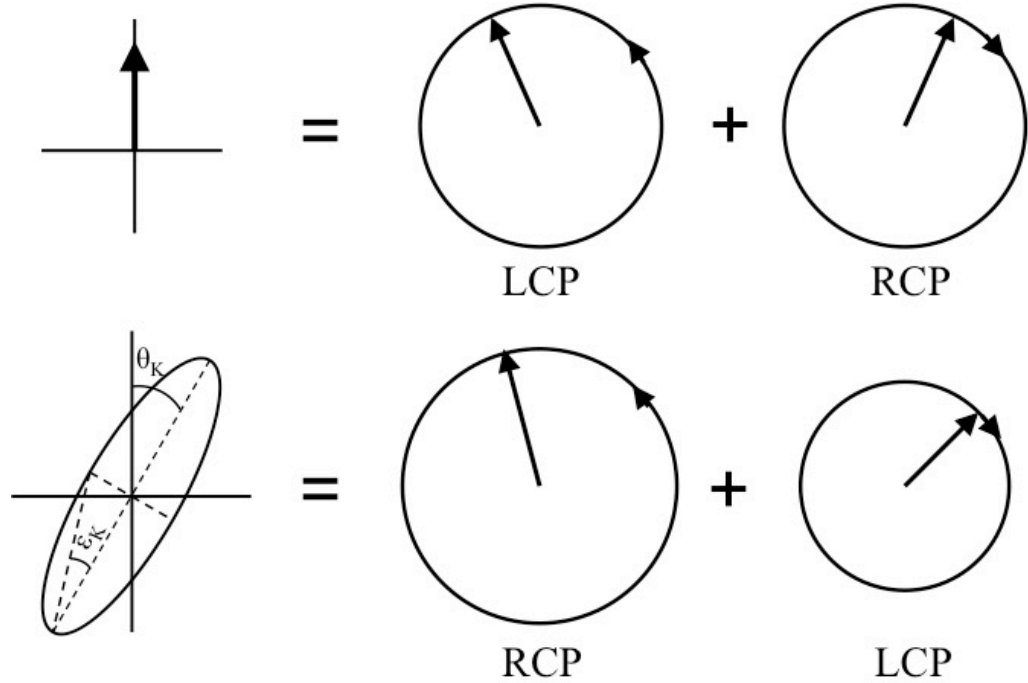


Figure 2.7: Linearly polarized light decomposes into LCP and RCP. The amplitude and the phase of the LCP and RCP changes after reflection, resulting in a rotated elliptical polarization.

The reflected polarization state can be described with the Fresnel reflection coefficients, which are defined as the ratio of reflected and incident electric fields:

$$\tilde{r}_{\pm} = r_{\pm} e^{i\varphi_{\pm}} = \frac{\vec{E}_{\pm}^{ref}}{\vec{E}_{\pm}^{in}}, \quad (2.11)$$

where \tilde{r}_{\pm} is the complex Fresnel reflection coefficient for right (+) and left (-) circularly polarized light. After reflection, the direction of light propagation is

changed to the $-z$ direction and right circular polarization is changed to left circular polarization and vice versa [98], so the reflected light becomes

$$\begin{aligned}\vec{E}^{ref} &= \frac{1}{\sqrt{2}}[\tilde{r}_- \vec{E}_+ + \tilde{r}_+ \vec{E}_-] e^{i(kz - \omega t)} \\ \vec{E}^{ref} &= \frac{E_0}{2} \left(\tilde{r}_+ \begin{bmatrix} 1 \\ i \end{bmatrix} + \tilde{r}_- \begin{bmatrix} 1 \\ -i \end{bmatrix} \right) = \frac{E_0}{2} \begin{bmatrix} \tilde{r}_+ + \tilde{r}_- \\ i(\tilde{r}_+ - \tilde{r}_-) \end{bmatrix} = E_0 \frac{(\tilde{r}_+ + \tilde{r}_-)}{2} \begin{bmatrix} 1 \\ i \frac{(\tilde{r}_+ - \tilde{r}_-)}{(\tilde{r}_+ + \tilde{r}_-)} \end{bmatrix}. \quad (2.12)\end{aligned}$$

Due to the non-zero y component in the reflected beam, the polarization plane is rotated and the linear polarization state is changed to elliptical. For a weak magneto-optic Kerr effect that results in a small change in polarization, the complex Kerr angle can be written as

$$\phi_K = \theta_K + i\epsilon_K \approx i \frac{(\tilde{r}_+ - \tilde{r}_-)}{(\tilde{r}_+ + \tilde{r}_-)}. \quad (2.13)$$

Given the reflection coefficient \tilde{r}_\pm expressed in terms of refractive indices and

dielectric constants is $\tilde{r}_\pm = \frac{\tilde{n}_\pm - 1}{\tilde{n}_\pm + 1} = \frac{\sqrt{\tilde{\epsilon}_\pm} - 1}{\sqrt{\tilde{\epsilon}_\pm} + 1}$ [99], we can obtain the complex Kerr angle

as

$$\tilde{\phi}_K = -\frac{\tilde{\epsilon}_{xy}}{(\tilde{\epsilon}_{xx} - 1)\sqrt{\tilde{\epsilon}_{xx}}}. \quad (2.14)$$

The complex Kerr angle can be expressed in terms of the optical conductivity using the relation (Eq. (2.7)) between dielectric constants and optical conductivity:

$$\tilde{\phi}_K = -\frac{\tilde{\sigma}_{xy}}{\tilde{\sigma}_{xx} \sqrt{1 + \frac{4\pi i}{\omega} \tilde{\sigma}_{xx}}}. \quad (2.15)$$

As seen in Eq. (2.14), large off-diagonal and small diagonal (low reflectivity) dielectric tensor elements are necessary for large Kerr angles.

When using the MOKE technique, reflection coefficients are described using s -polarized (perpendicular to the incident plane \Rightarrow vertically polarized) and p -polarized (parallel to the incident plane \Rightarrow horizontally polarized) light. Reflected electric fields can be represented as

$$\begin{pmatrix} E_s^r \\ E_p^r \end{pmatrix} = \begin{pmatrix} r_{ss} & r_{sp} \\ r_{ps} & r_{pp} \end{pmatrix} \begin{pmatrix} E_s^i \\ E_p^i \end{pmatrix} \quad (2.16)$$

where E_s^r and E_p^r are reflected s -polarized and p -polarized electric fields, E_s^i and E_p^i are incident s -polarized and p -polarized electric fields, respectively and

$r_{ss}, r_{sp}, r_{ps}, r_{pp}$ are the dielectric tensor depended reflection coefficients, defined as

$$r_{ss} = \frac{E_s^r}{E_s^i}, \quad r_{ps} = \frac{E_p^r}{E_s^i}, \quad r_{sp} = \frac{E_s^r}{E_p^i}, \quad r_{pp} = \frac{E_p^r}{E_p^i}. \quad \text{When } s\text{-polarized light is incident on the}$$

sample, a small portion is rotated to p -polarization through MOKE, whereas when the incident polarization is p -polarized, a small portion is rotated to s -polarization. This arises from the off-diagonal terms of the reflection matrix describing the MOKE. Complex Kerr angles ϕ_{ks}, ϕ_{kp} in terms of these reflection coefficients for s and p polarization are

$$\phi_{ks} = \frac{r_{ps}}{r_{ss}} \quad \text{and} \quad \phi_{kp} = \frac{r_{sp}}{r_{pp}}. \quad (2.17)$$

An expression for the Kerr angle can be derived following the formulation reported by You and Shin [100]. For light incident from a non-magnetic medium to a magnetized medium of arbitrary magnetization \vec{M} as seen in Figure 2.8, the dielectric tensor can be written as [101]

$$\varepsilon = \varepsilon_{xx} \begin{pmatrix} 1 & -iQm_z & iQm_y \\ iQm_z & 1 & -iQm_x \\ -iQm_y & iQm_x & 1 \end{pmatrix}, \quad (2.18)$$

where $Q = i \frac{\epsilon_{xy}}{\epsilon_{xx}}$ and $\epsilon_{zz} = \epsilon_{xx}$ assumed for simplicity. We set the magnetic permeability tensor to 1 at optical frequencies [102] and m_x, m_y, m_z are the direction cosines of the magnetization vector.

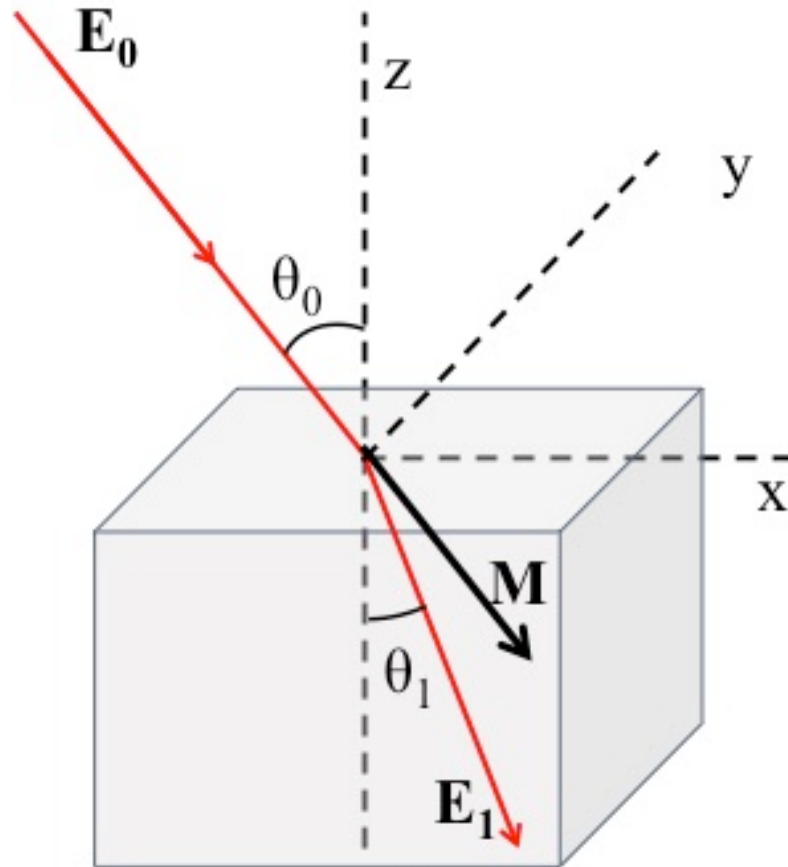


Figure 2.8: Light is incident from medium 0 to medium 1. The angle of incidence θ_0 and refraction θ_1 are related by Snell's law.

Reflection matrix elements derived by solving Maxwell's equations for the above dielectric tensor [101,103] can be written as:

$$\begin{aligned}
r_{pp} &= \frac{n_1 \cos \theta_0 - n_0 \cos \theta_1}{n_1 \cos \theta_0 + n_0 \cos \theta_1} - \frac{i2n_0 n_1 \cos \theta_0 \sin \theta_1 m_x Q}{n_1 \cos \theta_0 + n_0 \cos \theta_1}, \\
r_{sp} &= \frac{in_0 n_1 \cos \theta_0 (m_y \sin \theta_1 + m_z \cos \theta_1) Q}{(n_1 \cos \theta_0 + n_0 \cos \theta_1)(n_0 \cos \theta_0 + n_1 \cos \theta_1) \cos \theta_1}, \\
r_{ss} &= \frac{n_0 \cos \theta_0 - n_1 \cos \theta_1}{n_0 \cos \theta_0 + n_1 \cos \theta_1} \quad \text{and} \\
r_{ps} &= -\frac{in_0 n_1 \cos \theta_0 (m_y \sin \theta_1 - m_z \cos \theta_1) Q}{(n_1 \cos \theta_0 + n_0 \cos \theta_1)(n_0 \cos \theta_0 + n_1 \cos \theta_1) \cos \theta_1},
\end{aligned} \tag{2.19}$$

where $\theta_0, \theta_1, n_0, n_1$ are the angle of incidence, angle of refraction, the refractive index of the nonmagnetic medium 0, and that of the magnetic medium 1, respectively. For polar MOKE with a p -polarized incoming wave, the following relation can be obtained by substituting the $r_{pp}, r_{sp}, r_{ss}, r_{ps}$ in Eq. (2.17) and setting $m_x, m_x = 0$:

$$\left(\phi_K^p\right)^{polar} = \left(\frac{r_{sp}}{r_{pp}}\right)^{polar} = \frac{in_0 n_1 \cos \theta_0 m_z Q}{(n_0 \cos \theta_0 + n_1 \cos \theta_1)(n_1 \cos \theta_0 - n_0 \cos \theta_1)}. \tag{2.20}$$

We can get then the expression for longitudinal MOKE by setting $m_x, m_z = 0$:

$$\left(\phi_K^p\right)^{long} = \left(\frac{r_{sp}}{r_{pp}}\right)^{long} = \frac{in_0 n_1 \cos \theta_0 (n_1 \cos \theta_0 - n_0 \cos \theta_1) \tan \theta_1 m_y Q}{(n_0 \cos \theta_0 + n_1 \cos \theta_1)}. \tag{2.21}$$

By similar mathematical treatment, Kerr angles for s -polarized light for polar and longitudinal MOKE can be obtained. The derivation of these equations using Mathematica is given in Appendix A. As can be seen from Eq. (2.20) and Eq. (2.21), the polar signal is an even function whereas longitudinal MOKE is an odd function of the incident angle.

From a quantum-mechanical perspective, the magneto-optic Kerr effect is based on the simultaneous occurrence of the exchange interaction and spin-orbit coupling in a bulk ferromagnet [98,104,105]. We consider as an example a system where only vertical optical transitions are allowed and the selection rules $\Delta l = \pm 1$, $\Delta m_l = \pm 1$ for electric dipolar transitions are satisfied [106]. The condition $\Delta l = \pm 1$ indicates that only transitions between s and p levels or between p and d levels are allowed. The condition $\Delta m_l = \pm 1$ corresponds to transitions by left- and right- circularly polarized light. Figure 2.9 shows an energy diagram for optical transitions from an occupied degenerate initial d_{xz}, d_{yz} state ($l=2, m_l = \pm 1$) to an unoccupied final p_z state ($l=1, m_l = 0$) for a ferromagnet.

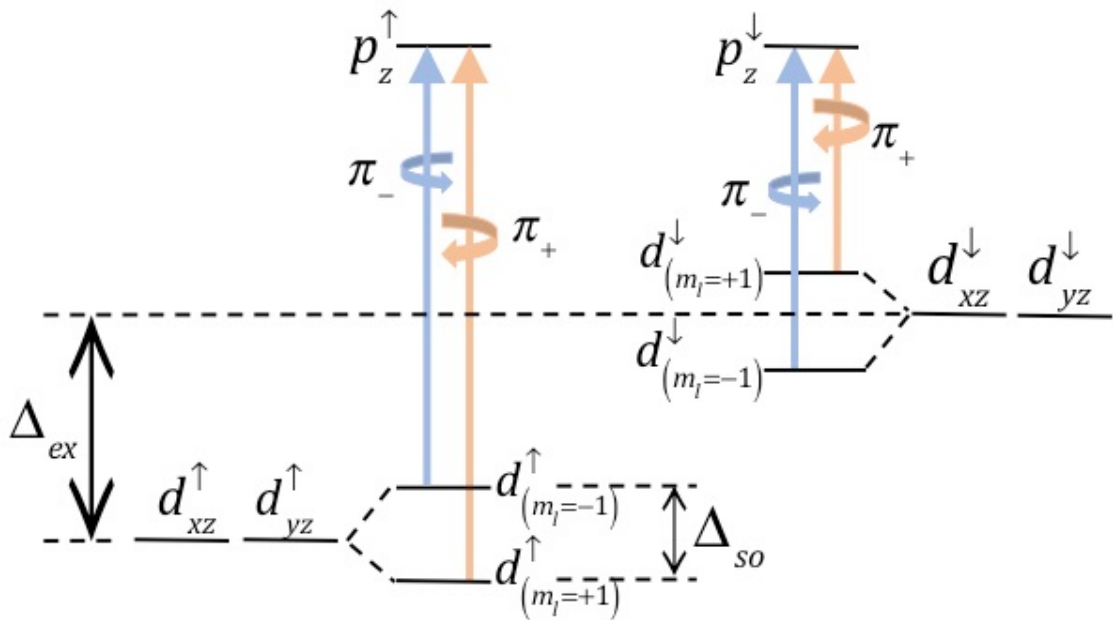


Figure 2.9: Sketch of the energy levels with exchange and spin-orbit interaction in a bulk ferromagnet showing the electric dipole transitions for left- and right-circular polarization.

The left-hand side shows the spin-up states and the right-hand side the spin-down states. The energy difference Δ_{ex} between the spin-up and spin-down states is due to the exchange interaction. The d_{xz} (d_{yz}) state splits into $d_{(m_l=-1)}^\uparrow$ ($d_{(m_l=+1)}^\uparrow$) in each spin state due to the spin-orbit interaction, resulting in an energy difference of Δ_{so} . For spin up, the energy of $d_{(m_l=+1)}^\uparrow$ is higher than the energy of $d_{(m_l=-1)}^\uparrow$. For spin down, the situation is reversed. Figure 2.10 shows the energy diagram of transitions for a bulk paramagnet. In this case, there is no exchange interaction so there is no splitting between spin-up and spin-down states. Adding contributions from spin-up and spin-down states leads to a vanishing Kerr signal.

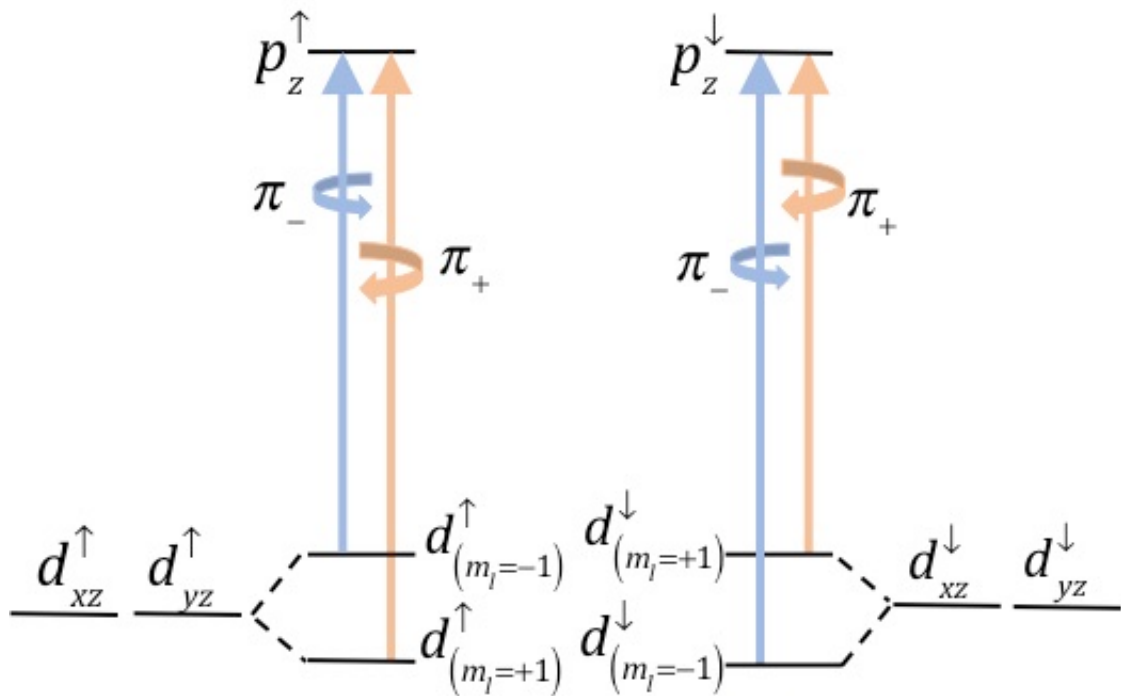


Figure 2.10: Sketch of the energy levels without exchange interaction in a bulk paramagnet, showing the electric dipole transitions for left- and right-circular polarization.

Electric dipole transitions for right- (π_+) and left- (π_-) circularly polarized light can be expressed as

$$\langle i|\pi_+|f\rangle = |\pi_+| \text{ and } \langle i|\pi_-|f\rangle = |\pi_-|. \quad (2.22)$$

For each spin state, the sum of the dipole matrix elements, $|\pi_+| + |\pi_-|$, gives the diagonal component of the optical conductivity, whereas the off-diagonal components correspond to the difference, $|\pi_+| - |\pi_-|$ [107]. The total conductivity is the sum of the conductivities for spin up and down states:

$$\sigma_{xx} = |\pi_+|^{\uparrow} + |\pi_-|^{\uparrow} + |\pi_+|^{\downarrow} + |\pi_-|^{\downarrow} \text{ and } \sigma_{xy} = |\pi_+|^{\uparrow} - |\pi_-|^{\uparrow} + |\pi_+|^{\downarrow} - |\pi_-|^{\downarrow}. \quad (2.23)$$

If there is no spin-orbit interaction, $|\pi_+|^{\uparrow} = |\pi_-|^{\uparrow}$ and $|\pi_+|^{\downarrow} = |\pi_-|^{\downarrow}$; so, the off-diagonal component of the conductivity cancels out for each spin state. Spin-orbit interaction is necessary for non-zero off-diagonal conductivity elements. If there is no exchange interaction, the energy difference between the spin-up and spin-down states is removed, so the relation between the electric dipole transitions for right- and left-circularly polarized light becomes $|\pi_+|^{\uparrow} = |\pi_-|^{\downarrow}$ and $|\pi_-|^{\uparrow} = |\pi_+|^{\downarrow}$. Then the sum of the off-diagonal conductivities from the spin-up and spin-down states cancels, leading to zero off-diagonal conductivity elements. The diagonal component of the conductivity remains without the spin-orbit and exchange interactions. Hence spin-orbit interactions and exchange splitting are essential to the existence of the magneto-optic Kerr effect.

REFERENCES

- [1] P. J. Kelly and R. D. Arnell, *Vacuum* **56**, 159 (2000).
- [2] M. Hughes, Semicore Equip. Inc. (2014).
- [3] J. E. Mahan, *Physical Vapor Deposition of Thin Films*, 1 edition (Wiley-Interscience, New York, 2000).
- [4] W. D. Sproul, D. J. Christie, and D. C. Carter, *Thin Solid Films* **491**, 1 (2005).
- [5] C. A. Mack, *SPIE* **Vol. 4440**, 59 (2001).
- [6] Oxford Instruments Plasma Technol. (2012).
- [7] A. Yamano, *Rigaku J.* **34**, (2018).
- [8] S. Foner, *J. Appl. Phys.* **79**, 4740 (1996).
- [9] Wikipedia Free Encycl. (n.d.).
- [10] L. Reimer, *Scanning Electron Microscopy : Physics of Image Formation and Microanalysis* (Springer, 1998).
- [11] W. H. Bragg, *Rev. Mod. Phys.* **3**, 449 (1931).
- [12] E. Hecht, *Optics*, 3rd Editio (Addison-Wesley Publishing Company, 1998).
- [13] P. Weinberger, *Philos. Mag. Lett.* **88**, 897 (2008).
- [14] W. J. Geerts, *A High Field Magneto-Optical Kerr Probe* (1999).
- [15] A. Khurshudov, in *Essent. Guid. to Comput. Data Storage*, 1st editio (Prentice Hall Ptr, 2001), pp. 201–216.
- [16] H. Ohldag, N. B. Weber, F. U. Hillebrecht, and E. Kisker, *J. Appl. Phys.* **91**, 2228 (2002).
- [17] P. Vavassori, *Appl. Phys. Lett.* **77**, 1605 (2000).

- [18] J. M. Florczak and E. D. Dahlberg, *J. Appl. Phys.* **67**, 7520 (1990).
- [19] C. Nistor, G. S. D. Beach, and J. L. Erskine, *Rev. Sci. Instrum.* **77**, 103901 (2006).
- [20] T. Gerrits, P. Krivosik, M. L. Schneider, C. E. Patton, and T. J. Silva, *Phys. Rev. Lett.* **98**, 207602 (2007).
- [21] X. Fan, H. Celik, J. Wu, C. Ni, K. Lee, V. O. Lorenz, and J. Q. Xiao, *Nat. Commun.* **5**, 3042 (2014).
- [22] X. Fan, A. R. Mellnik, W. Wang, N. Reynolds, T. Wang, H. Celik, V. O. Lorenz, D. C. Ralph, and J. Q. Xiao, *Appl. Phys. Lett.* **109**, 122406 (2016).
- [23] S. D. Bader, *J. Magn. Magn. Mater.* **100**, 440 (1991).
- [24] J. Hamrlová, J. Hamrle, K. Postava, and J. Pištora, *Phys. Status Solidi Basic Res.* **250**, 2194 (2013).
- [25] M. Buchmeier, R. Schreiber, D. E. Bürgler, and C. M. Schneider, *Phys. Rev. B* **79**, 64402 (2009).
- [26] P. N. Argyres, *Phys. Rev.* **97**, 334 (1955).
- [27] J. D. Jackson, *Classical Electrodynamics* (Wiley and Sons Inc, 1975).
- [28] G. R. Fowles, *Introduction to Modern Optics* (Holt, New York, 1975).
- [29] Z. Q. Qiu and S. D. Bader, *Rev. Sci. Instrum.* **71**, 1243 (2000).
- [30] W. Reim and J. Schoenes, in *Ferro-magnetic Mater. Vol. 5*, edited by K. H. J. Buschow and E. P. Wohlfarth (1990).
- [31] C. You and S. Shin, *Appl. Phys. Lett.* **69**, 1315 (1996).
- [32] R. P. Hunt, *J. Appl. Phys.* **38**, 1652 (1967).
- [33] P. S. Pershan, *J. Appl. Phys.* **38**, 1482 (1967).
- [34] J. Zak, E. R. Moog, C. Liu, and S. D. Bader, *J. Appl. Phys.* **68**, 4203 (1990).
- [35] T. Nakagawa, in *Compend. Surf. Interface Anal.* (Springer Singapore, Singapore, 2018), pp. 667–671.
- [36] J. L. Erskine and E. A. Stern, *Phys. Rev. B* **8**, 1239 (1973).

- [37] P. Bruno, Y. Suzuki, and C. Chappert, Phys. Rev. B **53**, 9214 (1996).
- [38] J. Park, Optical and Magneto-Optic Kerr Effects of MnBi, Ni₂MnGa, and Gd₅Si₂Ge₂, Iowa State University, 2004.

Chapter 3

QUANTIFYING INTERFACE AND BULK CONTRIBUTIONS TO SPIN-ORBIT TORQUE IN MAGNETIC BILAYERS

Spin-orbit interactions in heavy metal/ferromagnet (HM/FM) bilayer heterostructures have attracted considerable attention because they provide an efficient way to manipulate magnetization with current-driven spin-orbit torques (SOTs). An electric current generates a field-like spin-orbit torque (FT) and a damping-like spin-orbit torque (DT) on the magnetization. Two mechanisms have been proposed to explain the generation of SOTs: the Rashba-Edelstein effect due to interfacial spin-orbit coupling and the spin Hall effect (SHE) arising in the bulk of materials with strong spin-orbit coupling (SOC). Much effort has been dedicated to identifying the dominant mechanism of the SOTs. However, the underlying mechanism for the SOC-driven phenomena remains unsettled. In this chapter, we develop a sensitive SOT magnetometer based on the magneto-optic Kerr effect (MOKE) that measures the SOTs for CoFeB/Pt bilayers over a wide thickness range. We observe that the DT inversely scales with the ferromagnet thickness, and the FT has a threshold effect that appears only when the ferromagnetic layer is thinner than 1 nm. Through a thickness-dependence study with an additional copper insertion layer at the interface, we conclude that the dominant mechanism for the SOC-driven phenomena in this system is the SHE. However, there is also a distinct interface contribution, which comes from the Rashba effect.

3.1 Introduction

Recent advances in the electrical control of magnetism [1–8] are exciting in part because they may lead to new technologies for nonvolatile magnetic memory and logic devices [9,10]. Some of the mechanisms that are contenders to provide the highest- efficiency magnetic manipulation in practical device geometries involve current-induced torques arising from SOC, either in HM/FM bilayers [5,6,11,12] or topological insulator (TI)/FM bilayers [13,14]. The SOC-driven magnetization dynamics such as magnetization switching [6,11,15–18], high-frequency oscillation [19–22] domain-wall motion [8,23,24] and skyrmion manipulation [25,26] have been demonstrated and may find critical applications in magnetic memory and logic devices. Although these beneficial effects have been successfully demonstrated, researchers are still debating the underlying principle, as to whether the dominating mechanism arises from the HM/FM interface due to the Rashba effect or from the bulk of the HM due to the SHE. It has been theoretically predicted that both the Rashba effect and the SHE generate FT and DT on the magnetization, with only quantitative differences [27].

Progress in this field, both for fundamental scientific understanding and practical applications, requires convenient, quantitative techniques for measuring the strength and direction of the SOTs; techniques that can be applied to a wide range of material systems. At present, the workhorse methods for measuring such torques are based on using magnetotransport signals for detecting magnetic reorientations in response to an applied current. For example, second-harmonic Hall effect measurements [28] work well for measuring torques acting on a metallic magnetic layer with perpendicular magnetic anisotropy, but for magnets with in-plane anisotropy, the need to separate out thermally induced signals makes this technique

more difficult to apply [11,17,29]. Spin-torque ferromagnetic resonance (ST-FMR) [6] can be used for metallic magnets with either perpendicular or in-plane anisotropy, but for very thin magnetic layers, an artifact caused by spin pumping and the inverse spin Hall effect could in principle interfere with this method [30].

In this chapter, we develop a MOKE-based SOT magnetometer that sensitively detects the DT and FT. Combined with sensitive FT detection via the planar Hall effect (PHE) [11], we obtain the thickness dependence of DT and FT over a wide range of FM thicknesses. On the basis of this technique, we are also able to quantitatively determine the bulk and interface contributions to the overall SOI effect.

3.2 Sample Fabrication

The samples were deposited via magnetron sputtering. The deposition rates were 0.13 nm s^{-1} (Cu), 0.07 nm s^{-1} (Ti, Pt and $\text{Co}_{40}\text{Fe}_{40}\text{B}_{20}$) in an argon pressure of 4.5×10^{-3} Torr. The resistivities of these films measured at 10 nm are, respectively, $\rho_{\text{Cu}} (7.12 \mu\Omega\text{cm}) \ll \rho_{\text{Pt}} (21.18 \mu\Omega\text{cm}) \ll \rho_{\text{CoFeB}} (224.96 \mu\Omega\text{cm}) \ll \rho_{\text{Ti}} (1,963 \mu\Omega\text{cm})$. The samples for the thickness-dependent studies are fabricated by depositing wedge-shaped films 4 cm long. The thickness is extracted based on the position of the sample. Since the position control has a 2 mm error, the determination of the thickness has an error of 5% of the entire wedge thickness.

The samples used for DT measurements were lithographically patterned into a $50 \mu\text{m} \times 50 \mu\text{m}$ square connected by two contact pads consisting of Ti(5)/Cu(200)/Au(50). The samples used for FT measurements were patterned into Hall bar structures $500 \mu\text{m}$ wide and 3 mm long. The contact pads of the Hall bars are capped with Ti(5)/Cu(200)/Au(50).

3.3 Detection of DT and FT

Despite the different SOC origins of the interface Rashba effect and the SHE, the FT and DT generated from a current through the HM/FM bilayer can be described by the Landau–Lifshitz–Gilbert–Slonczewski (LLGS) equation,

$$\frac{d\vec{m}}{dt} = -\gamma\vec{m} \times \vec{H}_{eff} + \alpha\vec{m} \times \frac{d\vec{m}}{dt} + a\vec{m} \times \vec{\sigma} + b\vec{m} \times (\vec{\sigma} \times \vec{m}), \quad (3.1)$$

where \vec{m} is the normalized magnetization vector, γ is the gyromagnetic ratio, \vec{H}_{eff} is the total effective field including the external field \vec{H}_{ex} , anisotropy field \vec{H}_a and Oersted field \vec{h}_{Oe} generated from the current, α is the damping coefficient, $\vec{\sigma}$ is the spin polarization of spin current generated from charge current and is in-plane and orthogonal to the electric current, and a and b describe the FT and DT, respectively. In order to determine the magnitude of a and b , it is desirable to analyze the linear response of the magnetization vector in a saturated magnetization state to a small electric current. In this case, the magnetization is uniform and the Dzyaloshinskii–Moriya interaction can be neglected [31]. In a simplified scenario, where the magnetization of the FM layer is uniformly saturated in the film plane by an external field and an electric current is applied in the same direction, the effect from the SOC can be viewed as an in-plane effective field $\vec{h}_{FT} = -\frac{a}{\gamma}\vec{\sigma}$ and an out-of-plane effective field $\vec{h}_{DT} = -\frac{b}{\gamma}\vec{\sigma} \times \vec{m}$ [11]. This results in a current-induced magnetization

reorientation

$$\left\{ \begin{array}{l} \Delta m_x = \frac{h_{FT} + h_{Oe_in}}{H_{eff}} \\ \Delta m_y = \frac{h_{DT} + h_{Oe_out}}{H_{eff} + M_{eff}} \end{array} \right. \quad (3.2)$$

where $M_{\text{eff}} = M_s - \frac{2K_{\perp}}{M_s}$ arises from the demagnetizing effect, M_s is the saturation magnetization and K_{\perp} is the surface anisotropy energy density, and h_{Oe_in} and h_{Oe_out} are the in-plane and out-of-plane current-induced fields due to Ampere's law, respectively. By detecting the amount of magnetization reorientation, the FT and DT can be determined. The derivation of current-induced magnetization reorientation is given in Appendix B.

3.3.1 Detection of DT with the Polar MOKE

It is well known that MOKE microscopy can selectively detect each component of the magnetization by varying the incidence angle of the laser [32]. In particular, when the laser is incident normal to the surface, the laser polarization is only sensitive to the perpendicular magnetization (polar MOKE), making it an ideal technique to detect the out-of-plane magnetization reorientation and hence the effect of DT. The experimental setup is shown in Figure 3.1 (a).

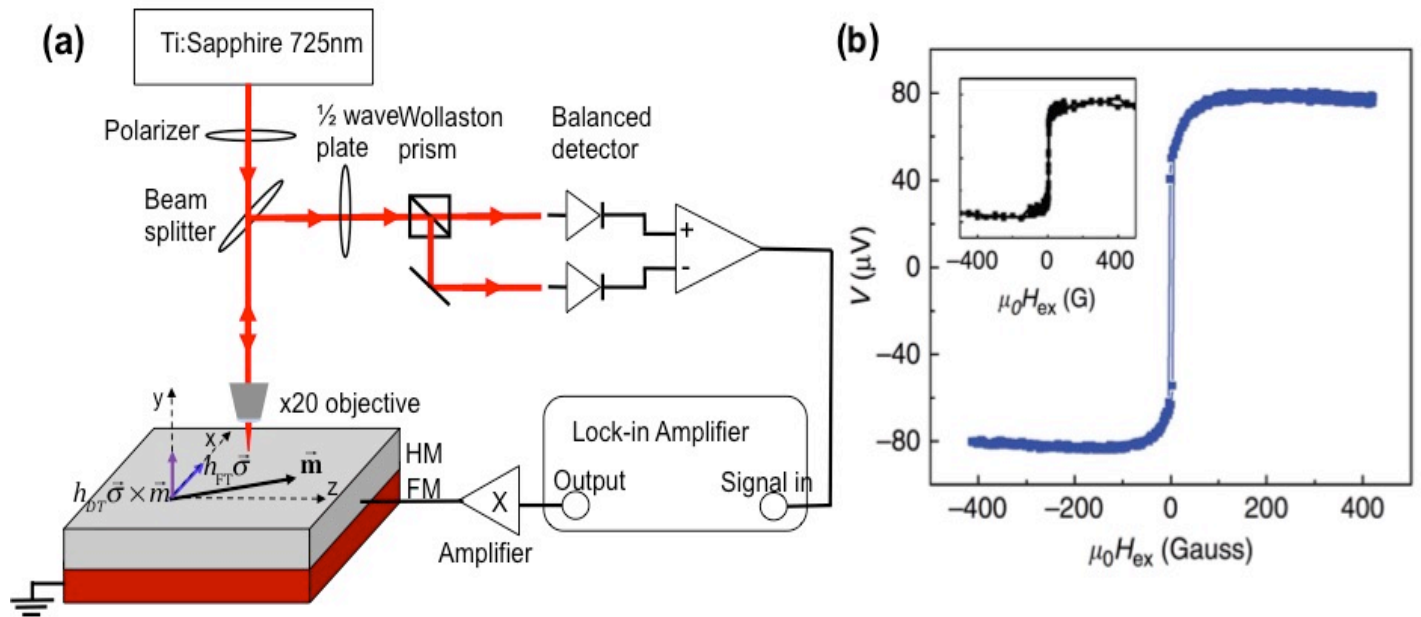


Figure 3.1: (a) Experimental setup for using polar MOKE to detect DT. A lock-in amplifier supplies an ac current through the sample along the z direction, which generates FT and DT that rotate the magnetization in-plane and out-of-plane from the xz plane, respectively. The reflected laser polarization changes with the magnetization of the sample because of MOKE. The change in the polarization is converted to a voltage signal through a series of optical components and a balanced detector. The voltage signal is detected by the same lock-in amplifier. (b) An example experimental result from Ti(1)/Co₄₀Fe₄₀B₂₀(0.85)/Pt(5) with a 12 mA bias current and 5 mW laser power. The inset is the magnetization hysteresis of the same sample.

The laser source used for the MOKE measurement is a mode-locked Ti:Sapphire laser working at 725 nm center wavelength. Light goes through a Glan Taylor polarizer with an extinction coefficient of $\sim 10^{-4}$ to set the polarization. For the DT measurement at normal incidence, a $\times 20$ objective is used to focus the laser on the sample and collimate the reflected beam. The error of the incidence angle is less than 0.1° . The reflected beam passes back through the objective and is reflected by a 70/30 beam splitter. It goes through a half-wave plate and the vertical and horizontal

polarization components are split by a Wollaston prism. The intensity of the two components are balanced by adjusting the half-wave plate. The HM/FM bilayer is patterned into a $50 \mu\text{m} \times 50 \mu\text{m}$ strip. When an alternating current I_{ac} is applied to the strip, the out-of-plane magnetization Δm_y of the FM changes based on Eq. (3.2), causing the polarization of the reflected laser to rotate because of the MOKE. The polarization components of the reflected laser are sent to a balanced detector, which outputs a voltage V that is proportional to the polarization rotation of the laser. Since the DT and FT are both proportional to the current, V is proportional to the applied current I_{ac} and can be measured by a lock-in amplifier. Figure 3.1 (b) shows an example result using Ti(1)/Co₄₀Fe₄₀B₂₀(0.85)/Pt(5). The curve resembles the magnetization hysteresis of the sample, consistent with Eq. (3.2), since $\vec{h}_{DT} = b/\gamma\vec{m} \times \vec{\sigma}$ switches sign as the magnetization switches and M_{eff} is much greater than the external field applied. On the other hand, \vec{h}_{Oe_out} remains a constant, which raises the entire curve. Figure 3.2 (a) and (b) show the linear responses to the bias current and laser power, which rules out contributions due to thermal effects.

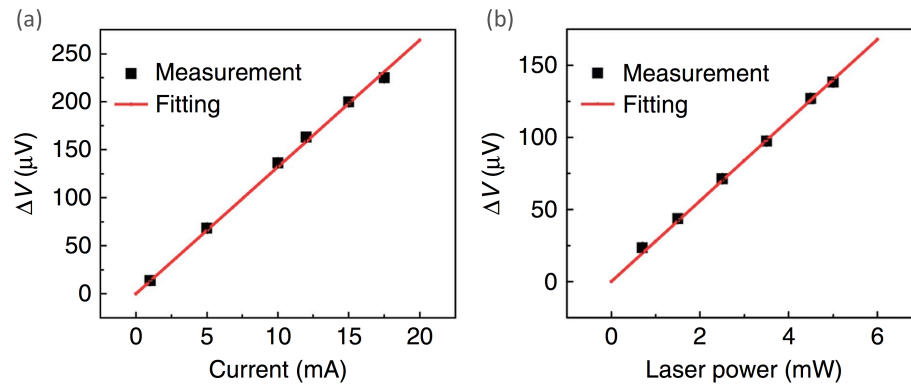


Figure 3.2 (a) The linear bias current dependence of the MOKE response. The laser power is kept at 5 mW with a beam radius of 2 mm, which corresponds to a power density of $4 \times 10^8 \text{ W} / \text{m}^2$. (b) The linear laser power dependence of the MOKE response. The bias current is kept at 10 mA, which corresponds to a current density of $4 \times 10^{10} \text{ A} / \text{m}^2$.

The magnitude of the DT is determined through a self-calibration method. The MOKE voltage at positive saturated field $V[+H_{\text{ex}}]$ and negative saturated field $V[-H_{\text{ex}}]$ are taken. The voltage signal corresponding to the DT and the out-of-plane Oersted field, which corresponds to the offset of the whole curve, can be extracted, respectively.

$$\begin{aligned}\Delta V_{DT} &= \frac{V[+H_{\text{ex}}] - V[-H_{\text{ex}}]}{2} \\ \Delta V_{\text{offset}} &= \frac{V[+H_{\text{ex}}] + V[-H_{\text{ex}}]}{2}\end{aligned}\quad (3.3)$$

Therefore, the magnitude of the DT can be correlated with the out-of-plane Oersted field, which is readily solvable using Ampere's law:

$$\frac{h_{DT}}{h_{\text{Oe.out}}} = \frac{V[+H_{\text{ex}}] - V[-H_{\text{ex}}]}{V[+H_{\text{ex}}] + V[-H_{\text{ex}}]}.\quad (3.4)$$

3.3.1.1 Extraction of DT from Polar MOKE

For a magnetic thin film with width w and thickness d , where $d \ll w$, the out-of-plane Oersted field distribution generated by an electric current flowing through the magnetic thin film is given by

$$h_{\text{Oe.out}}(x) = \frac{I_c}{2\pi w} \ln \frac{w-x}{x}\quad (3.5)$$

where I_c is the total electric current flowing through the film and $x \in [0, w]$ is the position perpendicular to the current direction. In the small field limit, the magnetization reorientation due to the current-induced out-of-plane Oersted field is given as

$$\Delta m_{y_{\text{Oe}}}(x) = \begin{cases} \frac{h_{\text{Oe.out}}(x)}{H_{\text{ex}} + M_{\text{eff}}}, & \text{if } 0 \leq x \leq w \\ 0, & \text{elsewhere,} \end{cases}\quad (3.6)$$

where H_{ex} is the external field and M_{eff} is the effective magnetization. It should be noted that in this derivation, we consider the magnetization reorientation only due to the local Oersted field by neglecting the exchange coupling between the nearest neighbors. This is a reasonable assumption since both the magnitude and gradient of the magnetic field are weak and the exchange energy is estimated to be six orders smaller than the Zeeman energy.

Owing to the finite size of the laser spot, the response of the Kerr rotation is calculated as the integration of the local magnetization reorientation weighted by the Gaussian function that describes the spatial distribution of the laser.

$$\Delta V_{\text{Offset}}(x, z) = \eta \frac{1}{2\pi r^2} \iint dx' dz' e^{-\frac{(x-x')^2 + (z-z')^2}{r^2}} \Delta m_{y, \text{Oe}}(x') \quad (3.7)$$

where r is the radius of the laser spot and η describes the sensitivity of MOKE response: $\eta = V_{\text{MOKE}} / \Delta m_y$.

Similarly, the MOKE response due to the DT-induced magnetization reorientation can be derived as

$$\Delta V_{\text{DT}}(x, z) = \eta \frac{1}{2\pi r^2} \iint dx' dz' e^{-\frac{(x-x')^2 + (z-z')^2}{r^2}} \frac{h_{\text{DT}}(x')}{H_{\text{ex}} + M_{\text{eff}}}, \quad (3.8)$$

where h_{DT} is uniform over the sample but switches sign when the magnetization switches.

We perform a line scan by keeping the laser position fixed and translating the sample along the x -direction. The DT is determined by fitting the line scan. By moving the sample along the x -direction with a motion stage, the laser beam scans across the sample along its middle section. An example curve is shown Figure 3.3 (a) and (c) using Ti(1)/Co₄₀Fe₄₀B₂₀(0.85)/Pt(5).

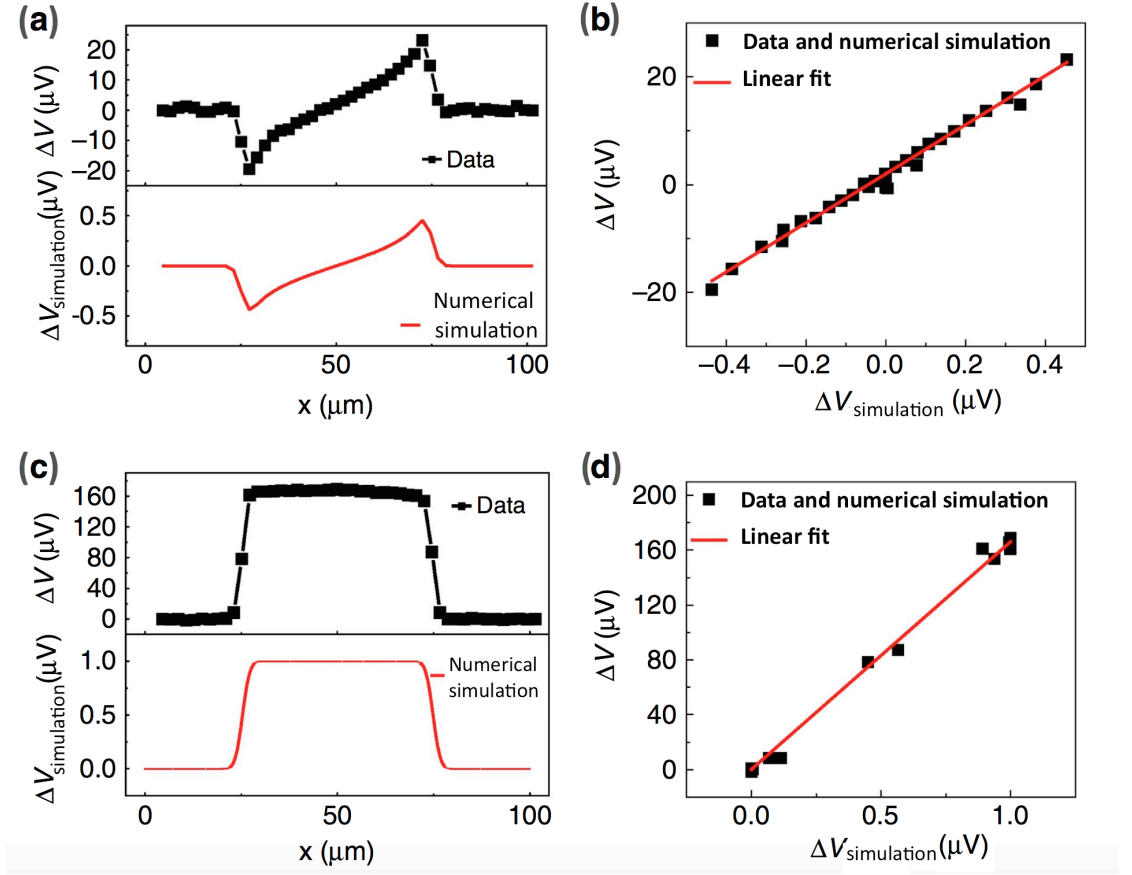


Figure 3.3: (a) Measured offset of the line scan $\Delta V = V[+H, x] + V[-H, x]$ (top, black squares) and the corresponding numerical simulation (bottom, red line) based on Eq. (3.7). (b) Plot of the y-axis values of the numerical simulation and the measured data against one another (black squares). The parameters in Eq. (3.7) are calibrated from a linear least-squares fit (red line). For this example curve, we find $\eta l_c / w = 45.5 \pm 1.2 \mu V$. (c) Measured DT signal from line scan $\Delta V = V[+H, x] - V[-H, x]$ (top, black squares) and the corresponding numerical simulation (bottom, red line) based on Eq. (3.8). (d) Data and simulation plotted against each other (black squares) and linear least-squares fit (red line), which gives the parameter for DT as $\eta h_{SOT} = 166 \pm 3 \mu V$. Therefore, the DT

coefficient is determined to be $\beta_T = \frac{h_{DT}}{j_{Pt}} = \frac{h_{DT}}{I_c / w} d_{Pt} = 18.3 \pm 0.7 \text{ nm}$.

We then numerically simulate the curves based on Eq. (3.7) and Eq. (3.8), also shown in Figure 3.3 (a) and (c). Here the unknown parameter is the starting position of the line scan, which can be obtained by aligning the experimental result and the fitting data. We then perform a linear regression algorithm on the experimental data and the corresponding simulation data to obtain the ratio between the two, as shown in Figure 3.3 (b) and (d). The magnitude of the DT is then calculated as

$$\frac{h_{DT}}{I_c / (2\pi w)} = \frac{\Delta V_{DT}(x, z) / \iint dx' dz' e^{-\frac{(x-x')^2 + (z-z')^2}{r^2}}}{\Delta V_{Offset}(x, z) / \iint dx' dz' e^{-\frac{(x-x')^2 + (z-z')^2}{r^2}} \ln \frac{w-x'}{x'}}. \quad (3.9)$$

In this example sample, the applied current is 12 mA. Since the resistivity of $\text{Co}_{40}\text{Fe}_{40}\text{B}_{20}$ (hereafter CoFeB) is much greater than that of Pt, we estimate that all of the current flows through the Pt, giving rise to a current density $j_{\text{Pt}} = 4.8 \times 10^{10} \text{ A/m}^2$.

We then determine the material-related DT coefficient $\beta_T = h_{DT} / j_{\text{Pt}} = 18.3 \pm 0.7 \text{ nm}$.

By assuming the DT is contributed by SHE and using the equation proposed by Ando

et al. [33] and Liu *et al.* [21], $\beta_{DT} = \frac{\hbar}{2e} \frac{\sigma_{\text{SH}}}{\mu_0 M_s d_{\text{CoFeB}}}$, we determine a spin Hall angle of

0.076 ± 0.007 for Pt, which is similar to reported results. Here the parameters used are $\mu_0 M_s = 1.6 \text{ T}$ and $d_{\text{CoFeB}} = 0.85 \pm 0.05 \text{ nm}$.

Figure 3.4 shows line scan curves for three samples: Ti(1)/CoFeB(0.75)/Pt(5), Ti(1)/CoFeB(0.95)/Cu(5), and Ti(1)/CoFeB(2)/Ta(5). The Pt(5) and Ta(5) samples have opposite spin Hall angle and hence opposite-sign DT line scan curves but the same out-of-plane Oersted field line scan curves. Cu(5) has a similar out-of-plane Oersted field line scan curve but a nearly 100 times weaker DT line scan curve, which agrees with the weak spin-orbit coupling in Cu. These results show the high sensitivity and universality of our MOKE technique.

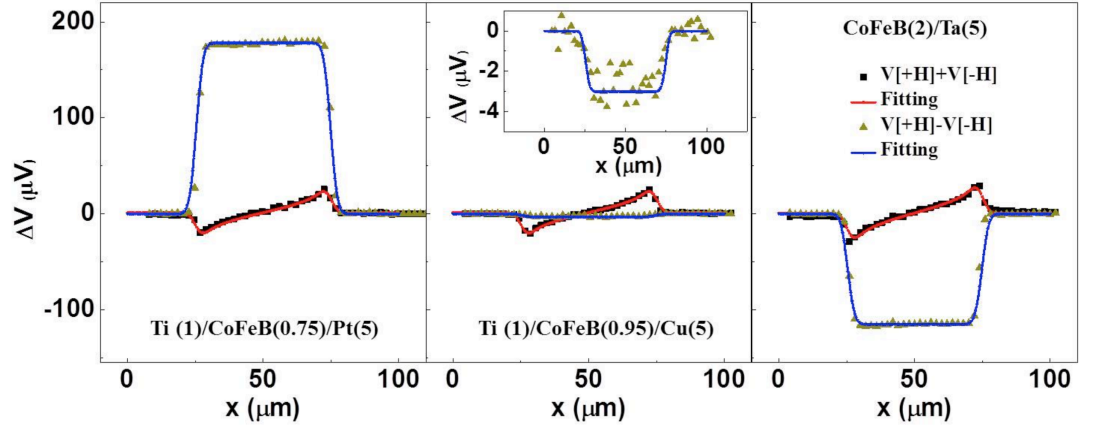


Figure 3.4: Representative DT measurement using polar MOKE for Ti/CoFeB/Pt, Ti/CoFeB/Cu, and CoFeB/Ta samples. The Ti/CoFeB/Cu (inset in the middle panel) shows very little DT signal, two orders smaller than those measured in CoFeB/Pt and CoFeB/Ta. The CoFeB/Pt and CoFeB/Ta has opposite sign to the DT, which is consistent with the opposite spin Hall angles of Pt and Ta.

The current densities through Pt, Cu, and Ta layers are, respectively, $5 \times 10^{10} \text{ A/m}^2$, $8 \times 10^{10} \text{ A/m}^2$, and $8 \times 10^{10} \text{ A/m}^2$. The extracted DT coefficients from these samples are $\beta_{DT} = 20.1 \pm 0.9 \text{ nm}$ for CoFeB/Pt, $\beta_{DT} = -0.2 \pm 0.05 \text{ nm}$ for CoFeB/Cu, and $\beta_{DT} = -9.2 \pm 0.5 \text{ nm}$ for CoFeB/Ta.

Owing to the fine resolution of this optical method, it is also possible to spatially image the spin-orbit torque. As shown in Figure 3.5, two-dimensional images of the out-of-plane magnetization reorientation due to the DT and Oersted field can be obtained. Reasonable uniformity is observed near the center of the sample.

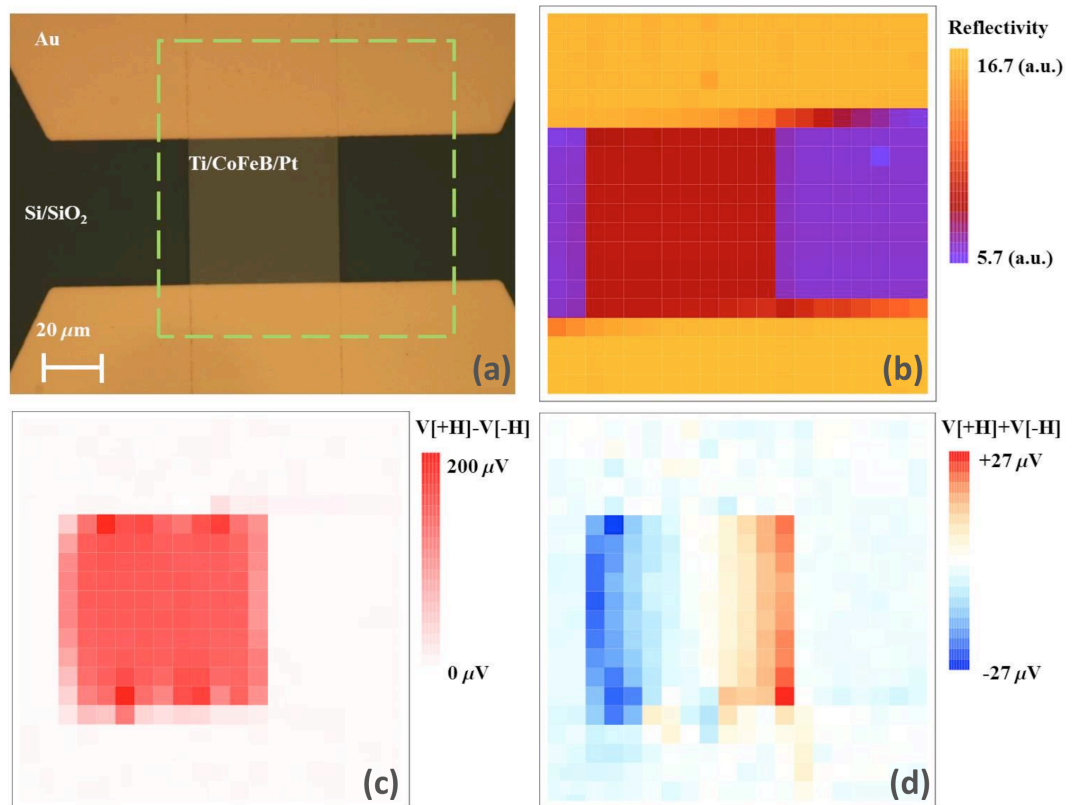


Figure 3.5: Two-dimensional raster scanning of the DT. (a) Image of the device under measurement. The imaging area is $100\ \mu\text{m} \times 100\ \mu\text{m}$ with a step size of $5\ \mu\text{m}$, illustrated by the green dashed line. (b) 2d imaging of the laser reflectivity as the laser scans the region. The area with Au, Si/SiO₂ and Ti/CoFeB/Pt has different reflectivity and can therefore be distinguished. (c) 2d imaging of the DT by taking the difference between the voltage response at positive saturated field and negative saturated field. In the middle regime, the magnitude is relatively uniform at $160 \pm 5\ \mu\text{V}$. The smearing of the boundary is due to the finite size of the laser beam diameter ($4\ \mu\text{m}$). (d) 2d imaging of the offset signal due to the out-of-plane Oersted field obtained by taking the average of the voltage response at positive saturated field and negative saturated field. As expected, the magnetization reorientation due to the out-of-plane Oersted field points toward opposite directions at the left side and right side of the sample. In the middle regime of the sample ($\sim 30\ \mu\text{m}$ vertical span), the distribution is reasonably uniform.

3.3.2 Detection of FT with Second-order Planar Hall Effect

We measure the magnitude of the current-induced FT using the second-order PHE method. As shown in Figure 3.7 (a), the Ti(1)/CoFeB(0.75)/Pt(5) sample is electrically detected in a Hall bar structure with in-plane magnetization orientation. A transverse voltage, V , arising from PHE and anomalous Hall effect (AHE), is measured:

$$V = V_{PHE} + V_{AHE} = wj\Delta\rho \frac{m_x m_z}{M_s^2} + wj\rho \frac{m_y}{M_s}, \quad (3.10)$$

where w is the Hall bar strip width, j is the dc current density, $\Delta\rho$ and ρ_{AHE} are the anisotropic and anomalous Hall resistivities, respectively, m_x, m_y, m_z are the magnetizations in the x, y, z direction, respectively, and M_s is the saturation magnetization. In a stationary state with saturated magnetization, the voltage contribution due to AHE can be neglected [11], so the detected transverse voltage is only due to PHE and is given by

$$V \approx wj\Delta\rho \sin\phi \cos\phi, \quad (3.11)$$

where ϕ is the in-plane magnetization rotation, which depends on H_{ext}, h_l (h_{FT} and h_{Oe}) as

$$\Delta\phi \approx \frac{\delta\phi[H_{ex}, h_l]}{\delta h_l} \frac{dh_l}{dj} j. \quad (3.12)$$

The second-order planar Hall voltage is taken at various small transverse magnetic fields for the purpose of calibration, and by simultaneously reversing the bias current, we find $\Delta V(h_{cal}) = V(+I, +h_{cal}, H_{ex}) + V(-I, -h_{cal}, H_{ex})$, where I is the applied current and h_{cal} is the applied calibration field. Under the small perturbation limit, the second-order PHE voltage ΔV is linearly proportional to the current-induced magnetization

reorientation Δm_x , as calculated in Eq. (3.9), and is therefore proportional to the transverse field, including FT, the in-plane Oersted field and the calibration field h_{cal} ,

$$: \Delta V \propto h_{FT} + h_{Oersted_in} + h_{cal}. \quad (3.13)$$

The second-order PHE voltage curves with different calibration fields are shown in Figure 3.6 (b). The curves have similar profile with different magnitudes.

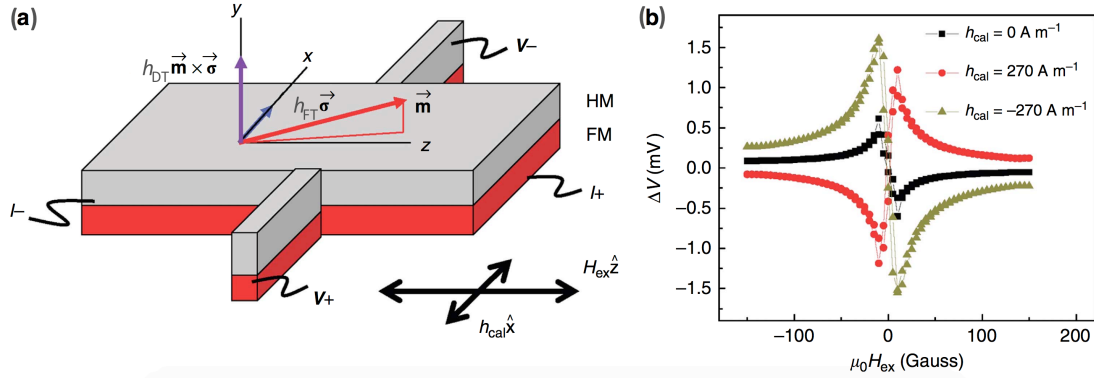


Figure 3.6: (a) Experimental setup for using the second-order PHE to detect the in-plane magnetization reorientation and the FT. A transverse field h_{cal} is applied to calibrate the response of the second order PHE voltage in order to quantify the FT. (b) Example measured second-order PHE curve of the Ti(1)/CoFeB(0.75)/Pt(5) under several calibration field strengths. The applied dc current is 50 mA.

The second-order PHE voltage ΔV is linearly proportional to the transverse field, which includes the effective field FT, in-plane Oersted field and calibration field h_{cal} , as seen in Eq. (3.17), so the FT can be extracted by comparing $\Delta V(h_{cal} = 0 \text{ A m}^{-1})$ and $\Delta V(h_{cal} = -270 \text{ A m}^{-1}) - \Delta V(h_{cal} = 270 \text{ A m}^{-1})$ using a linear regression algorithm, as shown in Figure 3.7 (a). Here the data at magnetic fields < 30 Gauss are not included in the fitting to satisfy the requirement of small angle perturbation.

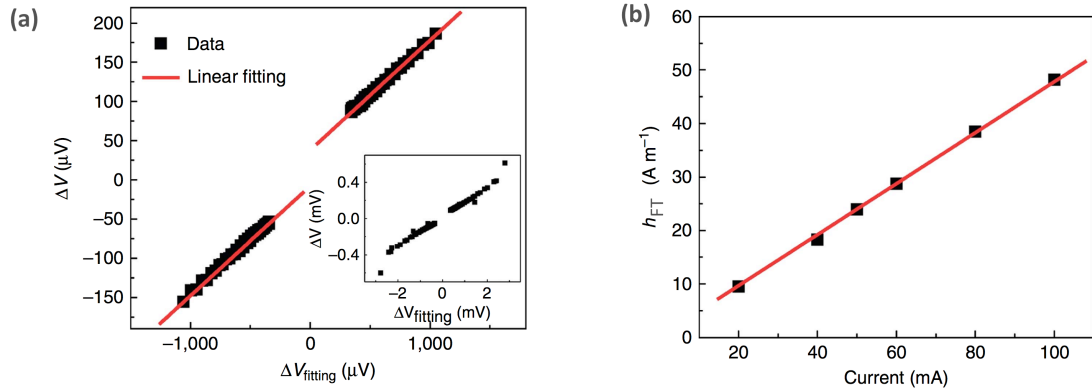


Figure 3.7: (a) Linear regression algorithm to extract the FT. The x-axis is obtained by $\Delta V_{fitting} = \Delta V(h_{cal} = -270 \text{ Am}^{-1}) - \Delta V(h_{cal} = 270 \text{ Am}^{-1})$ and y-axis is the $\Delta V(h_{cal} = 0 \text{ Am}^{-1})$ at the corresponding magnetic field. The positively saturated data and negatively saturated data are fit separately with the average slope taken as the ratio between the total current-induced field and the calibration field. The inset shows the overall curve at both saturated and unsaturated fields. (b) The linear bias current dependence of the FT indicates that the measurement is still in linear regime.

The data at positively saturated state and negatively saturated state are fit separately with the slope being $\frac{h_{FT} + h_{0e,in}}{540 \text{ Am}^{-1}} = 0.137 \pm 0.002$. An offset between the two linear fits

can be observed, which corresponds to the thermal effect and anomalous Hall effect due to out-of-plane magnetization reorientation [11]. By assuming most of the current flows through Pt layer, we can calculate the FT by subtracting the in-plane Oersted field $h_{0e,in} = \frac{I}{2w} = 50 \text{ Am}^{-1}$, where $w = 500 \mu\text{m}$ is the width of the Hall bar and

$I = 50 \text{ mA}$. The FT of Ti(1)/CoFeB(0.75)/Pt(5) is extracted to be $24.0 \pm 1.1 \text{ Am}^{-1}$ at a current density of $2 \times 10^{10} \text{ Am}^{-2}$ through Pt. We similarly determine the FT coefficient

$\beta_{FT} = \frac{h_{FT}}{j_{Pt}} = 1.20 \pm 0.05 \text{ nm}$. Figure 3.7 (b) shows the linear dependence of the FT on

the bias current applied, suggesting that the measurement is in the linear response regime.

3.3.3 Detection of FT with Longitudinal MOKE

MOKE can also detect the in-plane magnetization reorientation, Δm_x , with oblique angle incidence and therefore determine the FT, as shown in Figure 3.8 (a). For the FT measurement with oblique incidence, the Ti(1)/CoFeB(0.75)/Pt(5) sample with the Hall bar structure is used. In this case, two lenses are used to focus and collimate the laser. The incidence angle is set to be about 20°.

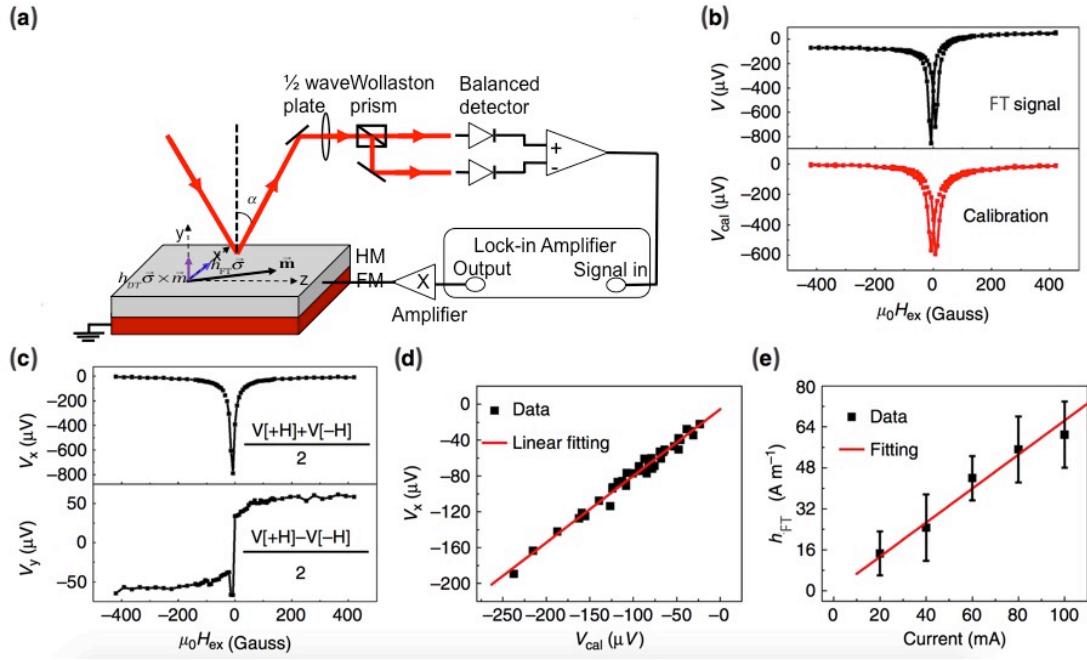


Figure 3.8: (a) Experimental setup for using longitudinal MOKE to detect the FT. The setup is identical with the polar MOKE shown in Figure 3.1 (a), except that the laser is obliquely incident on the sample in the xy plane. The incident angle is set to be about 20° . (b) Measured voltage from the lock-in amplifier when passing an ac current 100 mA through the sample ($500 \mu\text{m}$ in width) (black squares, top curve). The curve is asymmetric owing to the out-of-plane magnetization reorientation because of the DT. The calibration is performed by applying an ac current through a metallic wire behind the sample, which generates an Oersted field of $216 \pm 8 \text{ Am}^{-1}$ that drives the in-plane magnetization reorientation. As shown in the lower graph (red circles), the curve is symmetric since the calibration field has no torque-like term. (c) The magnetization reorientation because of the FT (top curve) and DT (bottom curve) can be separated by their different symmetries. (d) The magnitude of the FT is extracted using a linear regression algorithm by comparing the top curve in (c) and the calibration curve in (b). Only data between 50 Oe and 300 Gauss are used in the fitting, where the magnetization is well-saturated. (e) The extracted FT is linearly proportional to the bias current, suggesting that the measurement is still in the linear regime.

Owing to the nature of the oblique incidence setup, it is inevitable that signals due to the out-of-plane reorientation Δm_y also contribute: $V = V_x + V_y$, where $V_x \propto \Delta m_x$ and $V_y \propto \Delta m_y$. However, we are able to separate V_x from V_y based on their different symmetries; that is, the component V_x because of the FT and in-plane Oersted field is symmetric at positive and negative external field, while the component V_y because of DT switches sign when the magnetization switches. Moreover, the V_y because of the out-of-plane Oersted field can be viewed as constant background for thin magnetic films, as can be understood from Eq. (3.2). Therefore, we extract V_x by
$$V_x = \frac{V(+H_{\text{ex}}) + V(-H_{\text{ex}})}{2}.$$
 We also perform a calibration measurement by applying an ac magnetic field h_{cal} in the x -direction. The calibration field is applied by sending an ac electric current (1 A) through a flat wire (1 mm wide and 1 cm long) underneath the sample. The distance from the sample to the wire is about 650 ± 50 mm. The radiated field is calculated to be $216 \pm 8 \text{ Am}^{-1}$. In this case, the longitudinal MOKE signal V_{cal} only corresponds to the in-plane magnetization rotation and is therefore symmetric, as shown in the Figure 3.8 (b). The FT can be derived from $\frac{h_{\text{FT}} + h_{\text{Oersted_in}}}{V_x} = \frac{h_{\text{cal}}}{V_{\text{cal}}}$ using linear regression, as shown in Figure 3.8 (d). In the fit, only data at saturated magnetization states are used. In this example fitting, the ratio between the current-induced effective field and the calibration field is 0.74 ± 0.03 , which gives rise to a current-induced field of $h_{\text{FT}} + h_{\text{Oe_in}} = 160 \pm 16 \text{ Am}^{-1}$ at 100 mA applied bias current. After removing the 104 Am^{-1} Oersted field generated by the current, we obtain $h_{\text{FT}} = 56 \pm 16 \text{ Am}^{-1}$.

3.3.4 FM Layer Thickness Dependence of DT and FT

We measure the magnitude of the DT and FT for a series of samples Ti(1)/CoFeB(x)/Pt(5), where x spans from nominal 0.65 nm to 5.75 nm. The addition of Ti is for better adhesion and continuity of the ultrathin CoFeB layer. Adding the Ti layer does not introduce significant SOI because of its high resistivity and low atomic number. As shown in Figure 3.9 (a) and its inset, the DT coefficient follows the $1/d_{\text{CoFeB}}$ dependence and monotonically increases when the CoFeB gets thinner. On the other hand, the thickness dependence of the FT coefficient shows a threshold effect that remains near zero for thick CoFeB, but increases rapidly when CoFeB is thinner than 1 nm.

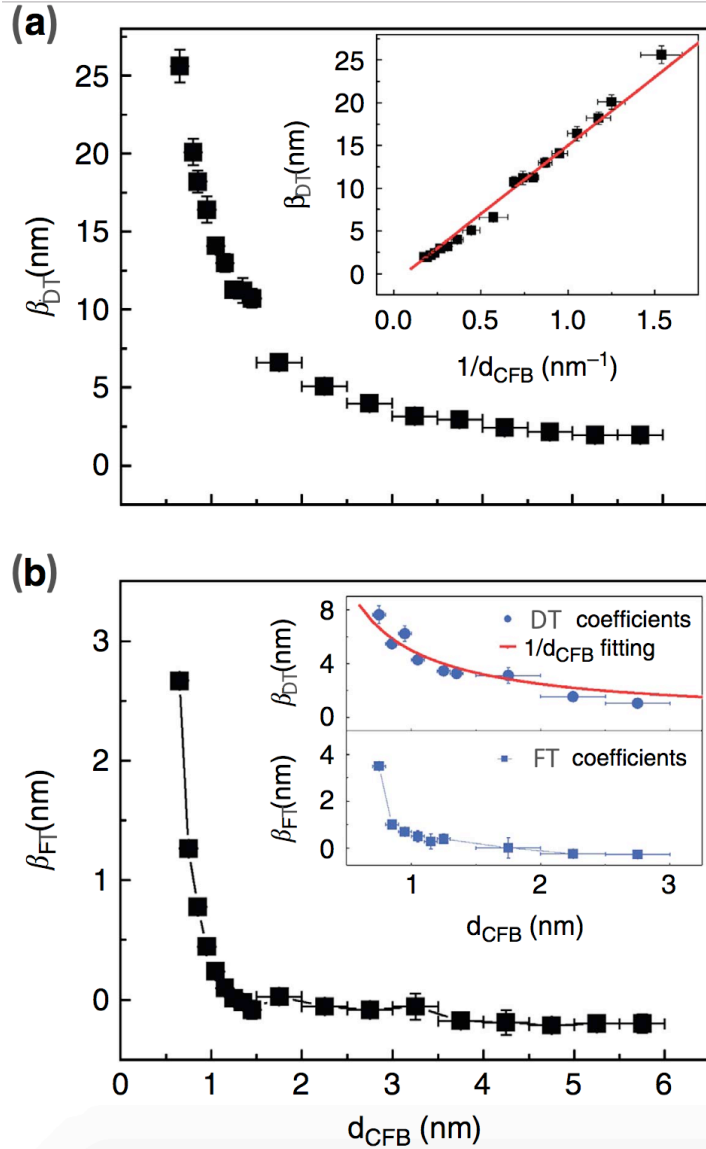


Figure 3.9: (a) Measured DT coefficient of Ti(1)/CoFeB(x)/Pt(5), where x spans from 0.65 to 5.75 nm. The inset shows the $1/d_{\text{CoFeB}}$ dependence of the DT coefficients. Here the error bar of the y-axis is obtained from the linear regression. The error bar of the x-axis is because of possible misalignment in fabricating the wedge-shaped sample. (b) Measured FT coefficient of the same series of samples as in (a). The FT remains nearly zero when CoFeB is thick and increases rapidly as the CoFeB becomes thinner than 1 nm. The inset shows the DT and FT of Ti(1)/CoFeB(x)/Cu(2)/Pt(5), where the direct interface between CoFeB and Pt is removed.

Haney *et al.* [27] computed the dependence of FT and DT on the thickness of the FM based on the Boltzmann equation considering both the bulk spin Hall effect in the HM and the Rashba effect at the FM/HM interface. The Boltzmann model calculations showed that the bulk spin Hall effect results in a constant scaled DT (Fig. 6a of Haney *et al.* [27]), which corresponds to a $1/d_{\text{CoFeB}}$ dependence. The calculated Rashba effect results in a decreasing scaled DT with decreasing FM thickness, corresponding to a much faster decay than the $1/d_{\text{CoFeB}}$ dependence in the absolute DT. This suggests that our results are consistent with the SHE mechanism rather than the Rashba effect mechanism. In the context of the SHE, the sharp increase in the FT for very thin FMs may be understood by the finite spin-dephasing length of the FM. In other words, this result is in accordance with the spin-dephasing effect in the spin torque transfer process [34] [35], where the spin Hall-induced spin current undergoes a Larmor precession because of the exchange interaction with the local magnetization. When the CoFeB is thinner than a characteristic spin-dephasing length, an effective magnetic field can be generated on the magnetization from the spin torque transfer process. Kim *et al.* [12] have recently performed a study of the DT and FT in a Ta/CoFeB/MgO system with perpendicular geometry. Their result on the FT also shows a monotonic increase with the reduction of CoFeB thickness. However, the sign of the FT is opposite to what one would expect from the SHE. Their result of the DT dependence on the CoFeB thickness is also different from what we measured. This may indicate that the dominant mechanism determining spin-orbit torques is different for different structures.

Although the results shown in Figure 3.9 imply that the dominant mechanism of spin-orbit torque in this bilayer is the bulk SHE, one has to quantify the interface

effect separately from the bulk effect in order to be conclusive. To this purpose, we further perform the same study on a series of samples of Ti(1)/CoFeB(x)/Cu(2)/Pt(5), where the 2-nm Cu removes the possible CoFeB/Pt interface effect without significantly reducing the spin current because of its weak spin-orbit coupling. We estimate the effective DT and FT coefficients in Ti(1)/CoFeB(x)/Cu(2)/Pt(5) by assuming that all currents flow through the Pt, which overestimates the current density and therefore would result in reduced values compared with those of the Ti(1)/CoFeB(x)/Pt(5) sample. As shown in the inset of Figure 3.9 (b), similar trends of the DT and FT are observed, which asserts the primary contribution of the SHE to the DT and FT. However, the ratio of the magnitude in the DT and FT coefficients is different between the samples with and without Cu, implying that there may be subtleties at the CoFeB/Pt interface. Therefore, we performed a more systematic study by varying the Cu layer thickness, discussed below.

3.3.5 Determination of the Interface Contribution

Both the Rashba effect and the SHE can produce the DT and FT [27,36–38]. The difference between the two effects depends quantitatively on the Rashba coefficient, spin Hall angle, spin dephasing length and even the current distribution between the layers [27]. However, the determination of these parameters has not been well-established and variations in these parameters may lead to different conclusions. Here we treat the controversy in a different way by separating the contribution due to the interface from that due to nonlocal effects mediated by spin current. By inserting a thin Cu layer in between CoFeB and Pt, the direct interface effect is removed. Therefore, the DT and FT detected in the Ti(1)/CoFeB(0.7)/Cu(x)/Pt(5) samples are only because of nonlocal effects, where the SOI occurs in either the bulk of the Pt

because of the SHE or the Cu/Pt interface, and the spin current diffuses into the CoFeB through the almost dissipationless Cu layer. In this case, despite the different current distributions because of the varying thicknesses of Cu, the ratio between the DT and FT, h_{DT}/h_{FT} , should remain the same as long as the Cu layer is thick enough to isolate the direct interface effect between CoFeB and Pt. If the CoFeB/Pt interface makes a significant contribution to the FT and DT, one should observe a deviation of h_{DT}/h_{FT} when the Cu layer is removed. The experimental data are shown in Figure

3.10 (a).

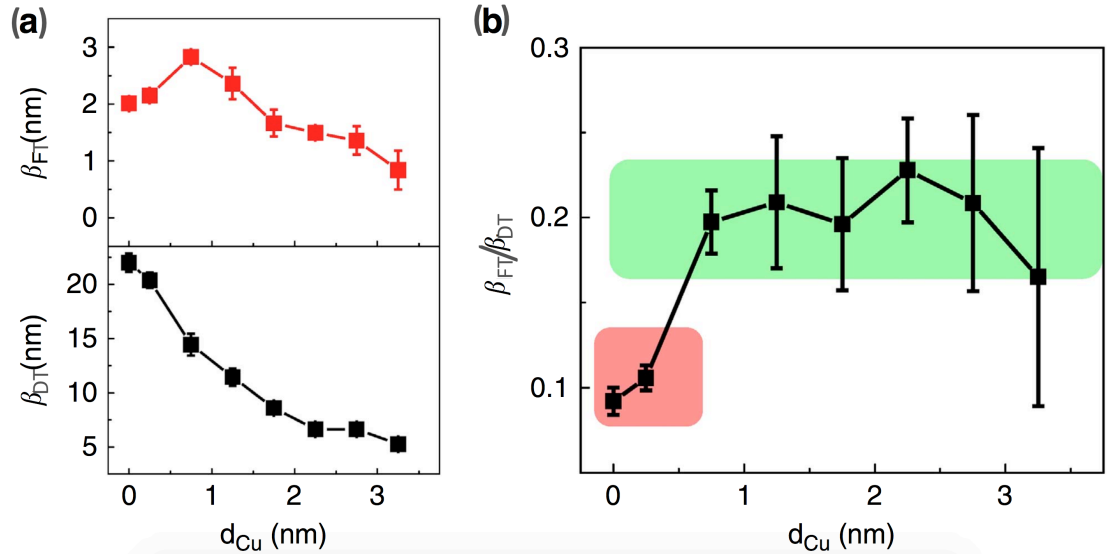


Figure 3.10: (a) Measured FT and DT coefficients in Ti(0.7)/CoFeB(0.7)/Cu(x)/Pt(5). The FT coefficient shows an increase with very thin copper insertion and then decreases as the copper layer gets thicker, while the DT coefficient shows a monotonic decay with increasing copper layer thickness. (b) The ratio between the FT and DT coefficients manifests two regimes as highlighted in the graph. In the green regime, where copper is thick enough to remove the interface effect between CoFeB and Pt, the β_{FT}/β_{DT} values are near 0.2. In the red regime, where copper is too thin to form continuous film, the β_{FT}/β_{DT} is lower suggesting that there exists an interface effect that produces a FT and DT based on a different mechanism from the effect of the nonlocal spin current.

The FT increases slightly with the insertion of a very thin Cu layer and reduces with increasing Cu thickness, while the DT exhibits a monotonic decay with Cu thickness. The overall reduction of the FT and DT is mainly because the Cu partially shorts the current through Pt. Another possible effect is that the Cu/CoFeB interface may have a different spin mixing conductance than the Pt/CoFeB interface, resulting in a different spin transfer torque efficiency [39,40]. Despite the significant reduction in both FT and DT, the ratio between the two remains near 0.2 when the Cu is thicker than 0.75 nm, as shown in Fig. 3.10 (b). This suggests that both the FT and DT have the same origin of nonlocal spin current. However, when the Cu is thinner than 0.75 nm, this ratio is lower than 0.2, indicating the existence of an interface effect. This interface effect may arise from the Rashba effect. Since the Rashba effect tends to produce a much larger effective field than torque, it is reasonable to estimate that the DT arises mostly from the SHE. Therefore, the pure spin Hall-induced effective field is estimated from the DT to be $\beta_{FT_spinHall} = \beta_{DT_spinHall} \times 0.2 = 4.4 \text{ nm}$ assuming the same FT/DT ratio as samples with Cu inserted. The Rashba field contribution with no Cu insertion is then estimated to be $\beta_{FT_Rashba} = \beta_{FT} - \beta_{FT_spinHall} = -2.4 \text{ nm}$.

We similarly perform a FT measurement study on the Ti(1)/Ni₈₀Fe₂₀(1.5)/Cu(0-5)/Pt(5) system. Although the magnitude of the FT is comparable to that of the Ti(1)/CoFeB(0.7)/Cu(0-5)//Pt(5), we observe monotonic decay of the FT with Cu insertion that differs from the samples using CoFeB. We speculate a correlation between the interface SOI and possible hybridization between Co and Pt [41]. In other words, the hybridization between Ni (or Fe) and Pt might be much weaker than that between Co and Pt so that no distinct interface effect is observed in Ni₈₀Fe₂₀/Pt samples. It should be pointed out that the Rashba effect is not

the only explanation for the reduction in the FT with direct contact of CoFeB and Pt. Another possible reason is the proximity effect [42], in which the interface of the Pt may become magnetic and effectively increase the thickness of the FM layer. Consequently, both the FT and DT decrease. Since the FT decreases more rapidly than the DT as the FM thickness increases, the ratio between the two decreases when the proximity effect effectively increases the thickness of the FM layer.

3.3.6 Summary

In Pt/CoFeB bilayers we show that the DT has $1/d$ dependence on the FM layer thickness and the FT has a threshold effect that appears only when the ferromagnetic layer is thinner than 1 nm. The fact that both DT and FT persist even with the insertion of a copper layer indicates that the spin Hall effect contributes to both the DT and FT. However, there is an important interface effect at the Pt/CoFeB interface that contributes additional DT and FT. This implies that another way to harness the spin-orbit coupling-induced magnetization switching is by engineering the interface. It should be emphasized that, although the spin Hall effect dominates the Pt/CoFeB system under this study, other systems with stronger interface SOI may be more influenced by the Rashba effect. The development of the spin-orbit torque magnetometer together with the Cu insertion method to isolate the interface allows quantitative determination of bulk and interface contributions in various systems.

REFERENCES

- [1] Myers, Ralph, Katine, Louie, and Buhrman, *Science* **285**, 867 (1999).
- [2] M. Weisheit, S. Fahler, A. Marty, Y. Souche, C. Poinsignon, and D. Givord, *Science* (80-.). **315**, 349 (2007).
- [3] Y.-H. Chu, L. W. Martin, M. B. Holcomb, M. Gajek, S.-J. Han, Q. He, N. Balke, C.-H. Yang, D. Lee, W. Hu, Q. Zhan, P.-L. Yang, A. Fraile-Rodríguez, A. Scholl, S. X. Wang, and R. Ramesh, *Nat. Mater.* **7**, 478 (2008).
- [4] T. Maruyama, Y. Shiota, T. Nozaki, K. Ohta, N. Toda, M. Mizuguchi, A. A. Tulapurkar, T. Shinjo, M. Shiraishi, S. Mizukami, Y. Ando, and Y. Suzuki, *Nat. Nanotechnol.* **4**, 158 (2009).
- [5] I. M. Miron, K. Garello, G. Gaudin, P.-J. Zermatten, M. V. Costache, S. Auffret, S. Bandiera, B. Rodmacq, A. Schuhl, and P. Gambardella, *Nature* **476**, 189 (2011).
- [6] L. Liu, C.-F. Pai, Y. Li, H. W. Tseng, D. C. Ralph, and R. A. Buhrman, *Science* (80-.). **336**, 555 (2012).
- [7] S. Emori, U. Bauer, S.-M. Ahn, E. Martinez, and G. S. D. Beach, *Nat. Mater.* **12**, 611 (2013).
- [8] K.-S. Ryu, L. Thomas, S.-H. Yang, and S. Parkin, *Nat. Nanotechnol.* **8**, 527 (2013).
- [9] C. Chappert, A. Fert, and F. N. Van Dau, *Nat. Mater.* **6**, 813 (2007).
- [10] J. A. Katine and E. E. Fullerton, *J. Magn. Magn. Mater.* **320**, 1217 (2008).
- [11] X. Fan, J. Wu, Y. Chen, M. J. Jerry, H. Zhang, and J. Q. Xiao, *Nat. Commun.* **4**, 1799 (2013).
- [12] J. Kim, J. Sinha, M. Hayashi, M. Yamanouchi, S. Fukami, T. Suzuki, S. Mitani, and H. Ohno, *Nat. Mater.* **12**, 240 (2013).
- [13] Y. Fan, P. Upadhyaya, X. Kou, M. Lang, S. Takei, Z. Wang, J. Tang, L. He, L.-

- T. Chang, M. Montazeri, G. Yu, W. Jiang, T. Nie, R. N. Schwartz, Y. Tserkovnyak, and K. L. Wang, *Nat. Mater.* **13**, 699 (2014).
- [14] A. R. Mellnik, J. S. Lee, A. Richardella, J. L. Grab, P. J. Mintun, M. H. Fischer, A. Vaezi, A. Manchon, E.-A. Kim, N. Samarth, and D. C. Ralph, *Nature* **511**, 449 (2014).
- [15] G. Yu, P. Upadhyaya, Y. Fan, J. G. Alzate, W. Jiang, K. L. Wong, S. Takei, S. A. Bender, L.-T. Chang, Y. Jiang, M. Lang, J. Tang, Y. Wang, Y. Tserkovnyak, P. K. Amiri, and K. L. Wang, *Nat. Nanotechnol.* **9**, 548 (2014).
- [16] X. Zhang, C. H. Wan, Z. H. Yuan, Q. T. Zhang, H. Wu, L. Huang, W. J. Kong, C. Fang, U. Khan, and X. F. Han, (2016).
- [17] K. Garello, I. M. Miron, C. O. Avci, F. Freimuth, Y. Mokrousov, S. Blögel, S. Auffret, O. Boulle, G. Gaudin, and P. Gambardella, *Nat. Nanotechnol.* **8**, 587 (2013).
- [18] C. Zhang, S. Fukami, H. Sato, F. Matsukura, and H. Ohno, *Appl. Phys. Lett.* **107**, 12401 (2015).
- [19] S. I. Kiselev, J. C. Sankey, I. N. Krivorotov, N. C. Emley, R. J. Schoelkopf, R. A. Buhrman, and D. C. Ralph, *Nature* **425**, 380 (2003).
- [20] L. Liu, C.-F. Pai, D. C. Ralph, and R. A. Buhrman, *Phys. Rev. Lett.* **109**, 186602 (2012).
- [21] L. Liu, T. Moriyama, D. C. Ralph, and R. A. Buhrman, *Phys. Rev. Lett.* **106**, 36601 (2011).
- [22] V. E. Demidov, S. Urazhdin, H. Ulrichs, V. Tiberkevich, A. Slavin, D. Baither, G. Schmitz, and S. O. Demokritov, *Nat. Mater.* **11**, 1028 (2012).
- [23] P. P. J. Haazen, E. Murè, J. H. Franken, R. Lavrijsen, H. J. M. Swagten, and B. Koopmans, *Nat. Mater.* **12**, 299 (2013).
- [24] I. M. Miron, T. Moore, H. Szambolics, L. D. Buda-Prejbeanu, S. Auffret, B. Rodmacq, S. Pizzini, J. Vogel, M. Bonfim, A. Schuhl, and G. Gaudin, *Nat. Mater.* **10**, 419 (2011).
- [25] W. Jiang, P. Upadhyaya, W. Zhang, G. Yu, M. B. Jungfleisch, F. Y. Fradin, J. E. Pearson, Y. Tserkovnyak, K. L. Wang, O. Heinonen, S. G. E. te Velthuis, and A. Hoffmann, *Science* (80-.). **349**, 283 (2015).
- [26] G. Yu, P. Upadhyaya, X. Li, W. Li, S. K. Kim, Y. Fan, K. L. Wong, Y.

- Tserkovnyak, P. K. Amiri, and K. L. Wang, *Nano Lett.* **16**, 1981 (2016).
- [27] P. M. Haney, H.-W. Lee, K.-J. Lee, A. Manchon, and M. D. Stiles, (2013).
- [28] J. A. Katine and E. E. Fullerton, *J. Magn. Magn. Mater.* **320**, 1217 (2008).
- [29] C. O. Avci, K. Garello, M. Gabureac, A. Ghosh, A. Fuhrer, S. F. Alvarado, and P. Gambardella, *Phys. Rev. B* **90**, 224427 (2014).
- [30] E. Saitoh, M. Ueda, H. Miyajima, and G. Tatara, *Appl. Phys. Lett.* **88**, 182509 (2006).
- [31] T. Moriya, *Phys. Rev. Lett.* **4**, 228 (1960).
- [32] Z. Q. Qiu and S. D. Bader, *Rev. Sci. Instrum.* **71**, 1243 (2000).
- [33] K. Ando, S. Takahashi, K. Harii, K. Sasage, J. Ieda, S. Maekawa, and E. Saitoh, *Phys. Rev. Lett.* **101**, 36601 (2008).
- [34] S. Zhang, P. M. Levy, and A. Fert, *Phys. Rev. Lett.* **88**, 236601 (2002).
- [35] J. Zhang, P. Levy, S. Zhang, and V. Antropov, *Phys. Rev. Lett.* **93**, 256602 (2004).
- [36] D. A. Pesin and A. H. MacDonald, *Phys. Rev. B* **86**, 14416 (2012).
- [37] X. Wang and A. Manchon, *Phys. Rev. Lett.* **108**, 117201 (2012).
- [38] K.-W. Kim, S.-M. Seo, J. Ryu, K.-J. Lee, and H.-W. Lee, *Phys. Rev. B* **85**, 180404 (2012).
- [39] Y. Tserkovnyak, A. Brataas, and G. E. W. Bauer, *Phys. Rev. B* **66**, 224403 (2002).
- [40] J. Bass and W. P. Pratt, *J. Phys. Condens. Matter* **19**, 183201 (2007).
- [41] N. Nakajima, T. Koide, T. Shidara, H. Miyauchi, H. Fukutani, A. Fujimori, K. Iio, T. Katayama, M. Nývlt, and Y. Suzuki, *Phys. Rev. Lett.* **81**, 5229 (1998).
- [42] S. Y. Huang, X. Fan, D. Qu, Y. P. Chen, W. G. Wang, J. Wu, T. Y. Chen, J. Q. Xiao, and C. L. Chien, *Phys. Rev. Lett.* **109**, 107204 (2012).

Chapter 4

ALL-OPTICAL VECTOR-RESOLVED MEASUREMENT OF SPIN-ORBIT-INDUCED TORQUES USING BOTH POLAR AND QUADRATIC MAGNETO-OPTIC KERR EFFECTS

In this chapter, we demonstrate that the MOKE with normal incidence light can be used to obtain quantitative optical measurements of both components of spin-orbit-induced torque (both the DT and FT) in HM/FM bilayers. This is achieved by analyzing the polar Kerr effect as well as the quadratic Kerr effect. The two effects can be distinguished by properly selecting the polarization of the incident light. We use this all-optical technique to determine the SOTs generated by a series of Pt/Permalloy ($\text{Ni}_{81}\text{Fe}_{19} = \text{Py}$) samples, finding values in excellent agreement with spin-torque ferromagnetic resonance (ST-FMR) measurements.

4.1 Introduction

The MOKE has been widely used for studying spin accumulation and magnetization in thin films [1–3]. In the previous chapter, we showed that conventional polar MOKE with normal light incidence can be used to accurately measure the DT component of the current-induced magnetic reorientation, and we have also shown that the longitudinal MOKE with oblique-angle light incidence can be used for measuring the FT component. Thus to measure both FT and DT components using polar and longitudinal MOKE requires measurements at both normal and oblique-angle light incidence. Recently, Montazeri *et al.* demonstrated the existence of a quadratic MOKE response with normal light incidence [4]. In this

chapter, we present a technique to measure and separate the polar and quadratic MOKE responses with normally incident light to detect DT and FT. We study a series of Pt/Py bilayers to verify the accuracy of this method.

4.2 Sample Fabrication

We demonstrate MOKE-based spin-torque magnetometry using in-plane magnetized substrate/Pt(6nm)/Py(d_{py}) bilayers, with d_{py} ranging from 2 to 10 nm. The bilayers were grown at room temperature on c-axis epi-ready sapphire substrates in a magnetron sputtering system with a base pressure of 2×10^{-9} Torr. After deposition of the Py, 2 nm of Al was deposited and oxidized to form a protective barrier. For the sample of Pt (6 nm)/Py (8 nm), $\mu_0 M_s = 0.87$ T as measured by vibrating sampling magnetometry, $\mu_0 H_{\text{anis}} = 0.23$ mT, and $\mu_0 H_{\text{anis}\perp} = 40$ mT as extracted from ferromagnetic resonance.

4.3 Determination of Polar and Quadratic MOKE signals

The MOKE can be described as arising from a magnetization-dependent permittivity tensor, which can be expressed as a Taylor series in the components of the magnetization unit vector, \vec{m} [5]

$$\epsilon_{ij}(\vec{m}) = \epsilon_{ij}^{(0)} + K_{ijk} m_k + G_{ijkl} m_k m_l + \dots \quad (4.1)$$

where the Einstein summation convention over the x , y , and z coordinates is used. The dielectric tensor $\epsilon_{ij}^{(0)}$ represents the components of the permittivity tensor in the absence of magnetization \vec{m} . When light interacts with a magnetic material, the light polarization will change depending on the magnetization orientation. The second term on the right side of Eq. (4.1) generates the first-order MOKE that encompasses the well-known polar, longitudinal, and transverse MOKE responses [6]. The third term

on the right side of Eq. (4.1) leads to a second-order MOKE response, which is often referred to as quadratic MOKE [7]. This term is in general not negligible.

For the case of normally incident light with linear polarization, the rotation of the polarization angle due to the magnetization can be written as [8]

$$\Psi(m) = \alpha_{polar} m_z + \beta_{quadratic} m_x m_y + \dots \quad (4.2)$$

where the z direction is perpendicular to the magnetic film plane, the x direction is parallel to the plane of the incident polarization, and α_{polar} and $\beta_{quadratic}$ are the coefficients for the polar MOKE and quadratic MOKE responses, respectively. If we define θ and ϕ as the polar and azimuthal angles of the magnetization and ϕ_{pol} as the angle of the plane of polarization, then Eq. (4.2) can be rewritten as

$$\Psi(m) = \alpha_{polar} \cos\theta + \frac{1}{2} \beta_{quadratic} \sin^2\theta \sin\left[2(\phi - \phi_{pol})\right] \quad (4.3)$$

As seen in Eq. (4.3), the polar MOKE response does not depend on the polarization direction, while the quadratic MOKE depends on the polarization angle as $\propto \sin\left[2(\phi - \phi_{pol})\right]$. Therefore, by controlling the polarization of the incident light, one can conveniently separate the two signals that are proportional to m_z and $m_x m_y$ and thus measure the current-induced magnetization rotation that results in changes to any of the magnetization components. Polar MOKE can be distinguished from the quadratic MOKE by tuning the angle of polarization of the light. If circularly polarized incident light is used, the polar MOKE component yields no polarization change, while the quadratic MOKE changes the polarization from circular to slightly elliptical.

As we have shown in Chapter 3, to first order for an in-plane-magnetized sample, the current-induced DT (changing θ) and FT (changing ϕ) is written as

$$\left\{ \begin{array}{l} \Delta\theta = \frac{h_{DT} + h_{Oe_out}}{H_{ex} + H_{anis} - H_{anis\perp} + M_s} \\ \Delta\phi = \frac{h_{FT} + h_{Oe_in}}{H_{ex} + H_{anis}} \end{array} \right. \quad (4.4)$$

where H_{anis} is the in-plane anisotropy field (assumed to be in the x direction), $H_{anis\perp}$ is any out-of-plane anisotropy field due to interface or crystalline anisotropy, and M_s is the saturation magnetization. For an ordinary transition-metal ferromagnet like Py, the in-plane anisotropy is negligible, and M_s is much larger than any of the other field terms. So, the change in the polar MOKE signal ($\propto \Delta\theta$) should be approximately independent of applied field for $H_{ex} \ll M_s$ while the current-induced change in the quadratic MOKE signal ($\propto \Delta\phi$) should scale approximately as $1/H_{ex}$.

Our MOKE measurements of the current-induced magnetization reorientation are conducted using the experimental geometry shown in Figure 4.1. We analyze the Kerr rotations of the light polarization using the optical bridge apparatus with a mode-locked Ti:Sapphire laser working at 780 nm center wavelength. We use a half wave plate (labeled HWP-1) and a quarter-wave plate (labeled QWP-1) to compensate a slight birefringence of the beam splitter and ensure that the light is initially linearly polarized along the x -axis when incident onto HWP-2 or QWP-2. To allow measurements in which linearly polarized light is incident on the bilayer and the polarization angle of the light can be adjusted relative to the sample magnetization, we rotate the light polarization by rotating the principle axis of a half wave plate (HWP-2) with respect to the x -axis. A $\times 20$ objective focuses the laser to a beam spot close to the center of the sample with a radius of approximately $2\ \mu m$.

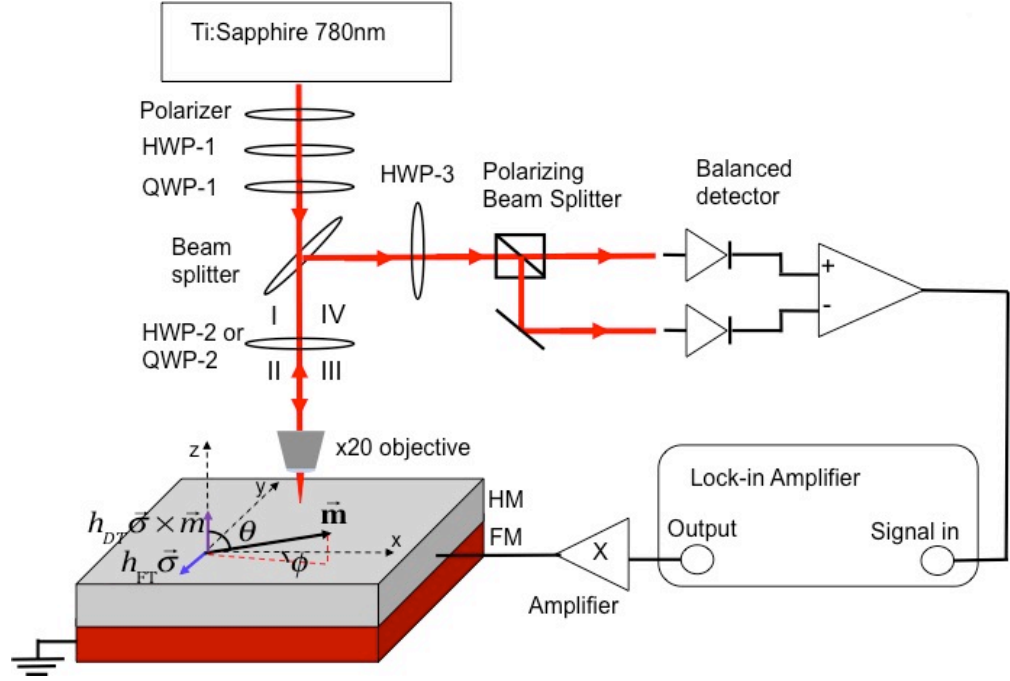


Figure 4.1: Experimental set-up for the optical detection of SOTs. For detecting the current-induced DT, we use a half wave plate, HWP-2, before the sample. This is replaced by a quarter wave plate, QWP-2, for detecting the current-induced FT.

The total polarization rotation before and after the HWP-2 can be derived using the method of Jones calculus, where the polarization is described by a vector while transmission through wave plates and reflection from the magnetic samples are described by a matrix as shown in Table 4.1. We apply an in-plane AC current, $I_{ac} \cos \omega t$, at 1013 Hz with $I_{ac} = 10$ mA and define the x -axis as the direction of current flow, with z perpendicular to the sample plane. We initially align the magnetization along the x direction using an external field H_{ex} .

	Initial Polarization	Half Wave Plate	Quarter Wave Plate	Magnetic sample
Jones Matrices/ Vectors	$P_0 = \begin{bmatrix} 1 \\ 0 \end{bmatrix}$	$M_{HW} = \begin{bmatrix} 1 & 0 \\ 0 & -1 \end{bmatrix}$	$M_{QW} = \begin{bmatrix} 1 & 0 \\ 0 & -i \end{bmatrix}$	$M_K = \xi \begin{bmatrix} 1 + \frac{\beta_{Quadratic}}{2} & -\alpha_{Polar} m_z \\ \alpha_{Polar} m_z & 1 - \frac{\beta_{Quadratic}}{2} \end{bmatrix}$

Table 4.1: List of Jones matrices/vectors used in this calculation. The initial polarization is set along the x -axis. The Jones matrices M in the table for half wave plate, quarter wave plate and magnetic sample are assuming the principle axis (fast axis of the wave plate or in-plane magnetization direction of the magnetic sample) is along the x -axis. The matrices with arbitrary principle axis can be deduced as $R[\theta]MR[-\theta]$, where $R[\theta] = \begin{bmatrix} \cos \theta & -\sin \theta \\ \sin \theta & \cos \theta \end{bmatrix}$ and θ is the relative angle between the principle axis and the x -axis. The factor ξ in the Jones Matrix for the magnetic sample captures the reflection loss, which does not affect the polarization change.

When HWP-2 is used, the light polarization at different points of the set-up marked as I, II, III, IV is calculated as:

I - The polarization is initially aligned in the x direction. $P_1 = \begin{bmatrix} 1 \\ 0 \end{bmatrix}$.

II - Upon transmitting through the HWP-2, the polarization is rotated by an angle $\phi_{pol} = 2\phi_{HW}$, where ϕ_{HW} is the relative angle between the principle axis of the half wave plate and the x direction. $P_2 = R[\phi_{HW}]M_{HW}R[-\phi_{HW}]P_1 = \begin{bmatrix} \cos 2\phi_{HW} \\ \sin 2\phi_{HW} \end{bmatrix}$.

III - After the light is reflected from the magnetic material, the polarization changes to $\phi_{pol} + \Psi_{Kerr}$ due to the polar and quadratic

MOKE:

$$P_3 = R[\varphi] M_K R[-\varphi] P_2 = \xi \left\{ \begin{bmatrix} \cos 2\varphi_{\text{HW}} \\ \sin 2\varphi_{\text{HW}} \end{bmatrix} + \alpha_{\text{Polar}} m_z \begin{bmatrix} -\sin 2\varphi_{\text{HW}} \\ \cos 2\varphi_{\text{HW}} \end{bmatrix} + \frac{\beta_{\text{Quadratic}}}{2} \begin{bmatrix} \cos(2\varphi - 2\varphi_{\text{HW}}) \\ \sin(2\varphi - 2\varphi_{\text{HW}}) \end{bmatrix} \right\}.$$

IV - The polarization of the reflected beam is rotated to $-\Psi_{\text{Kerr}}$ away from initial polarization after passing through the half wave plate HWP-2.

$$P_4 = R[\varphi_{\text{HW}}] M_{\text{HW}} R[-\varphi_{\text{HW}}] P_3 = \xi \left\{ \begin{bmatrix} 1 \\ 0 \end{bmatrix} + \begin{bmatrix} \frac{1}{2} \beta_{\text{Quadratic}} \cos(4\varphi_{\text{HW}} - 2\varphi) \\ -\alpha_{\text{Polar}} m_z + \frac{1}{2} \beta_{\text{Quadratic}} \sin(4\varphi_{\text{HW}} - 2\varphi) \end{bmatrix} \right\}.$$

Therefore the total polarization angle rotation is

$$-\alpha_{\text{Polar}} m_z + \frac{1}{2} \beta_{\text{Quadratic}} \sin(4\varphi_{\text{HW}} - 2\varphi_M). \quad (4.5)$$

Since we study small current-induced rotations of the magnetic moment about an initial state with $\varphi = 0, \theta = \pi/2$ by differentiating Eq. (4.5) and substituting $\varphi_{\text{HW}} = \phi_{\text{pol}}/2$, we can derive

$$-\Delta\Psi = -\alpha_{\text{Polar}} \Delta\theta + \beta_{\text{Quadratic}} \cos 2\phi_{\text{pol}} \Delta\phi. \quad (4.6)$$

For $\phi_{\text{pol}} = 45^\circ$ the contribution from the quadratic MOKE vanishes. The principle axis of the analyzing wave plate HWP-3 is set to be 22.5° from the x -axis. As a result, after passing through HWP-3, the light can be described by

$$R\left[\frac{\pi}{8}\right] M_{\text{HW}} R\left[-\frac{\pi}{8}\right] \xi \begin{bmatrix} 1 + \frac{1}{2} \beta_{\text{Quadratic}} \cos(4\varphi_{\text{HW}} - 2\varphi_M) \\ -\alpha_{\text{Polar}} \cos\theta_M + \frac{1}{2} \beta_{\text{Quadratic}} \sin(4\varphi_{\text{HW}} - 2\varphi_M) \end{bmatrix} = \frac{\xi}{\sqrt{2}} \begin{bmatrix} 1 + \frac{1}{2} \beta_{\text{Quadratic}} \cos(4\varphi_{\text{HW}} - 2\varphi_M) - \alpha_{\text{Polar}} \cos\theta_M + \frac{1}{2} \beta_{\text{Quadratic}} \sin(4\varphi_{\text{HW}} - 2\varphi_M) \\ 1 + \frac{1}{2} \beta_{\text{Quadratic}} \cos(4\varphi_{\text{HW}} - 2\varphi_M) + \alpha_{\text{Polar}} \cos\theta_M - \frac{1}{2} \beta_{\text{Quadratic}} \sin(4\varphi_{\text{HW}} - 2\varphi_M) \end{bmatrix} = \begin{bmatrix} E_{x'} \\ E_{y'} \end{bmatrix}.$$

The changes in the Kerr rotation angle are measured by using a polarizing beam splitter to separate the s - and p -components of the light and then analyzing the power

difference by a balanced detector. A lock-in amplifier locked to the frequency of the applied current records current-induced changes in the Kerr rotation. The voltage output from the balanced detector is proportional to

$$\begin{aligned} & |E_{x'}|^2 - |E_{y'}|^2 \\ &= \xi^2 \left[1 + \frac{1}{2} \beta_{\text{Quadratic}} \cos(4\varphi_{\text{HW}} - 2\varphi_{\text{M}}) \right] \times \left[-\alpha_{\text{Polar}} \cos\theta_{\text{M}} + \frac{1}{2} \beta_{\text{Quadratic}} \sin(4\varphi_{\text{HW}} - 2\varphi_{\text{M}}) \right]. \end{aligned} \quad (4.7)$$

By differentiating Eq. (4.7), we determine the AC voltage output from the balanced detector to be $V_{\text{Lock-in}} = \xi^2 \Delta\Psi$. On the other hand, when one of the inputs of the balanced detector is blocked, the DC component of the voltage output is $V_{\text{DC}} = \xi^2 / 2$. Therefore, the current-induced polarization rotation is extracted as $\Delta\Psi = \frac{V_{\text{Lock-in}}}{2V_{\text{DC}}}$.

To measure the FT, we substitute the HWP-2 with a QWP-2 with its principle axis set at 45° from the x -axis to generate circularly polarized light incident upon the bilayer. The light polarization at different points of the set-up marked as *I, II, III, IV* is calculated as:

I - The polarization is initially aligned in the x direction. $P_1 = \begin{bmatrix} 1 \\ 0 \end{bmatrix}$.

II - After the quarter wave plate QWP-2, the polarization becomes circularly polarized. $P_2 = R[\pi/4] M_{\text{QWP}} R[-\pi/4] P_1 = \frac{1-i}{2} \begin{bmatrix} 1 \\ i \end{bmatrix}$.

III - Upon reflection from the magnetic material, the magnetization becomes elliptically polarized, due to the quadratic MOKE.

$$P_3 = R[\varphi] M_{\text{K}} R[-\varphi] P_2 = \frac{1-i}{2} \xi \left\{ (1 - i\alpha_{\text{Polar}} m_z) \begin{bmatrix} 1 \\ i \end{bmatrix} + \frac{\beta_{\text{Quadratic}} (\cos\varphi + i\sin\varphi)^2}{2} \begin{bmatrix} 1 \\ -i \end{bmatrix} \right\}.$$

IV - After passing through QWP-2 again, the polarization is rotated to the y direction with a perturbation due to the quadratic MOKE.

$$P_4 = R[\pi/4]M_{\text{QW}}R[-\pi/4]P_3 = \xi \left\{ \begin{bmatrix} 0 \\ 1 \end{bmatrix} + \begin{bmatrix} \beta_{\text{Quadratic}} \frac{\sin 2\phi - i \cos 2\phi}{2} \\ i\alpha_{\text{Polar}} m_z \end{bmatrix} \right\}.$$

Therefore the total polarization angle rotation is

$$\frac{\pi}{2} - \beta_{\text{Quadratic}} \frac{\sin 2\phi - i \cos 2\phi}{2}. \quad (4.8)$$

By differentiating this polarization rotation near $\phi_M = 0$, we can derive

$$\Delta\Psi = -\beta_{\text{Quadratic}} \Delta\phi. \quad (4.9)$$

Out-of-plane magnetization does not give rise to polarization change to the circularly polarized light. Therefore, only the quadratic MOKE effect should contribute a signal in this geometry, with no contribution from the polar MOKE. Following the same process, it can be derived that the current-induced polarization rotation for light with circular polarization incident on the bilayer follows $\Delta\Psi = -\frac{V_{\text{Lock-in}}}{2V_{\text{DC}}}$.

4.4 Experimental Results of DT and FT with Polar and Quadratic MOKE

For a sample with the layer structure wafer/Pt(6 nm)/Py(8 nm)/ AlO_x the current-induced Kerr response as a function of swept magnetic field for different values of ϕ_{pol} is shown in Figure 4.2. By Eq. (4.6), we expect the contribution from the quadratic MOKE to be zero. We observe a simple step-like change in the current-induced Kerr signal near $H_{\text{ex}} = 0$, with the signal approximately independent of H_{ex} on either side of the step. This is the behavior expected from the polar Kerr signal by itself, with the step near $H_{\text{ex}} = 0$ due to reversal of the magnetization and with the weak magnetic-field dependence away from the step consistent with Eq. (4.4) for $H_{\text{ex}} \ll M_s$. As the polarization angle is rotated so that ϕ_{pol} differs from 45°, the form of the magnetic-field dependence of the current-induced Kerr signal changes dramatically, evolving from a simple step to the superposition of a step with an

additional component that is approximately inversely proportional to H_{ex} . This is the signature of a significant quadratic MOKE signal in addition to the polar MOKE, with the current-induced magnetization rotation within the sample plane providing the $1/H_{ex}$ dependence according to Eq. (4.4).

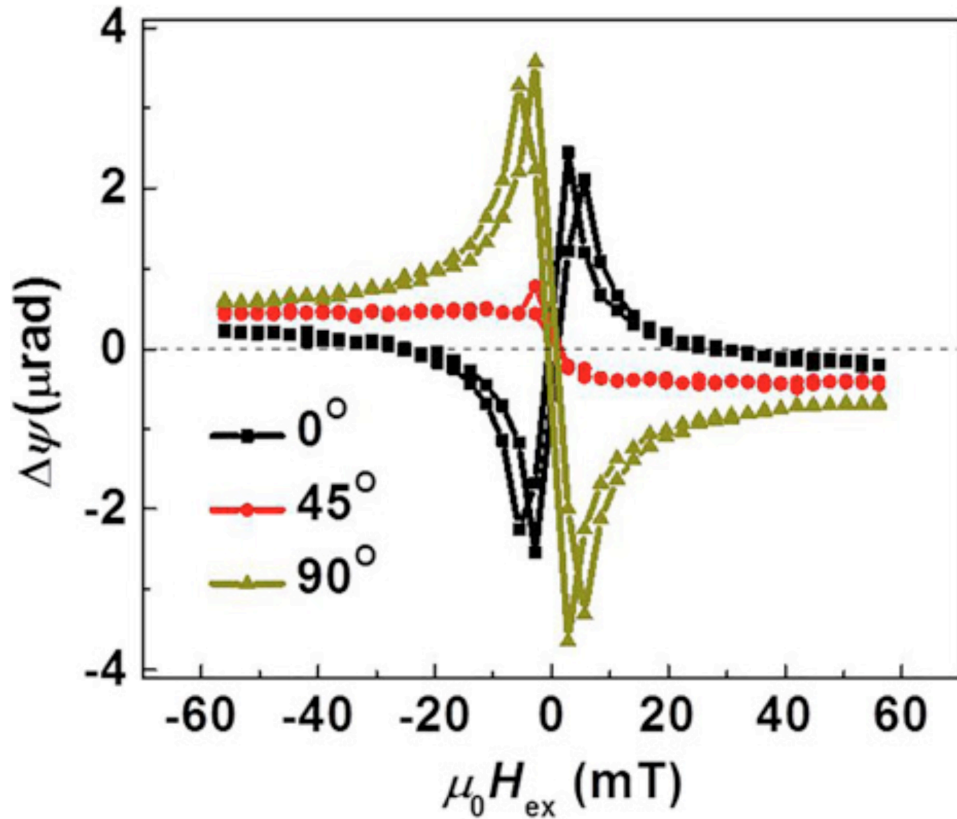


Figure 4.2: Current-induced polar MOKE response with three different incident laser polarizations.

The current-induced torque in a Pt/Py bilayer contains contributions from both the Oersted field (with both an approximately uniform in-plane component together with out-of-plane components near the edges of the sample) and SOTs. The out-of-plane components due to the Oersted field and DT can be distinguished based on

different symmetries with respect to reversing the magnetization; the Oersted field will not change upon magnetization reversal while the DT should invert, as we have shown in Chapter 3. For DT component isolation, we have employed the same self-calibration method described in Chapter 3. To isolate the out-of-plane Oersted field, we therefore plot the symmetric combination of polar Kerr signals, $\Delta\Psi(+m_x) + \Delta\Psi(-m_x)$, and to isolate the DT, we plot the antisymmetric combination, $\Delta\Psi(+m_x) - \Delta\Psi(-m_x)$ as seen in Figure 4.3, which is measured with linearly polarized light at $\phi_{pol} = 45^\circ$. As expected, we find that the out-of-plane Oersted field is antisymmetric about the center of the wire, and the DT is approximately constant across the wire width. Comparison of the measured out-of-plane Oersted field with a finite-element calculation of the Oersted field in a thin-film sample of finite width allows an accurate calibration of the DT field measured by the polar Kerr response.

The polar MOKE coefficient α_{polar} is extracted from the polar MOKE data shown in Figure 4.3. The line scan $\Delta\Psi(+m_x) + \Delta\Psi(-m_x)$ is due to the out-of-plane Oersted field, $h_{Oe,out}$, such that $\Delta\Psi(+m_x) + \Delta\Psi(-m_x) = \frac{2\alpha_{polar} \langle h_{Oe,out} \rangle}{H_{ext} + H_{anis} + M_S - H_{anis\perp}}$, where $\langle h_{z,Oe} \rangle$ is the average field in the region illuminated by the laser. The out-of-plane Oersted field can be calculated following Ampere's Law, $h_{Oe,out} = \frac{I}{2\pi w} \ln \frac{y'}{w - y'}$,

where w is the width of the strip. Through fitting the data as shown in Figure 4.3, we can extract α_{polar} to be $(5.8 \pm 0.8) \times 10^{-3}$ based on which we extract a value for the out-of-plane spin-orbit equivalent field of $\mu_0 h_{DT} = 0.068 \pm 0.010$ mT at a 10 mA current bias through the $50 \mu m$ strip. Using a simple parallel circuit model to account for the different resistivities of Pt and Py, we estimate that approximately 42% of the current flows through Pt, yielding a current density in the Pt of $j_{Pt} = 1.4 \times 10^{10}$ A/m². If we

assume all of the DT is due to the SHE in the Pt layer, we determine a spin Hall angle $\theta_{Pt} = 0.082 \pm 0.012$.

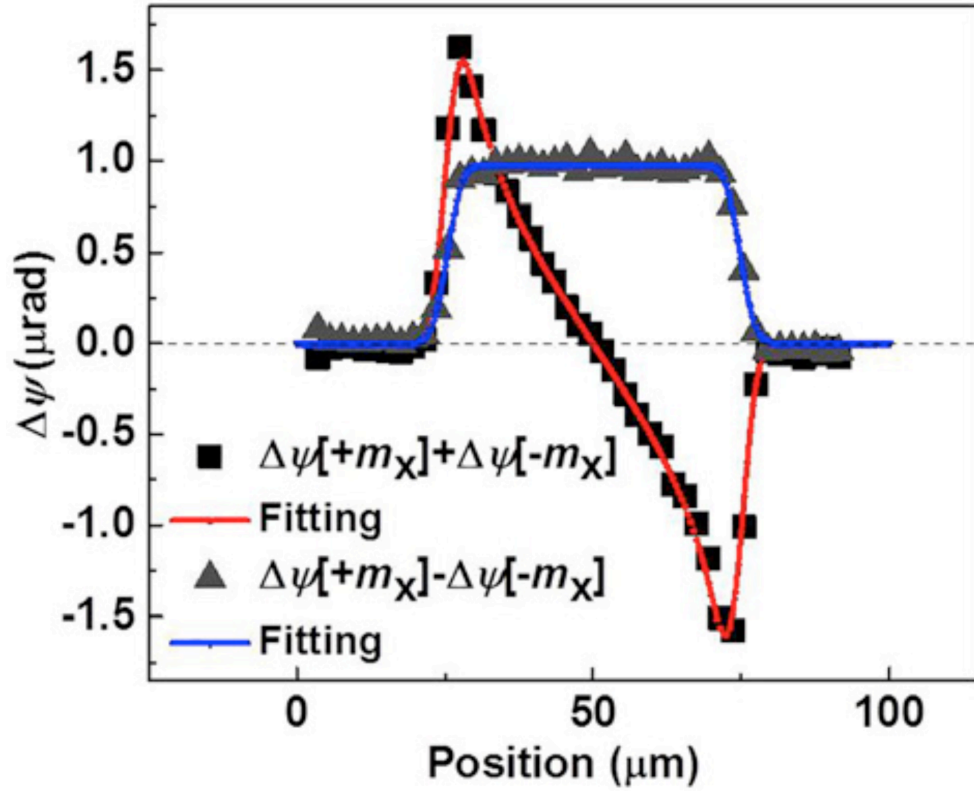


Figure 4.3: Separation of the out-of-plane field due to the Oersted field and the DT by the spatial symmetry and dependence on the magnetization orientation.

Figure 4.4 shows the Kerr signal as a function of swept applied field, H_{ex} , at 0° and circular polarizations. When circularly polarized light is incident, the step-like component seen in the polar MOKE signal vanishes, leaving only a signal proportional to $1/H_{ex}$ away from $H_{ex} = 0$ which is consistent with the expectation that only $\Delta\phi$ contributes to the quadratic MOKE signal.

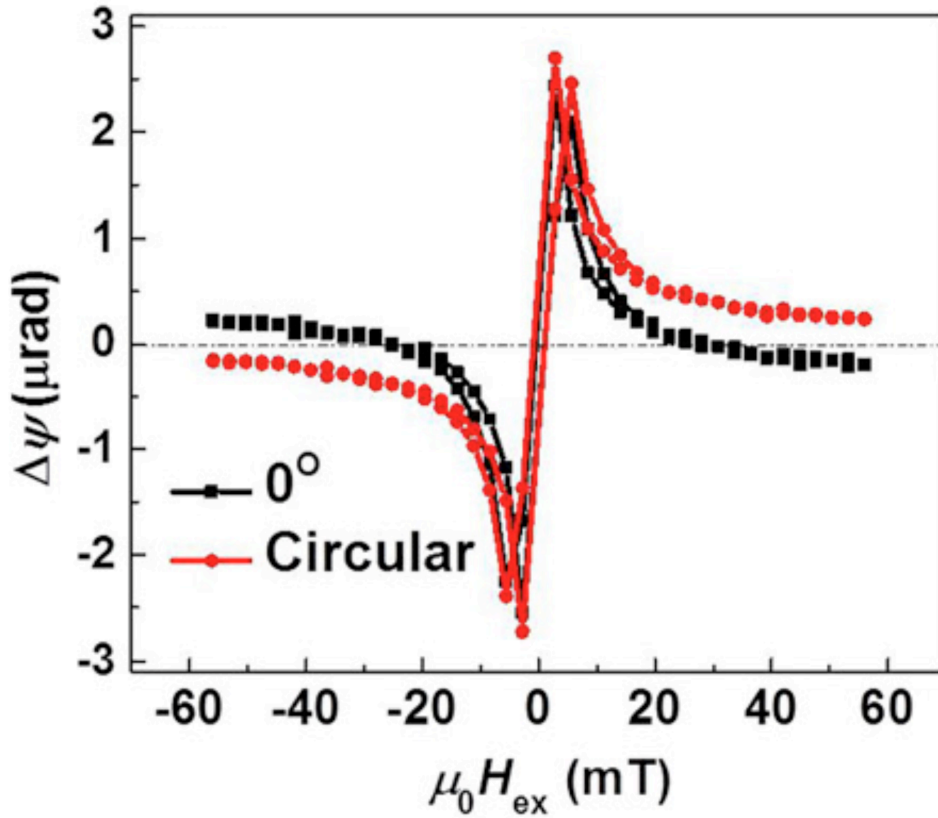


Figure 4.4: Current-induced Kerr response with circularly polarized light and 0° linearly polarized light. The former only contains a quadratic MOKE response ($1/H_{ex}$ -like) while the latter is a superposition of a quadratic MOKE response and a polar MOKE response (which has a step-like dependence on H_{ex}).

We can calibrate the effective in-plane field produced by the current in the bilayer in the same way we do the calibration for longitudinal measurements in Chapter 3. Calibration can be done using a metal strip fabricated on a printed circuit board attached to the back of the sample to apply a known oscillating in-plane external magnetic field and measuring the quadratic MOKE signal due to this external field. The MOKE signal measured with the calibration field $h_{Cal} = 0.08 \pm 0.008$ mT applied

along the y direction is used to extract $\beta_{\text{Quadratic}}$. In this case, the magnetization will reorient in the x - y plane, $\Delta\varphi = \frac{h_{\text{Cal}}}{H_{\text{ex}} + H_{\text{anis}}}$, following Eq. (4.4). Hence the measured

MOKE response can be deduced from Eq. (4.5) as $\Delta\Psi_{\text{Cal}} = \beta_{\text{Quadratic}} \frac{h_{\text{Cal}}}{H_{\text{ex}} + H_{\text{anis}}}$. Using

this expression, we fit the quadratic MOKE response measured under the calibration field, shown in Figure 4.6, and obtain $\beta_{\text{Quadratic}} = (1.1 \pm 0.1) \times 10^{-4}$. For the

Pt(6nm)/Py(8nm) sample with 10mA current bias, the equivalent field in-plane field produced by the current in the bilayer is $h_{\text{FT}} = 0.10 \pm 0.01$ mT. The uncertainty here arises mainly from inaccuracies in knowing the magnitude of the calibration field at the sample.

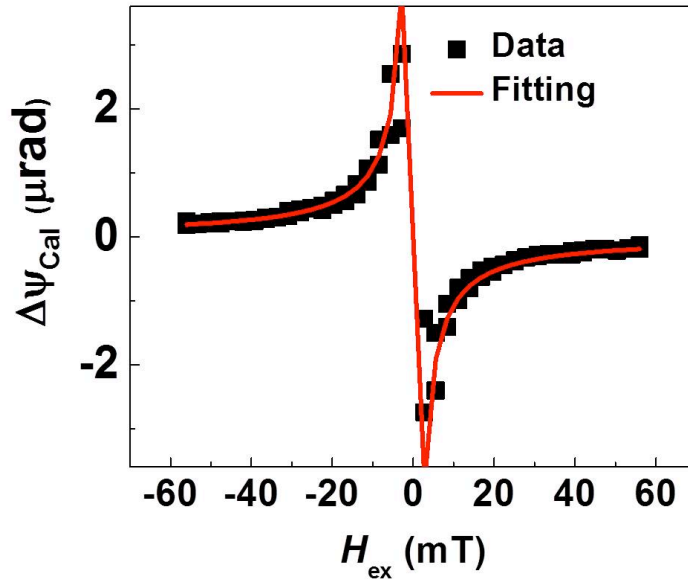


Figure 4.5: MOKE data when the calibration field is applied. The red curve is the fit

using $\Delta\Psi = \beta_{\text{Quadratic}} \frac{h_{\text{Cal}}}{H_{\text{ex}} + H_{\text{anis}}}$.

4.4.1 Laser Polarization Angle Dependence of MOKE

We have performed a laser-polarization-angle-dependent MOKE study to verify the angular dependence of the Kerr coefficients assumed in Eq. (4.6). Within linear response, the current-induced Kerr rotation in general should be described as

$$\Delta\Psi = a(\phi_{\text{pol}})\Delta\theta + b(\phi_{\text{pol}})\Delta\phi \quad (4.10)$$

where $a(\phi_{\text{pol}})$ and $b(\phi_{\text{pol}})$ are the MOKE coefficients that may depend on the polarization angle while $\Delta\theta$ and $\Delta\phi$ are the current-induced polar and azimuthal angle changes, which are independent of the polarization. Using Eq. (4.4) and the fields h_{DT} and h_{FT} derived in Section 1.4 when passing 10 mA current through the 50 μm sample strip, we extract $\Delta\theta = 77 \pm 11 \mu\text{rad}$ and $\Delta\phi = (1.1 \pm 0.1) \times 10^{-4} \frac{0.1 \text{ mT}}{\mu_0 H_{\text{ex}}}$.

Therefore, $a(\phi_{\text{pol}})$ and $b(\phi_{\text{pol}})$ can be extracted from the MOKE data measured at different polarizations, like shown in Figure 4.2, through linear regression. The extracted data, shown in Figure 4.6, reveals that indeed $a(\phi_{\text{pol}})$ is nearly independent with polarization and $b(\phi_{\text{pol}})$ has a cosine dependence on the polarization, which confirms Eq. (4.6).

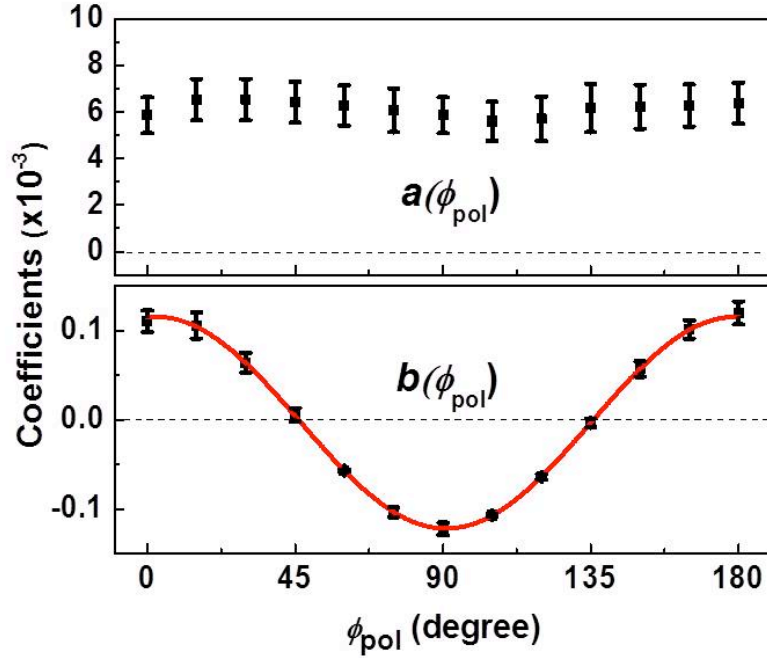


Figure 4.6: MOKE coefficients plotted as a function of laser polarization. The red curve in the bottom panel is a sinusoidal fit to $\cos 2\phi_{\text{pol}}$.

It is worth mentioning that the magnitude of α_{polar} is almost two orders of magnitude greater than $\beta_{\text{Quadratic}}$, which is perhaps not surprising given that the polar MOKE is a first-order process and the quadratic MOKE is second-order. Nevertheless, because the out-of-plane magnetization reorientation $\Delta\theta$ is strongly suppressed by the demagnetization effect, the measured quadratic MOKE signal can still exceed the polar MOKE response in our thin-film bilayer samples.

4.5 Experimental Detection of DT and FT with ST-FMR

ST-FMR measurement can be used to determine the DT and FT in FM/HM bilayers. ST-FMR is performed by following the procedures described in Ref. [9]: a microwave current is applied to the sample through a coplanar waveguide structure to

excite the magnetic precession and a magnetic resonance signal is detected via a rectified DC voltage. The magnitude of the symmetric part of the resonance allows a determination of the DT, and the anti-symmetric part yields the FT. The microwave current flowing through the sample is calibrated from a microwave reflection measurement.

4.6 Comparison of Experimental Data on DT and FT by MOKE and ST-FMR

To further verify the accuracy of our MOKE-based spin-torque magnetometer, we measured samples with varying Py thickness: wafer/Pt(6 nm)/Py(d_{Py})/AlO_x, with $d_{Py} = 2\text{--}10$ nm, and compared the results to ST-FMR performed on the same samples. We plot in Figure 4.7 the measured h_{DT} and h_{FT} determined by both MOKE and ST-FMR as a function of d_{Py} . These measured fields are normalized by the total surface current density (I_{tot}/w), where w is the width of the sample. The two measurement techniques are in excellent quantitative agreement for both components. The strengths of both components of the equivalent field decrease as a function of increasing d_{Py} in part because this corresponds to a decrease in the current density flowing in the Pt layer; however, the dependences on d_{Py} are different for the two components. This is as expected due to the physical differences between the antidamping spin Hall torque that acts at the interface of the magnetic layer and the in-plane Oersted field that acts throughout the thickness of the magnetic layer.

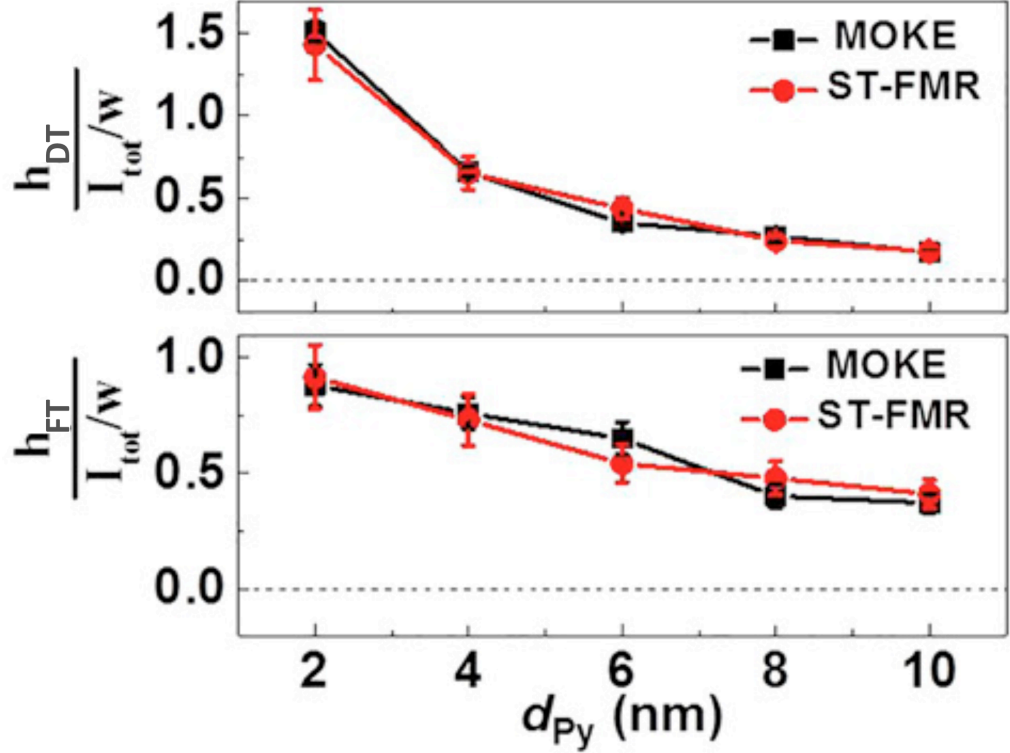


Figure 4.7: (a) The equivalent current-generated fields corresponding to the damping-like component h_{DT} and the in-plane effective-field-like component h_{FT} normalized by the total current per unit lateral width in the bilayer. The uncertainties for the MOKE technique mostly arise from the fitting, while the uncertainties for the ST-FMR are mainly due to the determination of the microwave current. Excellent agreement is found between the MOKE and ST-FMR techniques.

In Figure 4.8, we take the measurements of the DT from Figure 4.7 and replot them in the form of a surface torque per unit area ($\tau_{AD,SO} / A = h_{DT} \mu_0 \gamma M_s d_{Py}$) normalized by the current density flowing just in the Pt layer, estimated from a simple parallel circuit model taking into account the different average resistivities of the Pt and Py layers. Over most of the range of Py thickness, the torque is independent of

d_{Py} , as expected for the surface torque due to the SHE arising from the Pt layer. The corresponding average spin Hall angle is 0.075 ± 0.010 . There may be a small decrease in the strength of the torque for the 2 nm Pt layer, which is interesting in that it could hint at a decreased efficiency in the absorption of the incoming spin current for a very thin Py layer.

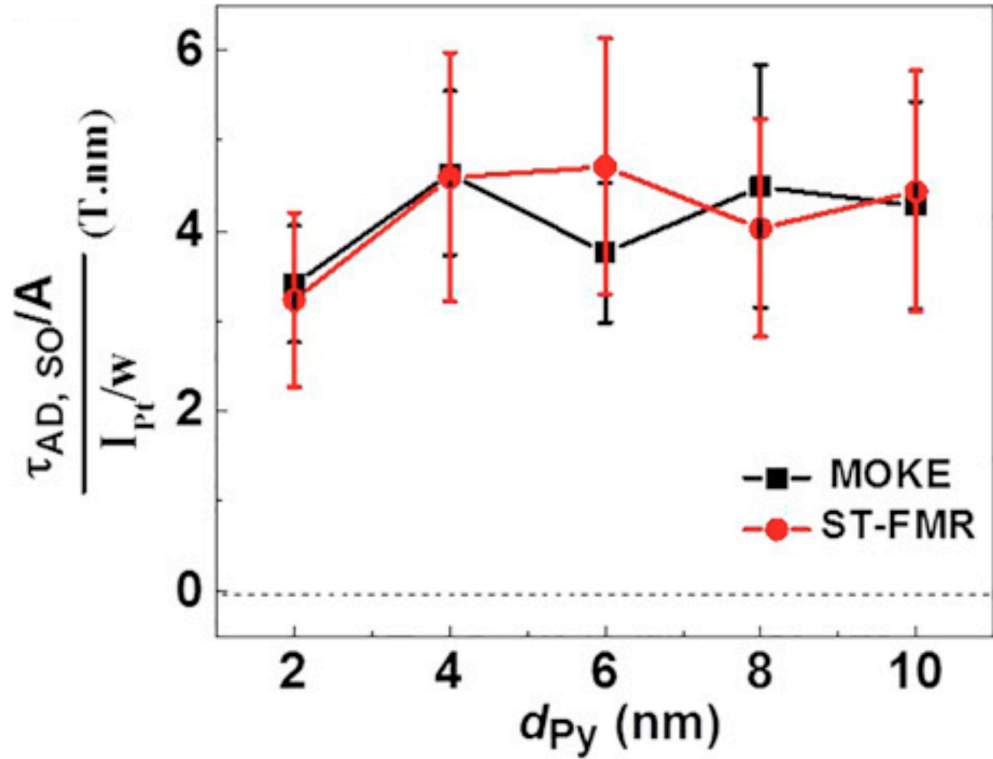


Figure 4.8: $\tau_{AD,SO} / A$ normalized by the estimated current per unit sample width in the Pt layer.

In Figure 4.9, we replot the data for the h_{FT} taken from Figure 4.7, but the normalized versus the estimated current per unit lateral sample width flowing just in the Pt layer rather than the total current. For a pure Oersted field, the value should be

0.5, independent of Py thickness. We find that the measured equivalent field is indeed independent of d_{Py} , but the magnitude is somewhat larger than expected from a pure Oersted field. This discrepancy could be due to an inaccuracy in our simple parallel circuit model for estimating the current in the Pt (we neglect surface scattering, for example) or to the existence of a spin-orbit-induced effective field with an unexpected dependence on d_{Py} .

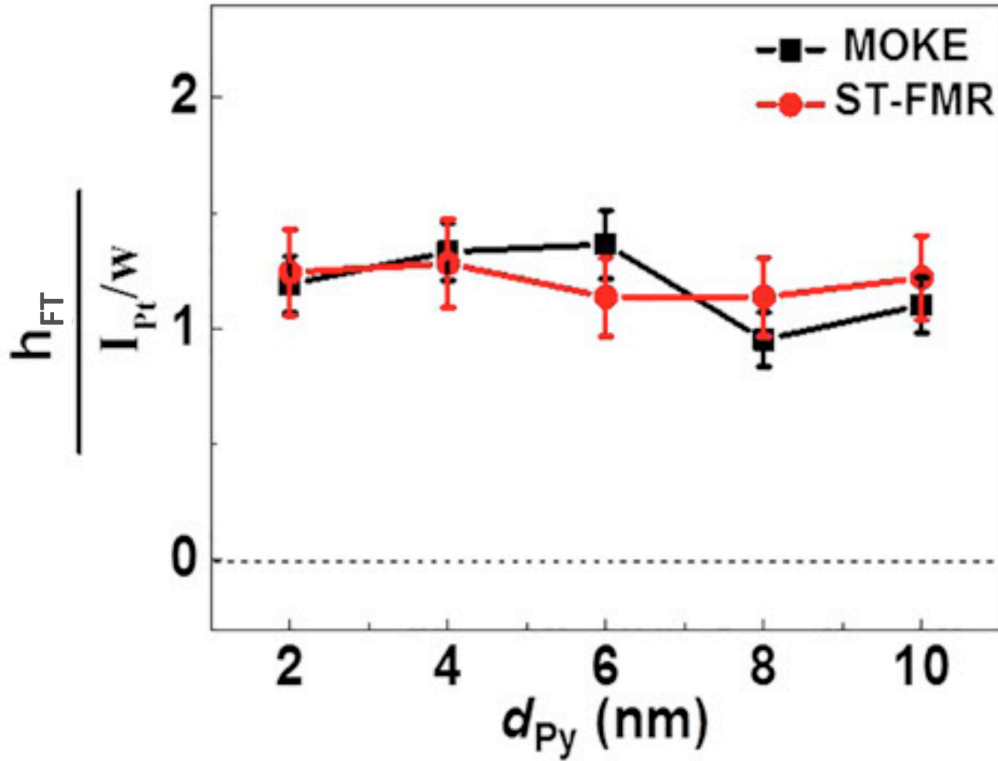


Figure 4.9: The h_{FT} normalized by the estimated current per unit sample width in the Pt layer.

4.7 Summary

We have demonstrated a convenient all-optical MOKE technique that can separately measure the DT and FT components of the current-induced SOT via polar

MOKE and quadratic MOKE, respectively, with both measurements performed using normally incident light. We find excellent agreement between the results of this technique and ST-FMR measurements for a series of Pt/Py bilayers with different Py thicknesses. We anticipate that MOKE magnetometry will be useful for rapid characterization of current-induced torques acting on a very wide range of materials.

REFERENCES

- [1] Y. K. Kato, R. C. Myers, A. C. Gossard, and D. D. Awschalom, *Science* (80-.). **306**, 1910 (2004).
- [2] G.-M. Choi and D. G. Cahill, *Phys. Rev. B* **90**, 214432 (2014).
- [3] Z. Q. Qiu and S. D. Bader, *Rev. Sci. Instrum.* **71**, 1243 (2000).
- [4] M. Montazeri, P. Upadhyaya, M. C. Onbasli, G. Yu, K. L. Wong, M. Lang, Y. Fan, X. Li, P. Khalili Amiri, R. N. Schwartz, C. A. Ross, and K. L. Wang, *Nat. Commun.* **6**, 8958 (2015).
- [5] J. Hamrlová, J. Hamrle, K. Postava, and J. Pištora, *Phys. Status Solidi Basic Res.* **250**, 2194 (2013).
- [6] C. Dehesa-Martínez, L. Blanco-Gutierrez, M. Vélez, J. Díaz, L. M. Alvarez-Prado, and J. M. Alameda, *Phys. Rev. B* **64**, 24417 (2001).
- [7] M. Buchmeier, R. Schreiber, D. E. Bürgler, and C. M. Schneider, *Phys. Rev. B* **79**, 64402 (2009).
- [8] R. . Osgood III, S. . Bader, B. . Clemens, R. . White, and H. Matsuyama, *J. Magn. Magn. Mater.* **182**, 297 (1998).
- [9] A. R. Mellnik, J. S. Lee, A. Richardella, J. L. Grab, P. J. Mintun, M. H. Fischer, A. Vaezi, A. Manchon, E.-A. Kim, N. Samarth, and D. C. Ralph, *Nature* **511**, 449 (2014).

Chapter 5

QUANTIFYING THE ANGULAR DEPENDENCE OF SPIN-ORBIT TORQUES IN HM/FM/METAL-OXIDE TRILAYERS WITH PERPENDICULAR MAGNETIC ANISOTROPY

In this chapter, we develop a scheme to quantify the angular dependence of spin-orbit torques (SOTs) based on the polar MOKE with field calibration. Theoretical calculations predict no dependence of the SOTs on the out-of-plane angle of magnetization due to SHE, but the Rashba effect induces a nontrivial angular dependence of the SOTs. Quantitative measurements with adiabatic harmonic Hall technique have observed the angular dependence in Ta/CoFeB/MgO or Pt/Co/AIO_x with perpendicular magnetic anisotropy. However, this method is complicated because the signal consists of both anomalous and planar Hall contributions. In addition, the fitting of the measurement data is sensitive to the fitting parameters, particularly to the perpendicular anisotropy, in a certain angle region (40–70°). To avoid this uncertainty, we precisely determine the SOTs and their angle dependence on the magnetization orientation via polar MOKE measurements. We observe a strong angular dependence that is different from the previous experimental observations. Based on this strong dependence, we conclude that a Rashba effect at the same interface, that is responsible for the perpendicular magnetic anisotropy, is the dominant mechanism for the current-driven SOTs in this system.

5.1 Introduction

In-plane current in HM/FM/ metal-oxide (MO_x) trilayers generates SOTs that enable an efficient method to control the magnetization of FM layer. Although it has been pointed out that the damping-like torque (DT) and field-like torque (FT) are dominated by the SHE and the Rashba effect, respectively [1–3], each torque contains the contributions from both the SHE and the Rashba effect [4–7]. The SOTs in HM/FM bilayers with in-plane magnetic anisotropy have been extensively investigated. The DT is usually found to be larger than the FT [8–10], indicating the SHE is strong in the bilayers with in-plane anisotropy. We have identified the contributions of the SHE and the Rashba effect to SOTs in Pt/CoFeB bilayers by inserting a copper layer to minimize the Rashba effect in Chapter 3. However, the same scheme cannot be applied to Ta/CoFeB/MgO trilayers with perpendicular magnetic anisotropy (PMA) since it will dramatically affect the PMA [11–15]. Different from the in-plane bilayers, the Ta/CoFeB/MgO trilayers with PMA show a strong Rashba effect, owing to the interfacial symmetry-breaking and hybridization of electronic states at the Ta/CoFeB and CoFeB/MgO interfaces [16,17]. The ratio between FT and DT are detected to be 2 [16], 3 [17], 6 [18,19], and up to 8 (this study), which is significantly affected by the modification of the interfaces through thermal annealing [20]. The Rashba-induced SOTs are closely related to the PMA [20], while the mechanism needs further theoretical investigation.

One promising method to distinguish between SHE- and Rashba-driven SOTs is through the dependence of SOTs on the angular direction of the magnetization. Theories based on the bulk SHE combined with the Boltzmann transport equation [5] suggest both FT and DT are independent on the rotation of magnetization normal to the film plane. On the other hand, a model with the Rashba spin-orbit coupling with

comparable strength to the exchange coupling [21] predicts a strong angular dependence in the SOTs. The angular dependence of SOTs has a critical impact on the magnetization dynamics and hence is important to understand for optimizing spin-orbit spintronics devices.

In this chapter, we determine the angular dependence of SOTs in Ta (2 nm)/CoFeB (1 nm)/MgO (3 nm) trilayers with adiabatic harmonic Hall and polar MOKE. We show that the harmonic Hall technique employed in the previous studies [16–18] is inaccurate in determining the angular dependence of SOTs, particularly in the medium polar angle region ($\theta = 40 - 70^\circ$), because the fitting of the measurement curves is very sensitive to the fitting parameters like perpendicular anisotropy. In MOKE measurements, we implement a field-calibration method to accurately quantify the SOTs at various polar angles of magnetization. The obtained nontrivial angular dependence of the SOTs is distinct from the previous experimental observations. The results suggest that the Rashba effect is the dominant contribution to SOTs in Ta/CoFeB/MgO structures.

5.2 Sample Fabrication and the Optimization of PMA in Ta/CoFeB/MgO Trilayers

The trilayer samples composed of Ta/ Co₄₀Fe₄₀B₂₀/ MgO were grown on a thermally oxidized Si wafer by magnetron sputtering. The base pressure of the vacuum chamber is 3×10^{-8} Torr, and the H₂O partial pressure is 3×10^{-9} Torr. Ta and CoFeB layers were deposited by dc sputtering at a rate of 1 Å/s. MgO was deposited from a MgO target by RF sputtering at a rate of 0.04 Å/s. The argon pressures during the deposition were 3 mTorr for Ta and CoFeB deposition and 1.1 mTorr during MgO deposition. Then a 7-nm SiO₂ was grown as the capping layer to protect the MgO

layer from degradation during the following annealing and fabrication process. For the harmonic Hall voltage measurements, the thin films were lithographically patterned into Hall bars 500 μm wide and 3 mm long. The samples used for MOKE measurements were patterned into 30 μm \times 30 μm squares. The contact pads consist of Ta (5)/Cu (200)/Au (50).

The interfacial PMA in Ta/CoFeB/MgO trilayers arises from the hybridization between the ferromagnetic atoms (Co and Fe) and the oxygen atoms in MgO [15]. A more recent study suggests that bottom metallic layers like Ta also significantly influence the perpendicular anisotropy [22]. Moreover, the annealing treatments are necessary for the development of PMA and tunneling magnetoresistance in the perpendicular magnetic tunnel junction. With the rapid thermal annealing technique Wang *et al.* [14] have achieved over 100% TMR. Here, we adopt a similar thermal treatment at 340°C for 3 min.

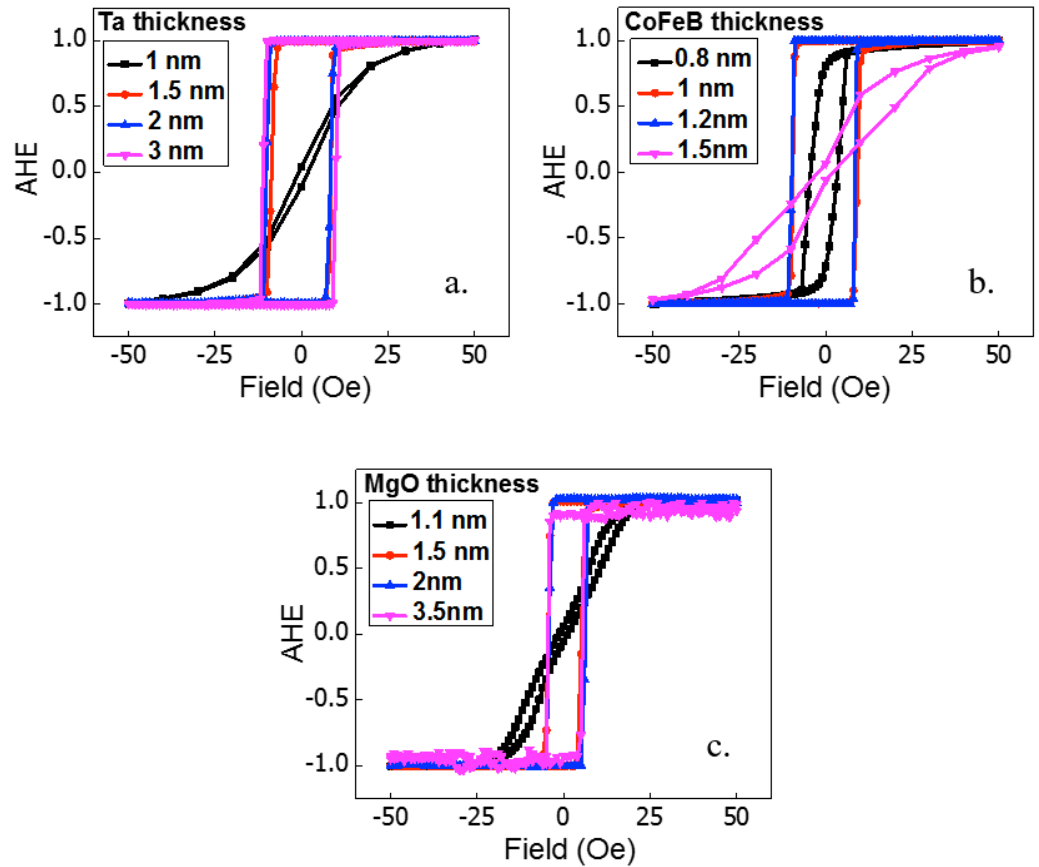


Figure 5.1: The anomalous Hall effect hysteresis loops of three groups of samples: (a) Ta (x)/CoFeB (1.2)/MgO (3), (b) Ta (2)/CoFeB (y)/MgO (3), and (c) Ta (2)/CoFeB (1.2)/ MgO (z).

We investigate the influence of the thickness of an individual layer on the development of PMA. Three sets of samples were fabricated. Each set of samples has the same structure, but with thickness variation in one of the three layers. The structures are Ta (x)/CoFeB (1.2)/MgO (3), Ta (2)/CoFeB (y)/MgO (3), and Ta (2)/CoFeB (1.2)/ MgO (z). The PMA of each sample is investigated via anomalous Hall effect measurements (AHE), where the Hall voltage is detected as the magnetic field is swept in the direction normal to the film plane. As shown in Figure 5.1, the

square-shaped hysteresis loop indicates good PMA. Summarizing all results, we obtain the required thickness ranges for PMA, which are $t_{\text{Ta}} > 1 \text{ nm}$, $1.5 \text{ nm} > t_{\text{CoFeB}} > 0.8 \text{ nm}$, and $t_{\text{MgO}} > 1.1 \text{ nm}$. We, therefore, choose the structure of Ta (2)/ CoFeB (1)/ MgO (3) to measure SOTs.

5.3 Magnetization Reorientation due to the SOTs in Multilayer Thin Films with PMA

The SOTs rotate the magnetization from its equilibrium orientation. As shown in Figure 5.2, θ_0 and ϕ_0 are the polar and azimuthal angle of the magnetization in the FM layer in the equilibrium direction. We also define the polar and azimuthal angle of the magnetic field as θ_H and ϕ_H . The in-plane current generates effective fields $\Delta H_{x,y,z}$ of SOTs, leading to modulation of the magnetization angle ($\Delta\theta$ and $\Delta\phi$). To determine the current-induced SOTs, we derive the relation between the SOTs and the change of magnetization angle.

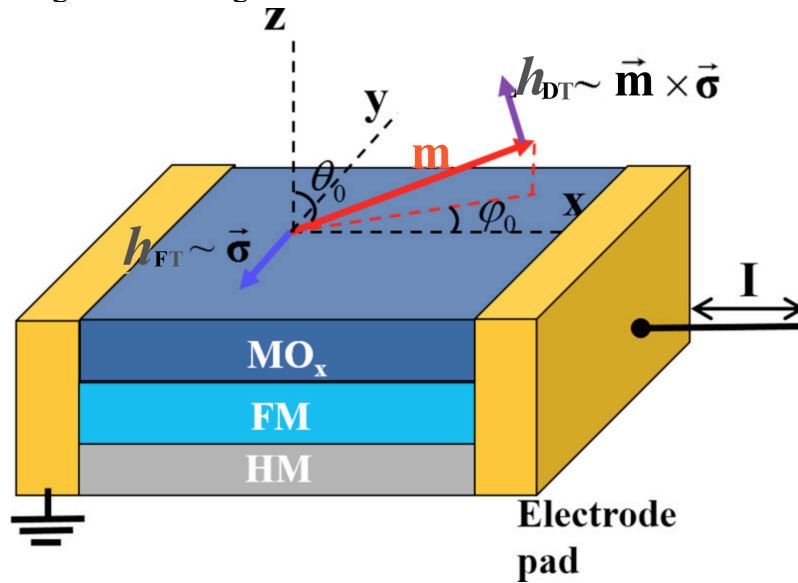


Figure 5.2: The sample structure of a trilayer system with PMA and the current induced DT and FT.

The magnetic energy of the system can be written as

$$E = -K_p \cos^2 \theta - K_l \sin^2 \phi \sin^2 \theta - \vec{M} \cdot \vec{H} , \quad (5.1)$$

where K_p is the effective out-of-plane anisotropy energy, including demagnetizing energy and perpendicular surface anisotropy K_\perp , and K_l is the in-plane uniaxial anisotropy energy. In a magnetic thin film, K_p can be expressed as $K_p = K_\perp - \frac{1}{2} M_s^2$.

The corresponding effective out-of-plane and in-plane anisotropy fields can be written as $H_p = \frac{2K_p}{M_s}$ and $H_l = \frac{2K_l}{M_s}$. To find the equilibrium magnetization directions

(θ_0, ϕ_0) , one can solve the equations

$$\left. \frac{\partial E}{\partial \theta} \right|_{\theta=\theta_0, \phi=\phi_0} = 0 , \quad (5.2)$$

$$\left. \frac{\partial E}{\partial \phi} \right|_{\theta=\theta_0, \phi=\phi_0} = 0. \quad (5.3)$$

The small perturbations ($\Delta\theta$ and $\Delta\phi$) to the magnetization direction are given by

$$\Delta\theta = \frac{\partial \theta}{\partial H_x} \Delta H_x + \frac{\partial \theta}{\partial H_y} \Delta H_y + \frac{\partial \theta}{\partial H_z} \Delta H_z , \quad (5.4)$$

$$\Delta\phi = \frac{\partial \phi}{\partial H_x} \Delta H_x + \frac{\partial \phi}{\partial H_y} \Delta H_y + \frac{\partial \phi}{\partial H_z} \Delta H_z . \quad (5.5)$$

We assume that the external magnetic field is much larger than the in-plane uniaxial anisotropy, so that $\phi_0 = \phi_H$. We further assume the direction of the external magnetic

field is along either the x or y -axis. Eqs. (5.4) and (5.5) under small angle

approximation can be expressed as [23]

$$\Delta\theta = \frac{\cos\theta_0 (\Delta H_x \cos\phi_H + \Delta H_y \sin\phi_H) - \sin\theta_0 \Delta H_z}{(H_p - H_l \sin^2 \phi_H) \cos 2\theta_0 + H \cos(\theta_H - \theta_0)} , \quad (5.6)$$

$$\Delta\phi = \frac{-\Delta H_x \sin\phi_H + \Delta H_y \cos\phi_H}{-H_l \sin\theta_0 \cos 2\phi_H + H \sin\theta_H} . \quad (5.7)$$

Equations (5.6) and (5.7) can be further simplified in the particular field and magnetic anisotropy configurations. Below, we discuss two scenarios that will be used in the measurements. The DT field $\vec{h}_{DT} = -b\vec{\sigma} \times \vec{m}/\gamma$ is always normal to the magnetization and the FT field $\vec{h}_{FT} = -a\vec{\sigma}/\gamma$ does not depend on the magnetization. One can separate the DT and FT based on their symmetries with respect to the magnetization.

5.3.1 External Magnetic Field Parallel to the Current

As illustrated in Figure 5.3, in the configuration where the external magnetic field is parallel to the current, we apply both the external magnetic field and in-plane current along the x -axis, leading to spin-polarization $\vec{\sigma}$ in the y direction. We call this set up the $H||I$ configuration. The effective field arising from DT and FT cause the magnetization to deviate from its equilibrium direction. In addition to the SOTs, the current generates an Oersted field, \vec{h}_{Oe} , along the y direction. One can write the current-induced effective fields as

$$\begin{aligned}\Delta H_x &= -h_{DT} \cos\theta_0 \\ \Delta H_y &= h_{FT} + h_{Oe} \\ \Delta H_z &= h_{DT} \sin\theta_0\end{aligned}\tag{5.8}$$

In this geometry, the external magnetic field is applied in the x - z plane, so $\phi_0 = \phi_H = 0^\circ, \theta_H \approx 90^\circ$.

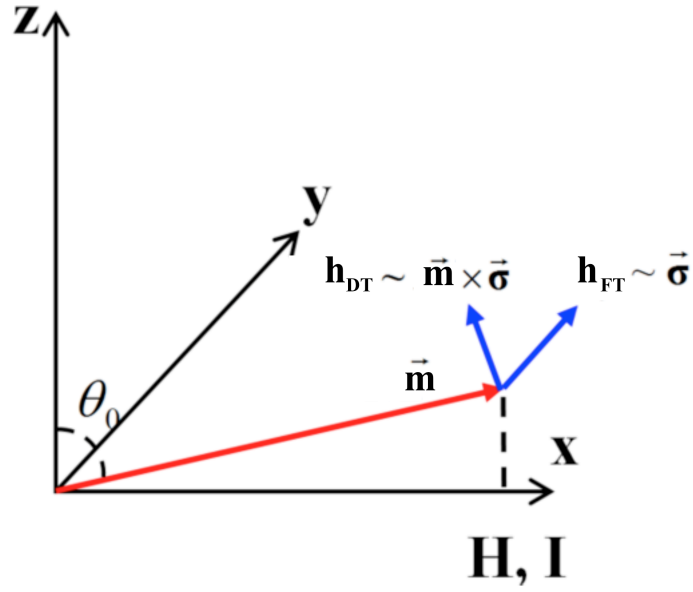


Figure 5.3: A sketch of DT and FT in the $H \parallel I$ configuration for multilayer thin films with PMA.

Then by substituting Eq. (5.8) into Eqs. (5.6) and (5.7), we obtain the modulation of the magnetization angle as

$$\Delta\theta = -\frac{h_{DT}}{H_p \cos 2\theta_0 + H \sin \theta_0}, \quad (5.9)$$

$$\Delta\phi = \frac{h_{FT} + h_{0e}}{H - H_l \sin \theta_0}. \quad (5.10)$$

From this it is clear that DT changes the polar angle of the magnetization and FT changes the azimuthal angle of the magnetization.

5.3.2 External Magnetic Field Perpendicular to the Current

In the second geometry, the $H \perp I$ configuration, depicted in Figure 5.4, we apply the magnetic field along the y -axis so that the magnetization rotates in the y - z plane, so $\phi_0 = \phi_H = 90^\circ, \theta_H \approx 90^\circ$.

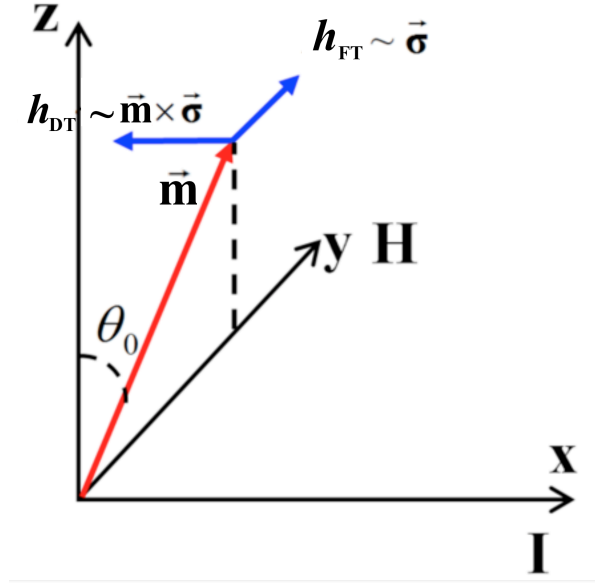


Figure 5.4: A sketch of DT and FT in the $H \perp I$ configuration for multilayer thin films with PMA.

The in-plane current along the x -axis creates the same spin polarization $\vec{\sigma}$ as the previous configuration. Therefore, the y -component of the current-induced effective field stays the same. The effective field due to the DT is in the x -direction. One can write the current-induced effective fields as

$$\begin{aligned}\Delta H_x &= -h_{DT}, \\ \Delta H_y &= h_{FT} + h_{Oe}.\end{aligned}\tag{5.11}$$

By substituting Eq. (5.11) into Eqs. (5.6) and (5.7), we obtain the expressions of magnetization change as

$$\Delta\theta = \frac{(h_{FT} + h_{Oe})\cos\theta_0}{(H_p - H_l)\cos 2\theta_0 + H\sin\theta_0},\tag{5.12}$$

$$\Delta\phi = \frac{h_{DT}}{H + H_l\sin\theta_0}.\tag{5.13}$$

In this scenario, the modulation of the polar angle $\Delta\theta$ is proportional to the FT and Oersted field, and the modulation of the azimuthal angle $\Delta\phi$ depends on the DT.

5.4 Detection of DT and FT with the Adiabatic Harmonic Hall Technique in Ta/CoFeB/MgO trilayers with PMA

The effective fields of SOTs alter the magnetization angle, resulting in a change of the Hall signal. The Hall voltage consists of the AHE and planar Hall (PHE) contributions. The detected signal was mostly attributed to AHE because AHE response is usually much larger than PHE in typical ferromagnetic metals and their alloys [8,17,18].

In the experiment, a sinusoidal ac current I_{ac} with the frequency of 323.4 Hz is applied to the Hall bar along the x -axis. The amplitude of I_{ac} is 5.7 mA. The resistivity of CoFeB and Ta thin film at 1 nm are 246 and 256 $\mu\Omega cm$, respectively. Assuming the bilayer can be modeled as a parallel circuit, the electric current density in Ta is $0.38 \times 10^6 \text{ A cm}^{-2}$. The current causes small oscillations of the magnetization through SOTs and the Oersted field, leading to first- and second-order harmonic Hall voltages detected by a lock-in amplifier. The dc AHE signal is related to the polar angle of magnetization as $V_A = \frac{1}{2} \Delta R_A I \cos\theta$ and the dc PHE signal is given by

$V_P = \frac{1}{2} \Delta R_P I \sin^2\theta \sin 2\phi$. When the azimuthal angle ϕ_0 is 0° or 90° , the expressions of

the harmonic Hall voltages are

$$V_\omega = \frac{1}{2} \Delta R_A I_{ac,FM} \cos\theta_0 \quad (5.14)$$

$$V_{2\omega} = \frac{1}{2} I_{ac,FM} \sin\theta_0 \left(\Delta R_A \Delta\theta \pm \frac{1}{2} \Delta R_P \sin\theta_0 \Delta\phi \right), \quad (5.15)$$

where $I_{ac,FM}$ is the ac current in the FM layer that is equal to 1.9 mA, and the sign in Eq. (5.15) is negative when $\phi_0 = 0^\circ$ and positive when $\phi_0 = 90^\circ$. The AHE voltage dominates the Hall signal.

In order to separately determine h_{DT} and h_{FT} , we performed the Hall measurements in the two configurations described above. The magnetic field is applied in the film plane with a small tilting angle ($\theta_H = 85^\circ$) to avoid the formation of domain walls. We plot the first- and second-order Harmonic response as a function of the external field in Figures 5.5 (a) and (b). The magnetic switching does not vary with applied field, indicating a single domain state. It is important to note that domain structures could be created at high polar angles. Structures of sub-100-nm dimensions would enable the validation of the single-domain assumption.

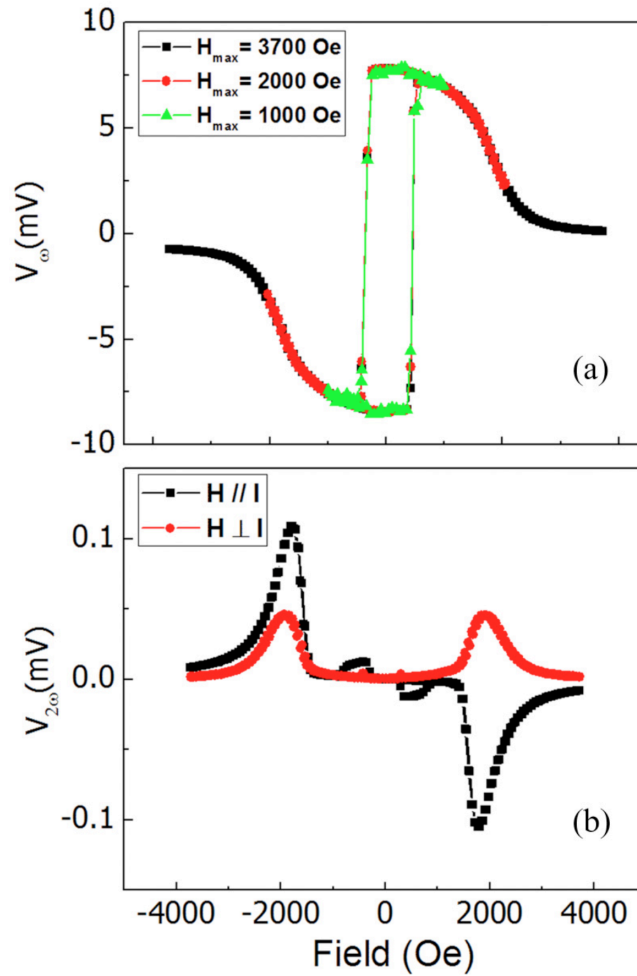


Figure 5.5: (a) First-order harmonic loops under different applied fields; (b) second-harmonic loops under the $H \parallel I$ and $H \perp I$ geometries.

In the $H \parallel I$ configuration, the modulation of polar angle $\Delta\theta$ is proportional to h_{dT} , expressed in Eq. (5.9). Therefore, the second-harmonic signal is mostly attributed to damping-like torque. The first-order Hall voltage reduces with the increase of magnetic field. The plot of the DC polar MOKE signal as a function of the external magnetic field is shown in Figure 5.6. The equilibrium polar angle θ_0 of magnetization at each magnetic field is obtained from the first-harmonic Hall response

by Eq. (5.14). From Eqs. (5.9) and (5.15), we obtain the expression of second-harmonic voltage as

$$V_{2\omega} = \frac{1}{4} \Delta R_A I_{ac,FM} \frac{\sin \theta_0 h_{DT}}{H_p \cos 2\theta_0 + H \sin \theta_0} - \frac{1}{2} \Delta R_P I_{ac,FM} \frac{\sin^2 \theta_0 (h_{FT} + h_{0e})}{H - H_l \sin \theta_0}. \quad (5.16)$$

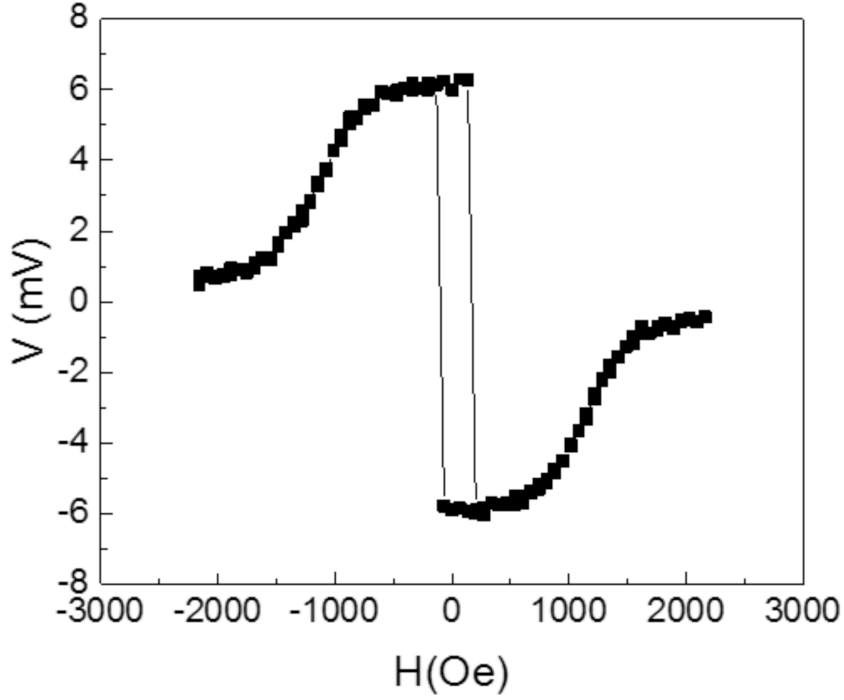


Figure 5.6: DC polar MOKE signal as a function of the external magnetic field.

Figure 5.7(a) shows the fitting of the second-harmonic data from Eq. (5.16) with parameters of $h_{DT} = 1.2$ Oe, $h_{FT} = 2.9$ Oe, $H_p = 2070$ Oe and $H_l = 50$ Oe. Here, the effective perpendicular field H_p is determined as the magnetic field at which the magnetization saturates along the film plane, as seen in the first-order harmonic loop in Figure 5.5(a).

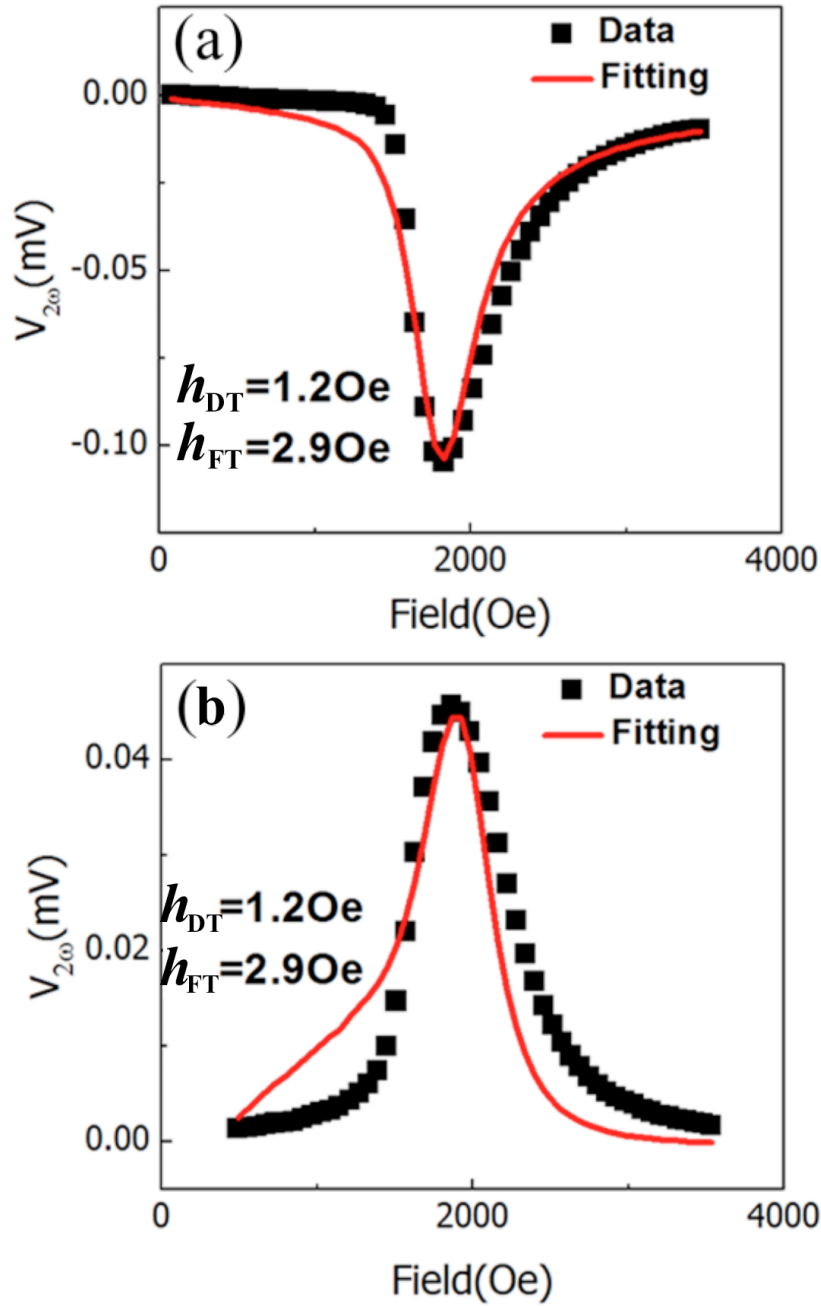


Figure 5.7: The fitting of second-harmonic curves under (a) $H \parallel I$ and (c) $H \perp I$ geometries. The fitted values are $h_{DT} = 1.2 \text{ Oe}$ and $h_{FT} = 2.9 \text{ Oe}$.

Similarly, in the $H \perp I$ configuration, we derive the second-harmonic response expressed as

$$V_{2\omega} = \frac{1}{4} \Delta R_A I_{ac,FM} \frac{\sin\theta_0 \cos\theta_0 (h_{FT} + h_{Oe})}{H_p \cos 2\theta_0 + H \sin\theta_0} - \frac{1}{2} \Delta R_P I_{ac,FM} \frac{\sin^2\theta_0 h_{DT}}{H - H_l \sin\theta_0}. \quad (5.17)$$

The AHE voltage is dominated by field-like torque. We fit the second-harmonic curve in Figure 5.7(b) using Eq. (5.17) with the same parameters as in Figure 5.7(a). We neglect the current-induced Oersted field in both situations because it is much smaller than the SOT fields. The in-plane Oersted field is calculated from Ampere's law as $h_{Oe} = I/2w = 0.04$ Oe, where $w = 500 \mu\text{m}$ is the width of the Hall bar and the current in Ta is $I = 3.8$ mA. We then calculate the coefficients of the SOTs as $h_{DT}/j_{Ta} = 3.160\text{e}/10^6 \text{ Acm}^{-2}$ and $h_{FT}/j_{Ta} = 7.630\text{e}/10^6 \text{ Acm}^{-2}$. Assuming h_{DT} is only caused by the SHE, we calculate the spin Hall angle at the perpendicular state as $\theta_{SH} = 2eM_s t h_{DT} / \hbar j_{Ta} = 0.09$, where e is the electron charge, $M_s = 10^6$ A/m is the saturation magnetization of CoFeB, and the thickness of CoFeB $t = 1$ nm.

We extract the angular dependence by fitting the second-harmonic Hall data. The damping-like torque increases with polar angle and becomes a maximum when the magnetization is in the film plane due to the angular dependence of Rashba-induced SOTs. The values of h_{DT} and h_{FT} have been held constant in the fitting, i.e., no dependence on the magnetization direction. The deviations between the experimental and theoretical curves in Figures 5.7 (a) and (b) indicate the angular dependence of h_{DT} and h_{FT} [18]. By solving Eqs. (5.16) and (5.17) with known values of $V_{2\omega}$, ΔR_A , ΔR_P , $I_{ac,FM}$, θ_0 , H_p and H_l , we calculate the effective fields due to SOTs at each polar angle θ_0 . It is important to note that the dependence of h_{DT} and h_{FT} on the azimuthal angle ϕ_0 is neglected, which might cause some additional errors [24]. As

shown in Figures 5.8(a) and (b), both h_{DT} and h_{FT} increase with the polar angle and reach the maximum magnitude when the magnetization is in the film plane.

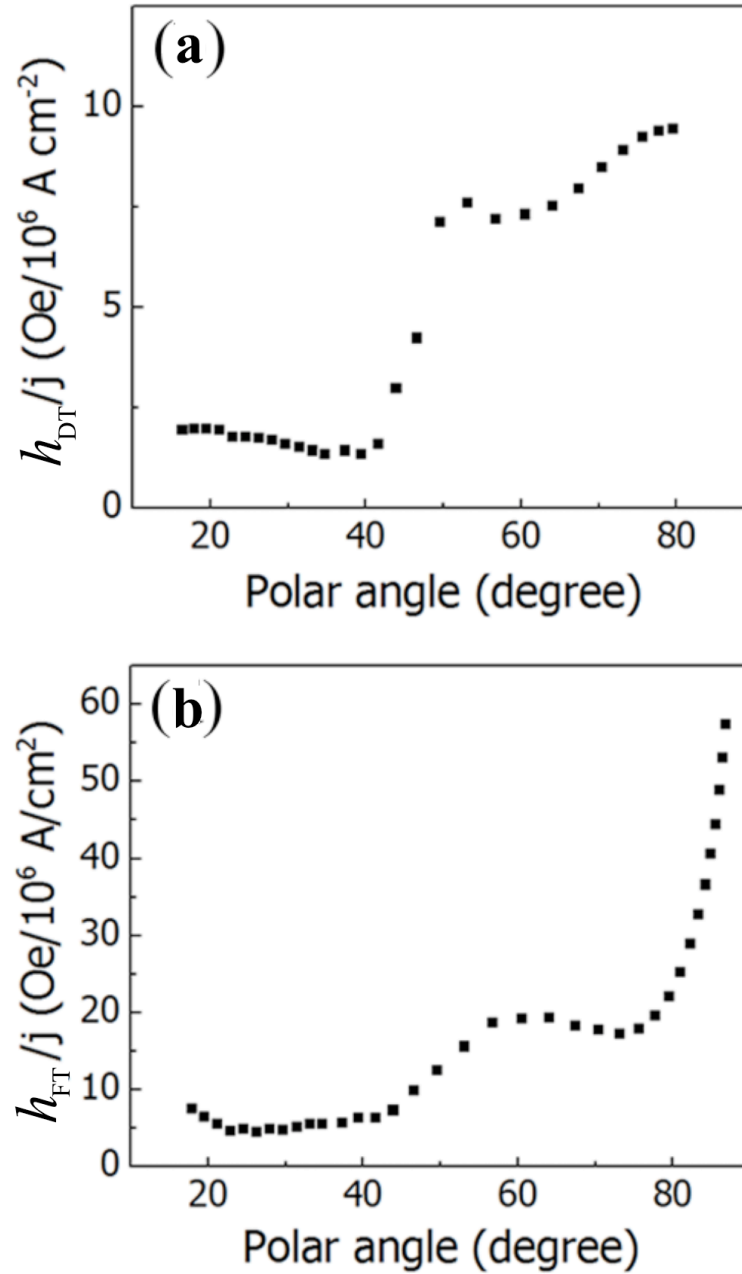


Figure 5.8: (a) The coefficient of damping-like torque and (b) field-like torque as a function of the polar angle of \vec{m} .

The profile of the SOTs between 40° and 70° owes to the uncertainty of the calculation. The fitting curves do not vary much in the low- and high-field regions corresponding to different effective anisotropy fields H_p , shown in Figure 5.9, suggesting the harmonic Hall measurements are accurate. However, the fitting results are sensitive to the effective anisotropy field near the peak, where the polar angle of the magnetization is between 40° and 70° . A small uncertainty in the value of H_p leads to a significant error in the calculation. As shown in Figure 5.9, a less than 5% change (90 Oe) in H_p leads to a large variation of the fitting curves in both configurations. In conclusion, the harmonic Hall technique may not be an accurate method to study the angular dependence of SOTs. In the next part, we will demonstrate a proper measurement scheme with the MOKE technique and field calibration.

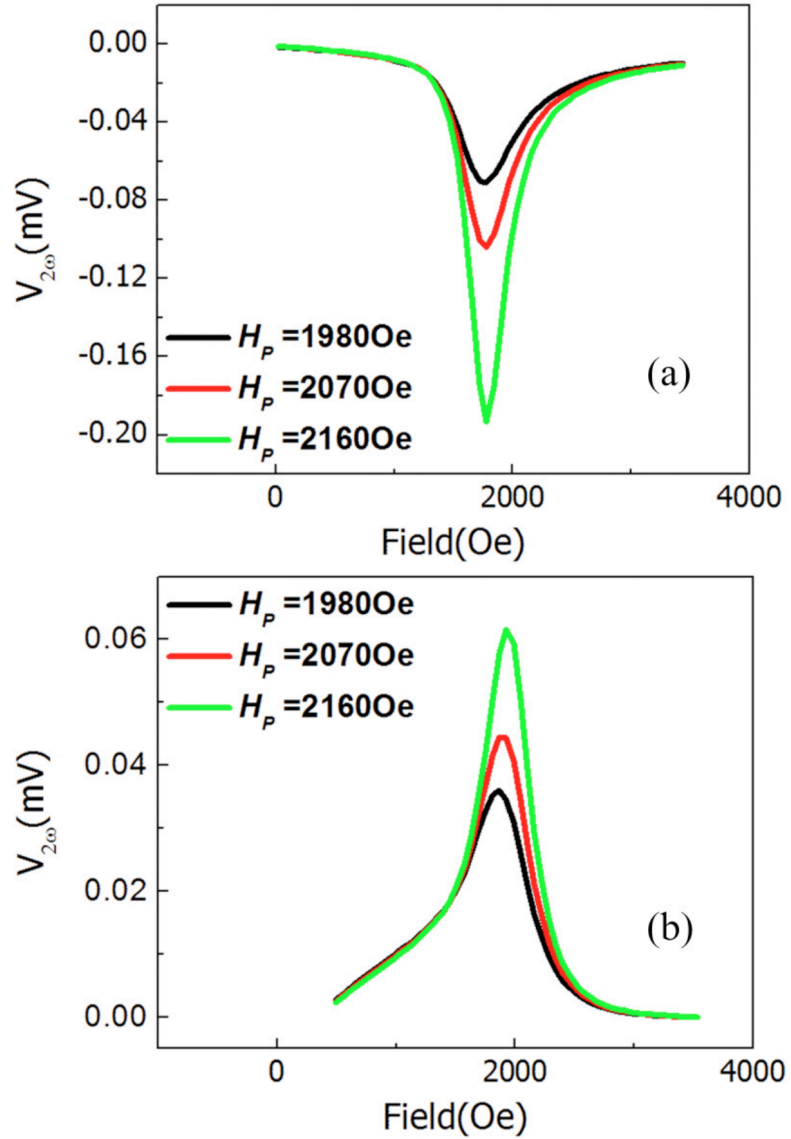


Figure 5.9: The fitting curves of second-harmonic voltage with different values of perpendicular anisotropy field H_p in (a) the $H \parallel I$ and (b) the $H \perp I$ configurations.

5.5 Detection of DT and FT with MOKE in Ta/CoFeB/MgO trilayers with PMA

As we have shown in Chapter 4, the MOKE with normal incidence light polarized linearly at 45° has only polar contribution [25]. The two measurement

geometries described above can be used to determine both the DT and FT using only polar MOKE.

In the $H \parallel I$ configuration, where the external magnetic field is applied in the x - z plane and $\phi_0 = \phi_H = 0^\circ, \theta_H \approx 90^\circ$, the relation between the current-induced SOT fields and the modulation of the magnetization has been shown in Eqs. (5.9) and (5.10). According to Eq. (5.9), the polar angle $\Delta\theta$ is proportional to h_{DT} and since we use normal incident light with 45° linear polarization with respect to the x -axis, the signal only depends on the polar angle as

$$\Delta V \propto \alpha_{polar} \sin\theta_0 \Delta\theta . \quad (5.18)$$

Therefore, we derive the polar MOKE response from Eqs. (5.9) and (5.14) as

$$\Delta V \propto \alpha_{polar} \frac{\sin\theta_0 h_{DT}}{H_p \cos 2\theta_0 + H \sin\theta_0} . \quad (5.19)$$

The MOKE configuration used in the measurements is depicted in Figure 5.10. The Ta/CoFeB/MgO trilayer is patterned into a $30 \mu\text{m} \times 30 \mu\text{m}$ square with two contact pads. A long conducting strip consisting of Ta (5 nm)/Cu (200 nm)/Au (50 nm) is fabricated in parallel with the sample for the purpose of field calibration. The width of the strip $w = 30 \mu\text{m}$, and the distance d between the strip and sample is $100 \mu\text{m}$. We apply linearly polarized light at the center of the sample film and a sinusoidal in-plane AC current at 1013 Hz either in the sample (1 mA) or in the conducting strip (100 mA). The Kerr rotation of the polarization due to the magnetization reorientation is analyzed by using the optical bridge apparatus that was explained in Chapter 3 [10].

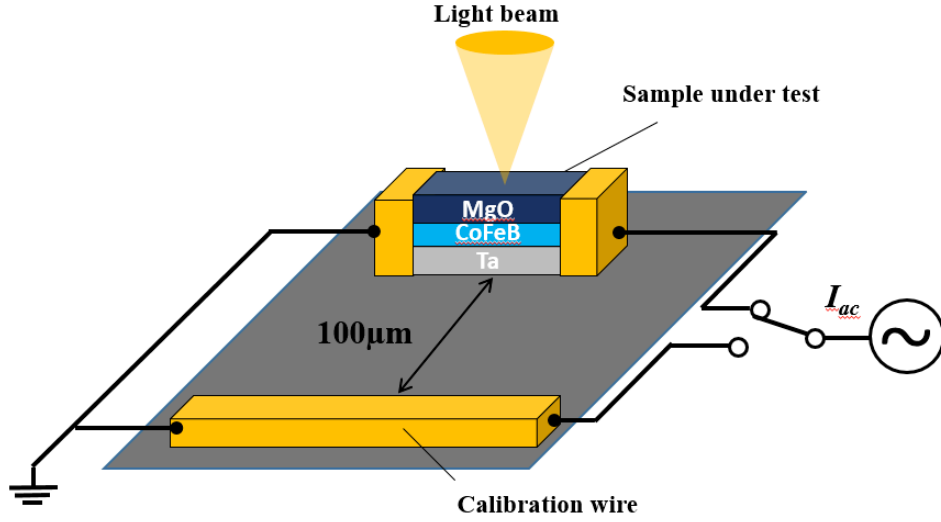


Figure 5.10: Measurement of DT and FT with the MOKE technique. Calibration is done by sending an AC current through a calibration wire that applies an out-of-plane magnetic field on the sample.

The signal is calibrated with a known field by passing current through the calibration wire. An out-of-plane magnetic field is generated on the sample that is analogous to the effect of SOT fields. The magnitude of the calibration field is given by $H_{cal} = I/2\pi d$. A 100 mA the AC current causes a $1.53 \pm 0.130e$ magnetic field, where the error is due to the finite width of the calibration strip. Magnetization reorientation due to this calibration field is given as

$$\Delta\theta = -\frac{\sin\theta_0 H_{cal}}{H_p \cos 2\theta_0 + H \sin\theta_0} . \quad (5.20)$$

Thus the polar MOKE response with current in the calibration wire is written as

$$\Delta V_{cal} \propto \alpha_{polar} \frac{\sin^2\theta_0 H_{cal}}{H_p \cos 2\theta_0 + H \sin\theta_0} . \quad (5.21)$$

Comparing Eq. (5.19) and (5.21), we obtain the DT effective field as

$$h_{DT} = \frac{\Delta V}{\Delta V_{cal}} H_{cal} \sin\theta_0 . \quad (5.22)$$

Figure 5.10 shows the plot of the polar MOKE signal corresponding to the DT (black curve) and the calibration field (red curve) as a function of the external magnetic field in the $H||I$ configuration. The MOKE signal only depends on the DT field $\vec{h}_{DT} = -b\vec{\sigma} \times \vec{m}/\gamma$; therefore, as we can see from Figure 5.11, the response due to DT changes sign with the external magnetic field while the calibration signal is symmetric since it does not change sign with the external field.

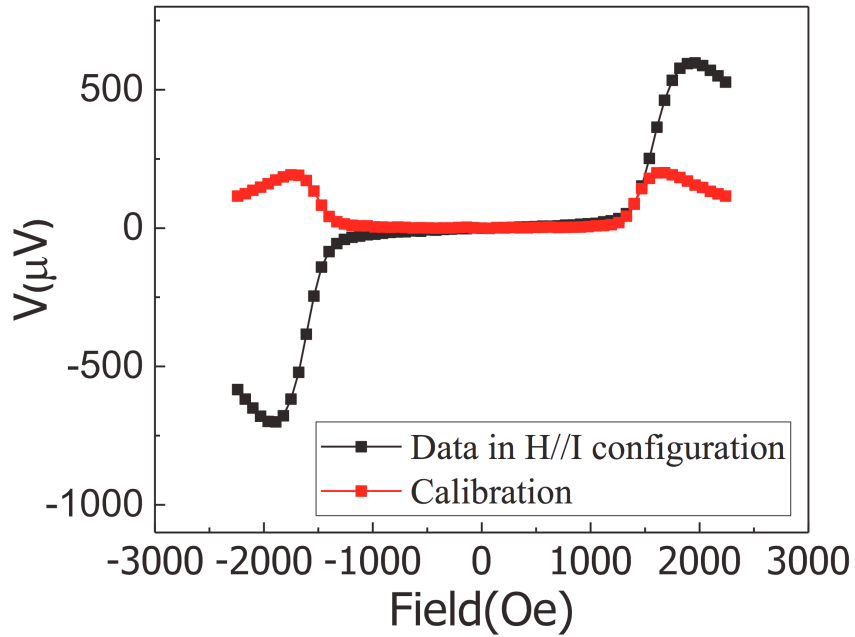


Figure 5.11: The MOKE response with 1 mA current (1.1×10^6 A/cm² current density in Ta) applied in the sample (black) and 1.53 Oe calibration field (red) under the $H||I$ configuration.

For the $H \perp I$ configuration, where the external magnetic field is applied in the y - z plane and $\phi_0 = \phi_H = 90^\circ$, $\theta_H \approx 90^\circ$, the relation between the current-induced SOT fields and the modulation of the magnetization was shown in Eqs. (5.12) and (5.13). According to Eq. (5.12) the polar angle $\Delta\theta$ is proportional to h_{FT} and h_{Oe} . We have neglected h_{Oe} in the calculation since it is one order smaller than h_{FT} due to Ta being

very resistive. With the same derivation process, we obtain the formula in the $H \perp I$ configuration to calculate the FT effective field h_{FT} as

$$h_{FT} = \frac{\Delta V}{\Delta V_{cal}} H_{cal} \tan \theta_0 . \quad (5.23)$$

Figure 5.12 shows the plot of the polar MOKE signal corresponding to the FT (black curve) and the calibration field (red curve) as a function of the external magnetic field in the $H \perp I$ configuration. The MOKE signal only depends on the DT field $\vec{h}_{FT} = -a \vec{\sigma} / \gamma$. Therefore, the curves corresponding to the FT field as well as the calibration field are symmetric with respect to the external magnetic field.

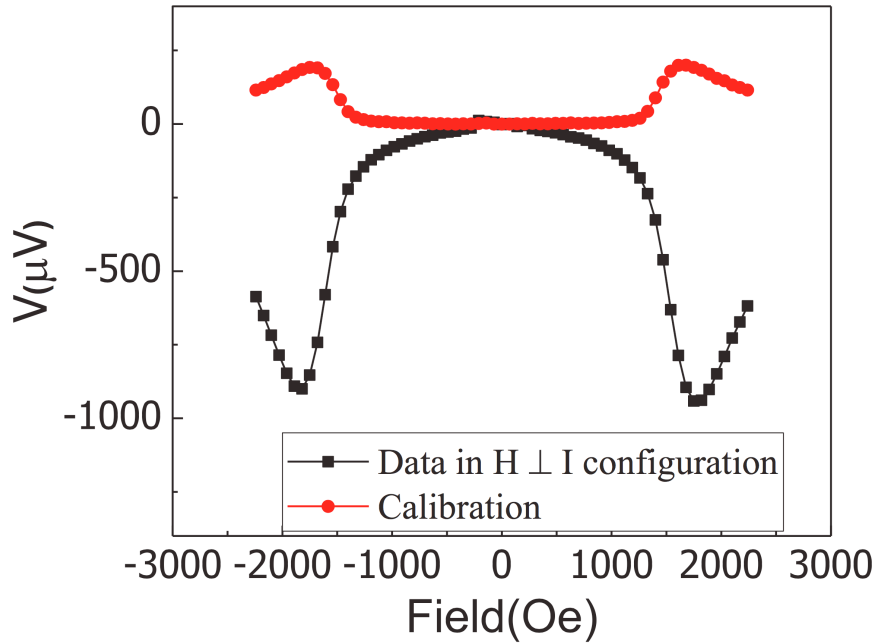


Figure 5.12: The MOKE response with 1 mA current (1.1×10^6 A/cm² current density in Ta) applied in the sample (black) and 1.53 Oe calibration field (red) under the $H \perp I$ configuration.

In each situation, we first apply current through the sample to detect the MOKE response ΔV induced by SOT effective fields. Then, we apply the current in

the calibration wire to measure the calibration signal ΔV_{cal} . From the dc MOKE, we determine the equilibrium angle θ_0 at each magnetic field as

$$\cos\theta_0 = \frac{V_{dc}}{V_{dc}(\theta_0 = 0)} \quad (5.24)$$

Using data obtained from Figures 5.11 and 5.12, we calculate h_{DT} and h_{FT} from Eq. (5.22) and Eq. (5.23) respectively. Because the MOKE technique with calibration field does not require the fitting of the measurement curve, the measurement scheme we develop here is more accurate in determining the angular dependence of SOTs than the harmonic Hall technique.

The SOT coefficients normalized to the current density in Ta, h_{DT}/j_{Ta} and h_{FT}/j_{Ta} , are plotted versus polar angle in Figure 5.12(a) and (b), respectively. The DC polar MOKE measurement is used to extract the polar angle as a function of external magnetic field. The ratio of h_{FT}/h_{DT} is around 8 in this study on PMA films, suggesting a strong Rashba effect. The ratio in the Pt/CoFeB bilayer [10] with in-plane anisotropy is much smaller, so in that case the SOTs are mostly attributed to the SHE. Both the DT and FT show non-trivial significant angular dependence. The SOTs are at a maximum near $\theta_0 = 90^\circ$. A simple theoretical calculation based on the 2D free-electron model with Rashba spin-orbit coupling also predicts similar trends in the angular dependence [21]. Based on the nontrivial angular dependence and magnitude of the SOTs, we believe the Rashba effect is the predominant mechanism in Ta/CoFeB/MgO trilayer structures. However, there are discrepancies between experimental results and theoretical predictions. In the 20–30° angle region, the SOTs are not monotonically increasing with the polar angle of magnetization. In addition, the magnitude and the increasing rate of SOTs after 60° are not reproduced in the

theoretical modeling. Our results suggest that the current theoretical model is not sufficient to describe the entire angular dependence of SOTs in this system.

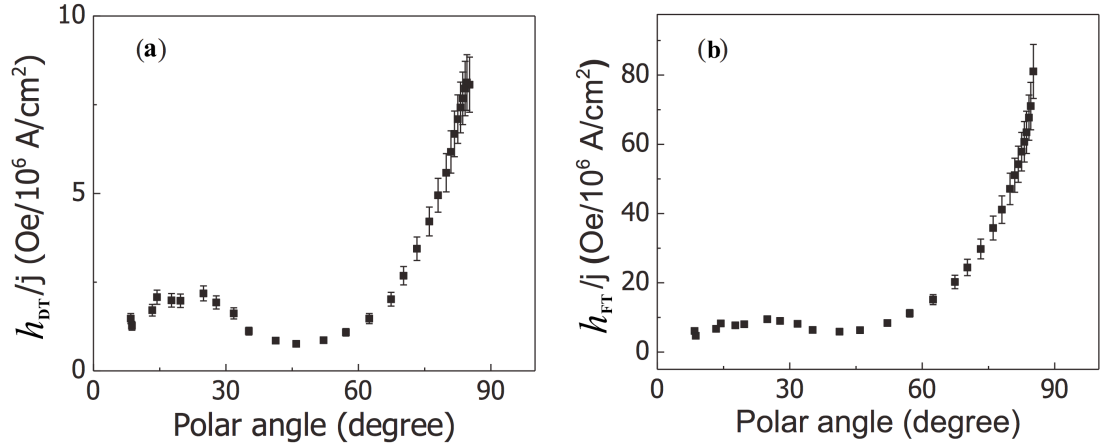


Figure 5.13: The calculated coefficient of damping-like torque (a) and field-like torque (b) as a function of the magnetization angle. Both DT and FT reach the maximum near $\theta_0 = 90^\circ$, when the magnetization lies in the film plane.

5.6 Summary

We performed MOKE measurements on Ta/CoFeB/MgO trilayers in order to quantify SOTs and also derived an algorithm to extract the angle dependence of SOTs. The second-harmonic Hall measurement technique is widely employed to quantify SOTs. We have shown that this technique is sensitive to the fitting parameters. A small change in the fitting parameters leads to a significant error in the determined SOTs for certain polar-angle regions. With the MOKE technique, we eliminate the fitting procedure by implementing a field calibration to accurately measure the SOTs. The field-like torque for this sample has a larger magnitude than the damping-like torque. Both damping-like and field-like torques reach a maximum when the magnetization lies in the film plane, as expected from a theoretical model with

interfacial Rashba spin-orbit interaction. However, the measured SOTs show a complex dependence on the polar angle of the magnetization. Further theoretical efforts are required to fully understand the mechanism of the SOTs. Accurate measurements of the angular dependence of the SOTs are also valuable to the study of magnetization dynamics induced by SOTs. Experiments as a function of layer thickness will be necessary to complete the study, and will require the quantification of the conductivity and other interfacial effects [26] at the ultrathin region.

REFERENCES

- [1] U. H. Pi, K. Won Kim, J. Y. Bae, S. C. Lee, Y. J. Cho, K. S. Kim, and S. Seo, *Appl. Phys. Lett.* **97**, 162507 (2010).
- [2] T. Suzuki, S. Fukami, N. Ishiwata, M. Yamanouchi, S. Ikeda, N. Kasai, and H. Ohno, *Appl. Phys. Lett.* **98**, 142505 (2011).
- [3] F. Freimuth, S. Blügel, and Y. Mokrousov, *Phys. Rev. B* **90**, 174423 (2014).
- [4] I. Mihai Miron, G. Gaudin, S. Auffret, B. Rodmacq, A. Schuhl, S. Pizzini, J. Vogel, and P. Gambardella, *Nat. Mater.* **9**, 230 (2010).
- [5] P. M. Haney, H.-W. Lee, K.-J. Lee, A. Manchon, and M. D. Stiles, *Phys. Rev. B* **87**, 174411 (2013).
- [6] V. P. Amin and M. D. Stiles, *Phys. Rev. B* **94**, 104420 (2016).
- [7] A. Manchon, (2012).
- [8] X. Fan, J. Wu, Y. Chen, M. J. Jerry, H. Zhang, and J. Q. Xiao, *Nat. Commun.* **4**, 1799 (2013).
- [9] L. Liu, C.-F. Pai, Y. Li, H. W. Tseng, D. C. Ralph, and R. A. Buhrman, *Science* (80-.). **336**, 555 (2012).
- [10] X. Fan, H. Celik, J. Wu, C. Ni, K. J. Lee, V. O. Lorenz, and J. Q. Xiao, *Nat. Commun.* **5**, 1 (2014).
- [11] S. Ikeda, K. Miura, H. Yamamoto, K. Mizunuma, H. D. Gan, M. Endo, S. Kanai, J. Hayakawa, F. Matsukura, and H. Ohno, *Nat. Mater.* **9**, 721 (2010).
- [12] W.-G. Wang, M. Li, S. Hageman, and C. L. Chien, *Nat. Mater.* **11**, 64 (2012).
- [13] S. Kanai, M. Yamanouchi, S. Ikeda, Y. Nakatani, F. Matsukura, and H. Ohno, *Appl. Phys. Lett.* **101**, 122403 (2012).
- [14] W.-G. Wang, S. Hageman, M. Li, S. Huang, X. Kou, X. Fan, J. Q. Xiao, and C. L. Chien, *Appl. Phys. Lett.* **99**, 102502 (2011).

- [15] H. X. Yang, M. Chshiev, B. Dieny, J. H. Lee, A. Manchon, and K. H. Shin, *Phys. Rev. B* **84**, 54401 (2011).
- [16] C. Zhang, M. Yamanouchi, H. Sato, S. Fukami, S. Ikeda, F. Matsukura, and H. Ohno, *Appl. Phys. Lett.* **103**, 262407 (2013).
- [17] J. Kim, J. Sinha, M. Hayashi, M. Yamanouchi, S. Fukami, T. Suzuki, S. Mitani, and H. Ohno, *Nat. Mater.* **12**, 240 (2013).
- [18] X. Qiu, P. Deorani, K. Narayanapillai, K.-S. Lee, K.-J. Lee, H.-W. Lee, and H. Yang, *Sci. Rep.* **4**, 4491 (2015).
- [19] K. Garello, I. M. Miron, C. O. Avci, F. Freimuth, Y. Mokrousov, S. Blügel, S. Auffret, O. Boulle, G. Gaudin, and P. Gambardella, *Nat. Nanotechnol.* **8**, 587 (2013).
- [20] C. O. Avci, K. Garello, C. Nistor, S. Godey, B. Ballesteros, A. Mugarza, A. Barla, M. Valvidares, E. Pellegrin, A. Ghosh, I. M. Miron, O. Boulle, S. Auffret, G. Gaudin, and P. Gambardella, *Phys. Rev. B* **89**, 214419 (2014).
- [21] K.-S. Lee, D. Go, A. Manchon, P. M. Haney, M. D. Stiles, H.-W. Lee, and K.-J. Lee, *Phys. Rev. B* **91**, 144401 (2015).
- [22] S. Peng, M. Wang, H. Yang, L. Zeng, J. Nan, J. Zhou, Y. Zhang, A. Hallal, M. Chshiev, K. L. Wang, Q. Zhang, and W. Zhao, *Sci. Rep.* **5**, 18173 (2016).
- [23] M. Hayashi, J. Kim, M. Yamanouchi, and H. Ohno, *Phys. Rev. B* **89**, 144425 (2014).
- [24] K. Garello, I. M. Miron, C. O. Avci, F. Freimuth, Y. Mokrousov, S. Blügel, S. Auffret, O. Boulle, G. Gaudin, and P. Gambardella, *Nat. Nanotechnol.* **8**, 587 (2013).
- [25] X. Fan, A. R. Mellnik, W. Wang, N. Reynolds, T. Wang, H. Celik, V. O. Lorenz, D. C. Ralph, and J. Q. Xiao, *Appl. Phys. Lett.* **109**, 122406 (2016).
- [26] S. Emori, T. Nan, A. M. Belkessam, X. Wang, A. D. Matyushov, C. J. Babroski, Y. Gao, H. Lin, and N. X. Sun, *Phys. Rev. B* **93**, 180402 (2016).

Chapter 6

VECTOR-RESOLVED MAGNETO-OPTIC KERR EFFECT MEASUREMENTS OF SPIN-ORBIT TORQUE

In this chapter, we demonstrate simultaneous detection of current-driven DT and FT in HM/FM bilayers by measuring all three magnetization components m_x , m_y , and m_z , using a vector-resolved MOKE technique based on quadrant detection. We investigate the magnitude and direction of SOTs in a series of Pt/Py samples, finding good agreement with results obtained via polar and quadratic magneto-optic Kerr effect measurements without quadrant detection as described in Chapter 4.

6.1 Introduction

We have shown that normal incidence light can measure both current-induced out-of-plane magnetization reorientation by polar MOKE measurements as done in Chapter 3 [1] and in-plane magnetization reorientation by second-order (quadratic) MOKE measurements as done in Chapter 4 [2] using a balanced detector. Such MOKE techniques do not suffer from electrical artifacts, and for high-sensitivity measurements potential optical artifacts such as reflectivity changes can be separated from the MOKE signal harmonically [3].

In ferromagnetic thin films, there have been several studies to determine the magnetization components vectorially [4,5]. For example, Ding *et al.* proposed a method to distinguish the pure longitudinal and polar Kerr contributions via two separate measurements interchanging the positions of a light source and a detector [6]. Yang *et al.* showed the detection of three magnetization components by changing the

different relative orientations of the optical devices: polarizer, modulator, and analyzer [7]. As an alternative that does not require changing the position of optical elements or data analysis to separate overlapping signals from different vector components, Keatley *et al.* used a scanning Kerr microscope equipped with a compact optical quadrant bridge polarimeter to measure in-plane vector hysteresis loops [8].

Here we present vector-resolved MOKE measurements of SOT based on an optical quadrant bridge detector for first-order detection of current-induced DT and FT in HM/FM bilayers over a wide range of thicknesses. With this vector-resolved MOKE technique, where normal incidence is converted to various incident angles with the help of an objective lens, one can separate the MOKE effects that are linear and quadratic in the magnetization and determine all three components of the magnetization vector. Thus, we can measure both DT and FT components simultaneously without the need to measure quadratic MOKE. We apply this method to measure DT and FT for a series of Pt/Py ($Ni_{81}Fe_{19} = Py$) samples as a demonstration of the implementation of the proposed technique. We compare our results with measurements made in Chapter 4 using polar and quadratic MOKE without quadrant detection.

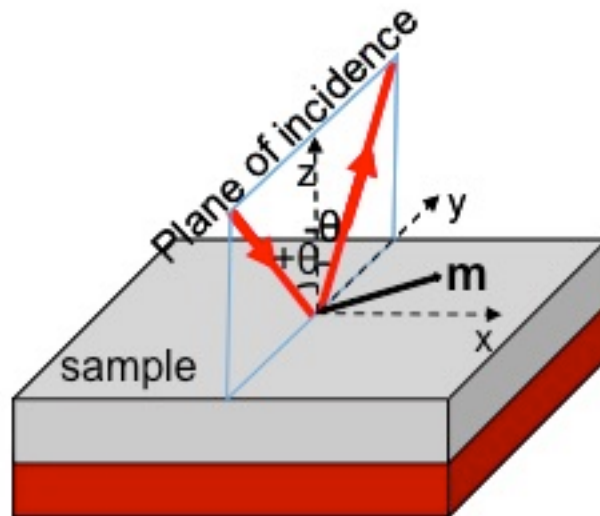
6.2 Separation of MOKE signals

As we have discussed before, the magneto-optical properties of a material can be described by the permittivity tensor, ϵ_{ij} , which can be expanded in the components of the magnetization \vec{m} acting on the material:

$$\epsilon_{ij} = \epsilon_{ij}^{(0)} + K_{ijk} m_k + G_{ijkl} m_k m_l + \dots \quad (6.1)$$

where the Einstein summation convention over the x , y , and z coordinates is used. The dielectric tensor K_{ijk} is the linear magneto-optic tensor, and G_{ijkl} is the quadratic

magneto-optic tensor. The linear response can be separated into terms corresponding to relative orientations of the unit vector of the magnetization \hat{m} , plane of incidence (POI) and sample plane (SP), with polar geometry corresponding to $\hat{m} \parallel POI$ and $\hat{m} \perp SP$, longitudinal to $\hat{m} \parallel POI$ and $\hat{m} \parallel SP$ and transverse to $\hat{m} \perp POI$ and $\hat{m} \parallel SP$ as seen in Figure 6.1. The Kerr rotation and ellipticity give a measure of the magnetization of the sample. Longitudinal and polar MOKE alter the polarization of the incident light from plane to elliptically polarized with the major axis rotated (Kerr ellipticity and rotation, respectively) [9]. Transverse MOKE does not result in a change of the polarization of the incident light. It involves a change in reflectivity for p -polarized light [10]. In this study, by using appropriate polarization conditions the transverse component is avoided.



Polar : $m \parallel z$; Longitudinal : $m \parallel y$; Transverse : $m \parallel x$

Figure 6.1: Polar, longitudinal, and transverse MOKE geometries for a sample with magnetization m .

Since the Kerr effect exists for any arbitrary direction of the magnetization, for oblique incidence the detected MOKE signal $\Psi(m)$ from a sample with magnetization \vec{m} can be written as (assuming the transverse component is suppressed):

$$\Psi(m) = \alpha_{polar} m_z + \gamma_{longitudinal} m_y + \delta_{longitudinal} m_x + \beta_{quadratic} m_x m_y + \dots \quad (6.2)$$

where the z direction is perpendicular to the magnetic film plane (see Figure 6.1), the y direction is parallel to the plane of the incident polarization, and α_{polar} , $\gamma_{longitudinal}$, $\delta_{longitudinal}$, and $\beta_{quadratic}$ are the coefficients for the polar, longitudinal, and quadratic MOKE responses, respectively.

It has been demonstrated that polar and longitudinal signals can be separated by measuring the Kerr signal in two reversed geometries [11], as the polar signal does not change sign if the angle of incidence is reversed from $+\theta$ to $-\theta$ but the longitudinal signal does change sign. That is, polar MOKE is an even function whereas longitudinal MOKE is an odd function of the incident angle. Quadratic MOKE is also an even function of the incident angle as shown in ref [12]. Thus, light incident at $-\theta$ (e.g. travelling from ray III to ray II in Figure 6.2) has the same sign for polar and quadratic signals but opposite sign for longitudinal signals as light incident at $+\theta$ (e.g. travelling from ray II to ray III in Figure 6.2).

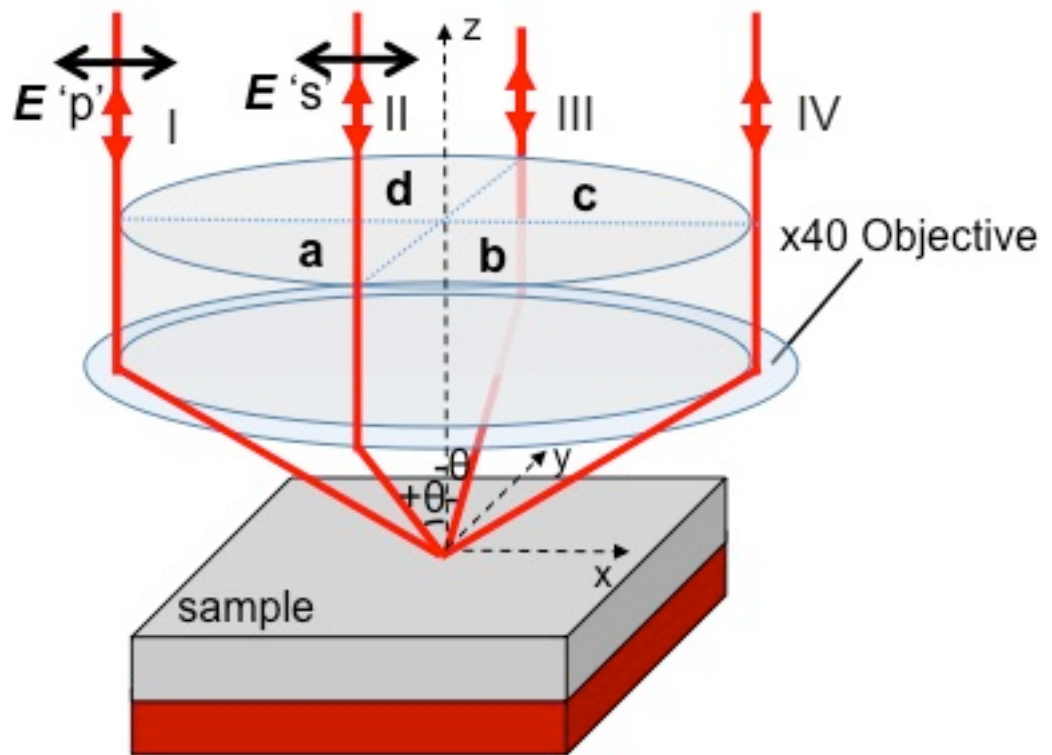


Figure 6.2: Geometry of the optical quadrant bridge detection system. A 40 \times objective focuses light transmitted to and collimates light reflected from the sample. The reflected light is detected in spatial quadrants *a*, *b*, *c*, and *d*. By adding and subtracting signals from appropriate quadrants, one can isolate the in-plane MOKE response from the out-of-plane MOKE response.

Using the even and odd dependence on the incident angle we are able to separate polar, longitudinal, and quadratic MOKE responses. Using a microscope objective with high numerical aperture ($NA = 0.65$ in our set-up), we focus light across a wide range of incident angles from perpendicular to the sample plane to oblique (up to approximately 40°) [8]. The light reflected from the sample is measured in four quadrants, as shown in Figure 6.2. By taking sums or differences of the four quadrants we obtain the contributions from the polar, longitudinal, and quadratic responses, with

the longitudinal contribution antisymmetric with incident angle. Thus, the response for angles of incidence θ with inward ($+\theta$) and outward ($-\theta$) propagation can be represented as

$$\theta_K^{\pm\theta} = \theta_K^P \pm \theta_K^L + \theta_K^Q, \quad (6.3)$$

where $\theta_K^{\pm\theta}$ are the Kerr rotations for the respective angles of incidence, and θ_K^P , θ_K^L , and θ_K^Q are the rotations for the polar, longitudinal, and quadratic magneto-optic Kerr effects, respectively. The quadrant detector allows us to either sum or subtract the inward ($\theta_K^{+\theta}$) and outward ($\theta_K^{-\theta}$) signals to obtain the desired Kerr rotations. By taking the sum of both inward ($\theta_K^{+\theta}$) and outward ($\theta_K^{-\theta}$) signals, one obtains twice the sum of the polar and quadratic Kerr rotations:

$$\theta_K^+ + \theta_K^- = 2(\theta_K^P + \theta_K^Q). \quad (6.4)$$

Since we add the signals from the two halves together, which corresponds to the signal measured at normal incidence, this signal does not have contributions from longitudinal or transverse MOKE. Measurement at 45 degree polarization can be performed to cancel the quadratic contribution, which enables us to determine the polar contribution, and in turn the DT term. Details of the methodology for separating polar and quadratic responses is explained in Chapter 4 [2]. By taking the difference of both inward ($\theta_K^{+\theta} = \text{ray II}$) and outward ($\theta_K^{-\theta} = \text{ray III}$) signals, one obtains twice the longitudinal Kerr rotation:

$$\theta_K^+ - \theta_K^- = 2\theta_K^L. \quad (6.5)$$

This allows determination of one in-plane magnetization component, m_y . For the longitudinal measurements, the incident light is p -polarized, but we take the difference of signals related to rays II and III in Figure 6.2, which corresponds to s -polarized light; thus, no transverse MOKE signal is measured. The other in-plane magnetization

component, m_x , can be gathered by subtracting the right (ray I) and the left (ray IV) halves of the beam. To suppress the transverse component for rays I and IV, the incoming polarization is changed from p - to s -polarization. The Kerr rotation from the FT term and other in-plane longitudinal components can be measured in this way. In principle, a magnetization term proportional to $m_x m_z$ may generate a hysteresis-like signal in the longitudinal configuration due to the out-of-plane Oersted field, but this term is anticipated to be less than two orders of magnitude smaller than the first-order signal and the measured signals do not indicate any substantial contribution from this term.

6.3 Measurement Setup and Determination of DT and FT with Vector-Resolved MOKE

A diagram of our vector-resolved MOKE setup is shown in Figure 6.3. Collimated light from a 100 mW diode laser at 785nm center wavelength goes through a Glan Taylor polarizer with an extinction coefficient of $\sim 10^{-4}$ to set the polarization. The angle of polarization is controlled with a half-wave plate (HWP-2) before being focused by a microscope objective of numerical aperture 0.65 on the sample. The reflected beam passes back through the objective and HWP-2 and is reflected by a 90/10 beam splitter. It goes through another half-wave plate (HWP-3) and the vertical and horizontal polarization components are split by a Wollaston prism. The intensity of the two components are balanced by adjusting HWP-3. The polarization components are detected by two quadrant photodiode detectors whose outputs are the sums or differences of various halves of the beams. The outputs of the detectors are subtracted from each other to achieve common mode rejection and doubling of the signal and then amplified. The signal is measured by a lock-in amplifier locked to the

frequency of the ac current driving the sample. Some useful tips in setting up the MOKE magnetometer is given in Appendix C. We have used the same set of samples we used in Chapter 4, namely in-plane magnetized substrate/Pt(6 nm)/Py (d_{Py}) bilayers, with d_{Py} ranging from 2 to 10 nm to verify the accuracy of this method by comparing results found by two different methods.

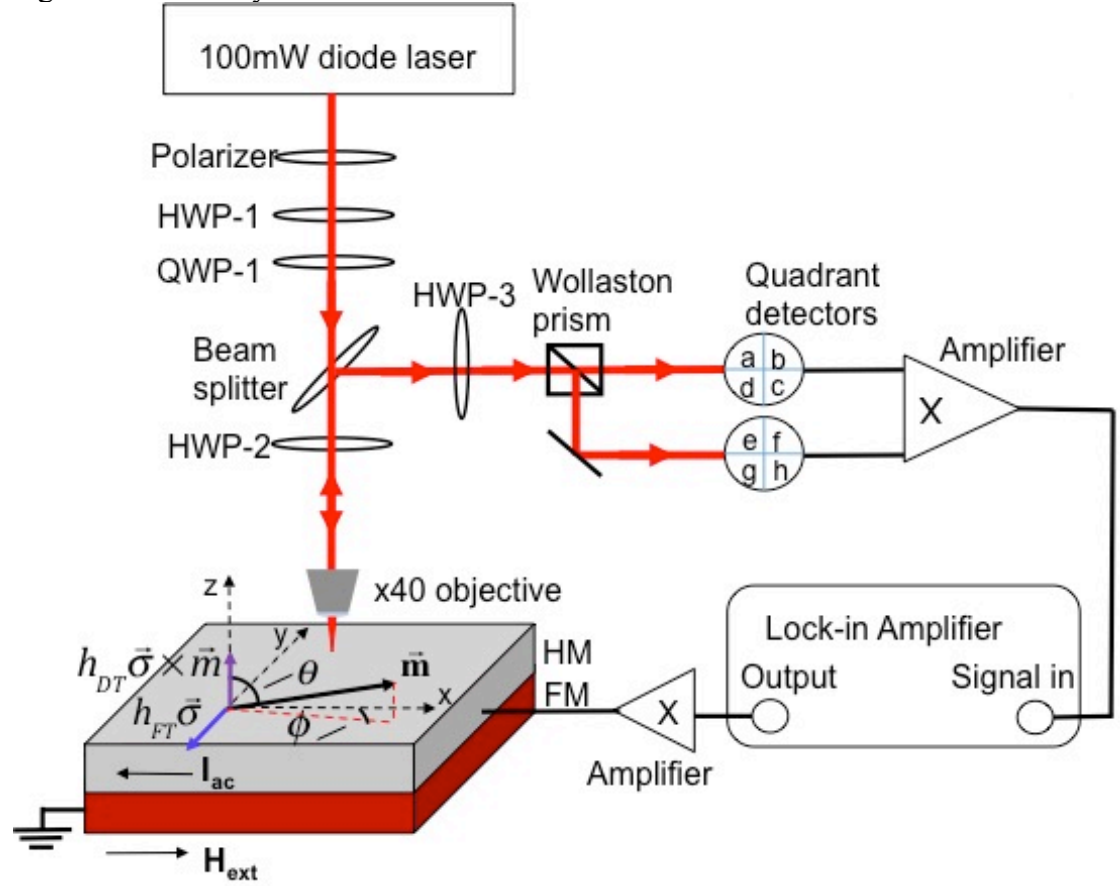


Figure 6.3: Experimental setup for the optical detection of spin-orbit torques. HWP: half-wave plate, QWP: quarter-wave plate.

We apply an in-plane ac current, $I_{ac} \cos \omega t$, at 1733 Hz with $I_{ac} = 20$ mA along the x-axis to the sample. An external magnetic field H_{ext} is applied along the x-axis to align

the magnetization. The current-induced FT and DT rotate the magnetization within the sample plane (changing ϕ_M) and perpendicular to the plane (changing θ_M), respectively. Examples of experimental results from 50 $\mu\text{m} \times 50 \mu\text{m}$ Py(8)/Pt(6) with a 20 mA bias current and 1 mW laser power are shown in Figure 6.4(a) and (b). The current-induced spin-orbit torque signals obtained by the MOKE measurements exhibit the expected linear dependence on the applied current density [1]. Figure 6.4(a) shows the raw data for the Py(8)/Pt(6) polar term (m_z) obtained using light at 45 degree polarization and taking the sum of all quadrants. The change in the polar MOKE signal ($\Delta\theta_M \propto \vec{\sigma} \times \vec{m}$) switches sign as the magnetization switches and is independent of H_{ext} away from zero field since $H_{ext} \ll M_s$. Figure 6.4 (b) shows the current-induced change in the longitudinal MOKE signal (m_y) at 0 degree polarization (at which polarization the transverse component is suppressed) exhibits a $1/H_{ext}$ dependence (proportional to $\Delta\phi_M \propto \vec{\sigma}$).

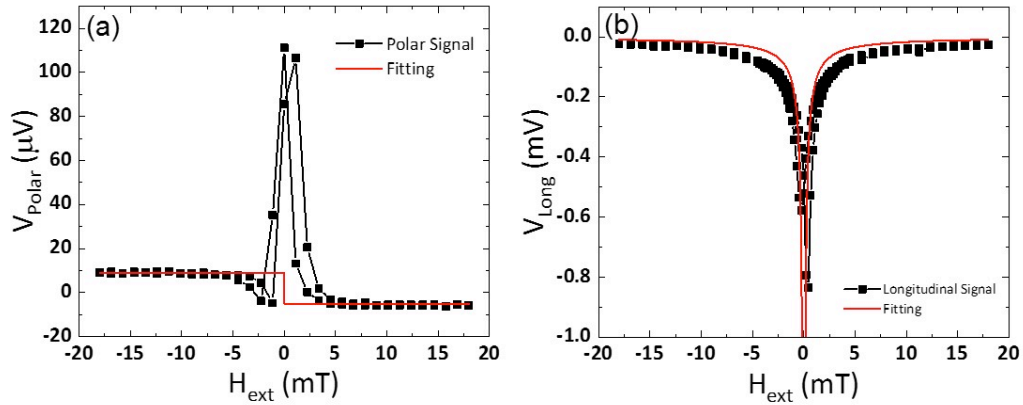


Figure 6.4: The current-induced (a) polar and (b) longitudinal response as a function of swept magnetic field H_{ext} in Py(8)/Pt(6) bilayers. The red lines are least-squares fits to a step function and to $\sim 1/H_{ext}$ for the polar and longitudinal responses, respectively.

The magnitude of the DT is determined through the self-calibration method explained in Chapter 3. Using a simple parallel circuit model to account for the different resistivities of Pt and Py, we estimate that approximately 42% of the current flows through the Pt, yielding a current density in Pt $j_{Pt} = 2.8 \times 10^{10} \text{ A/m}^2$. Note that the parallel circuit model does not take into account the potential for non-uniform conductance and thus may lead to overestimation of the current in the nonmagnetic layer [13]. A line scan is performed by keeping the laser position fixed and translating the sample along the y direction. The difference between lock-in voltages at positive saturation field and negative saturation field are taken for the DT signal and the summation of the lock-in voltages at positive saturation field and negative saturation field are taken for the out-of-plane Oersted field for each position, as seen in Figure 6.5. By fitting the lines scans using quadrant detectors for the DT signal and out-of-plane Oersted field, we extract the DT coefficient $\beta_T = \frac{h_{DT}}{j_{Pt}} = 6.970 \pm 0.050 \text{ nm}$. The effective spin Hall angle is defined as the ratio of the out-of-plane spin current to the in-plane charge current and is given by $\theta_{SH} = \beta_T \left(\frac{2e}{h} \right) \mu_0 M_s d_{Py}$. Since the spin-orbit torques consist of two components – DT and FT – two spin Hall torque efficiencies are calculated. Assuming that the DT arises from the spin Hall effect and using the equation $\theta_{SH} = \beta_T \left(\frac{2e}{h} \right) \mu_0 M_s d_{Py}$, we determine an effective spin Hall angle for DT, $\theta_{DT} = 0.086 \pm 0.007$ from vector-resolved MOKE for Pt, which is the same as that obtained with polar and quadratic MOKE without quadrant detection $\theta_{DT} = 0.086 \pm 0.004$ [2]. Here the parameters used are $\mu_0 M_s d_{Py} = 4.080 \text{ T.nm}$.

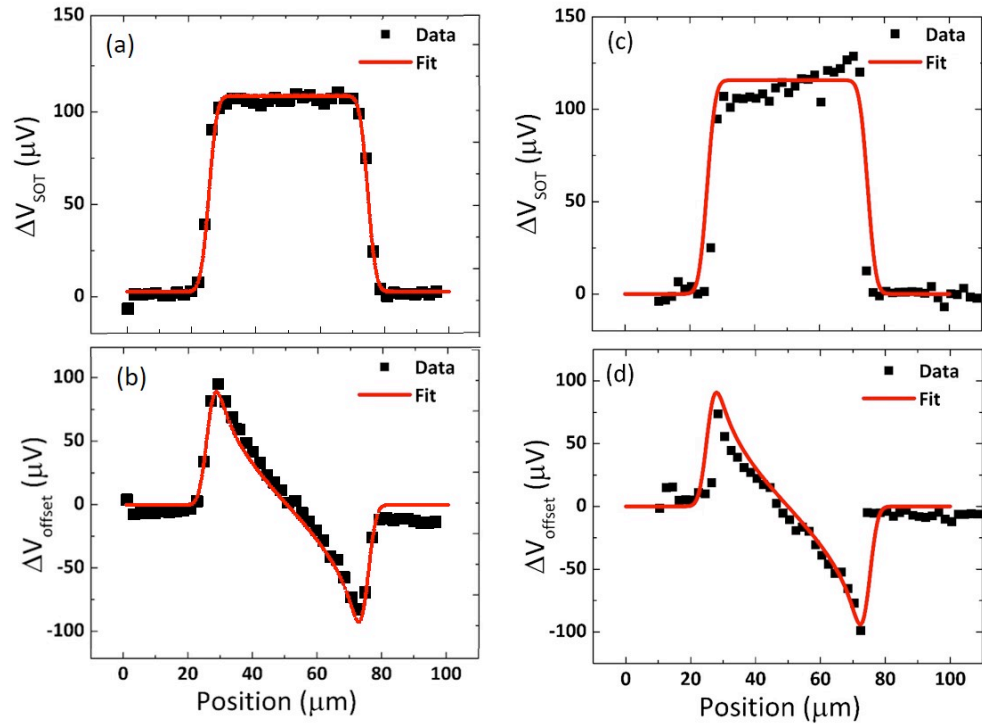


Figure 6.5: (a) Line scan result for Py(4)/Pt(6) with balanced detector. Out-of-plane equivalent spin-orbit field detected by subtracting signals taken at positive and negative saturation field. Fit function (red line) is calculated as the integration of the SOT-induced magnetization reorientation weighted by the Gaussian function that describes the spatial distribution of the laser. (b) Out-of-plane Oersted field detected by addition of signals taken at positive and negative saturation field. The fit function for the Oersted field (red line) is similarly calculated as the integration of the local magnetization reorientation weighted by the Gaussian function that describes the spatial distribution of the laser. (c), (d) Line scan results for Py(4)/Pt(6) with quadrant detectors.

To determine the magnitude of the FT we perform a calibration by passing an ac current (500 mA) only through a metallic wire (1 mm wide and 1 cm long) behind the sample that drives in-plane magnetization reorientation due to Ampere's law. Since this current is not passing through the sample, it does not contribute to spin orbit

torques. This ac current generates an Oersted field of 70.700 ± 2.940 A/m. The distance from the sample to the wire is about 1.050 ± 0.050 mm. The magnitude of the FT is extracted using a linear regression algorithm by comparing the FT signal curve and the calibration curve shown in Figure 6.6 (a) for Py(8)/Pt(6). In this example fitting, the ratio between the signals corresponding to the current-induced effective field and the calibration field is 2.490 ± 0.070 , which corresponds to a current-induced field of 176.080 ± 5.310 A/m. After removing the 83.800 A/m Oersted field generated by the current in the sample, we obtain $h_{FT} = 92.280 \pm 5.310$ A/m, which gives an effective spin Hall angle of $\theta_{FT} = 0.054 \pm 0.003$. As seen in Figure 6.6 (b), we also measure the change in the other in-plane magnetization component, m_x , which is negligibly small, as expected.

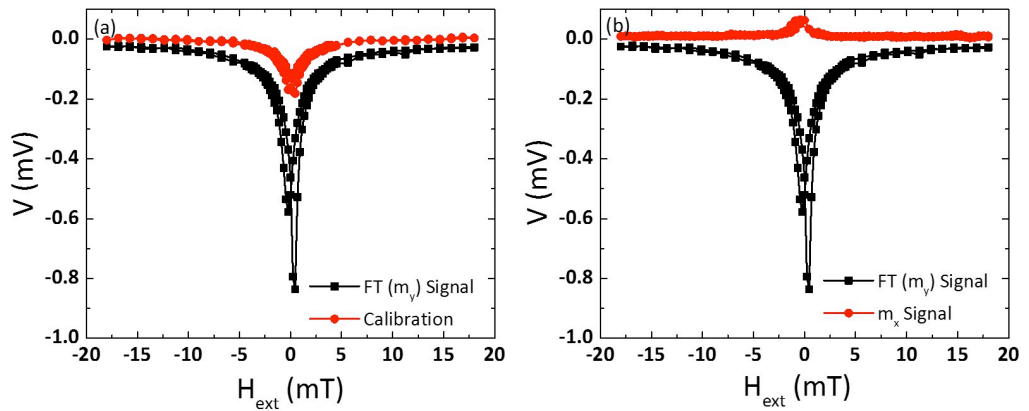


Figure 6.6: Measured voltage from the lock-in amplifier as a function of the external magnetic field for Py(8)/Pt(6) when passing an ac current (20 mA) through the sample (black squares) and an ac current (500 mA) through a wire underneath the sample (red circles). (b) Comparison of signals in two longitudinal configurations m_y (black squares) and m_x (red circles).

To further verify the accuracy of this method, we have extracted the effective spin Hall angle from FT and DT measurements for permalloy thicknesses d_{Py} from 2-10 nm and compared the results with quadratic MOKE and polar MOKE obtained without quadrant detection, respectively. As seen in Figure 6.7(a) and (b) the spin Hall angles determined from the longitudinal and polar measurements with quadrant detection agree well with the angles determined from quadratic and polar MOKE measurements without quadrant detection, respectively.

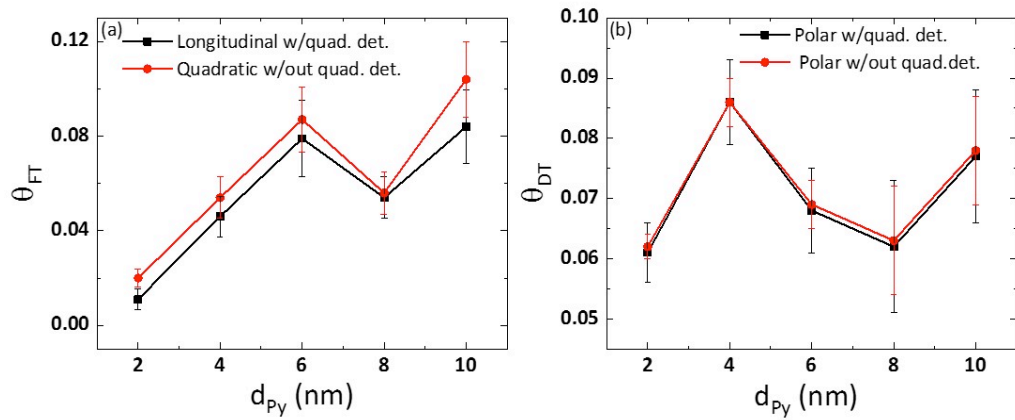


Figure 6.7: (a) Effective FT spin Hall angle measured via longitudinal with quadrant detection (black squares) and quadratic (red circles) MOKE vs. permalloy thickness d_{Py} . (b) Effective DT spin Hall angle measured with polar MOKE with quadrant detection (black squares) and polar MOKE without quadrant detection (red circles) vs. permalloy thickness d_{Py} .

6.4 Summary

We have demonstrated a convenient vector-resolved MOKE technique that can simultaneously measure the current-induced damping-like and field-like torques using normally incident light. We find quantitative agreement between the results of this technique and quadratic and polar MOKE measurements done without quadrant detection for a series of Pt/Py bilayers with different Py thicknesses. The technique

can be easily extended to measure spin-orbit torques in systems with perpendicular magnetization, as well as in systems with arbitrary magnetization direction. We anticipate this technique will be useful for further studies of current-induced magnetization reorientation in a variety of materials.

REFERENCES

- [1] X. Fan, H. Celik, J. Wu, C. Ni, K. J. Lee, V. O. Lorenz, and J. Q. Xiao, *Nat. Commun.* **5**, 1 (2014).
- [2] X. Fan, A. R. Mellnik, W. Wang, N. Reynolds, T. Wang, H. Celik, V. O. Lorenz, D. C. Ralph, and J. Q. Xiao, *Appl. Phys. Lett.* **109**, (2016).
- [3] C. Stamm, C. Murer, M. Berritta, J. Feng, M. Gabureac, P. M. Oppeneer, and P. Gambardella, *Phys. Rev. Lett.* **119**, 87203 (2017).
- [4] A. Berger and M. R. Pufall, *J. Appl. Phys.* **85**, 4583 (1999).
- [5] T. Kuschel, H. Bardenhagen, H. Wilkens, R. Schubert, J. Hamrle, J. Pištora, and J. Wollschläger, *J. Phys. D: Appl. Phys.* **44**, 265003 (2011).
- [6] H. F. Ding, S. Pütter, H. P. Oepen, and J. Kirschner, *Phys. Rev. B* **63**, 134425 (2001).
- [7] Z. J. Yang and M. R. Scheinfein, *J. Appl. Phys.* **74**, 6810 (1993).
- [8] P. S. Keatley, V. V. Kruglyak, A. Neudert, E. A. Galaktionov, R. J. Hicken, J. R. Childress, and J. A. Katine, *Phys. Rev. B* **78**, 214412 (2008).
- [9] P. Weinberger, *Philos. Mag. Lett.* **88**, 897 (2008).
- [10] K. Postava, A. Maziewski, A. Stupakiewicz, A. Wawro, L. T. Baczewski, Š. Višňovský, and T. Yamaguchi, *J. Eur. Opt. Soc. Rapid Publ.* **1**, 6017 (2006).
- [11] H. . Ding, S. Pütter, H. . Oepen, and J. Kirschner, *J. Magn. Magn. Mater.* **212**, 5 (2000).
- [12] J. Hamrle, S. Blomeier, O. Gaier, B. Hillebrands, H. Schneider, G. Jakob, K. Postava, and C. Felser, *J. Phys. D: Appl. Phys.* **40**, 1563 (2007).
- [13] K. Chen and S. Zhang, *Phys. Rev. B* **96**, 134401 (2017).

Chapter 7

CONCLUSIONS

The main concentration of this thesis is on the determination of the mechanisms of spin-orbit coupling based spin-orbit torques (SOTs) in heavy metal/ferromagnet bilayer heterostructures. An electric current generates a field-like spin-orbit torque (FT) and a damping-like spin-orbit torque (DT) on the magnetization. Based on the magneto-optic Kerr effect (MOKE), we develop a sensitive current-driven spin-orbit torque magnetometer to measure both FT and DT. The angular dependence of SOTs in heavy metal/ferromagnet/metal-oxide trilayers with perpendicular magnetic anisotropy is also quantitatively measured with MOKE.

In Chapter 3, we develop a MOKE-based SOT magnetometer to obtain the thickness dependence of DT and FT over a wide range of FM thicknesses in CoFeB/Pt bilayers with in-plane magnetic anisotropy. We observe that the DT inversely scales with the ferromagnet thickness, and the FT has a threshold effect that appears only when the ferromagnetic layer is thinner than 1 nm. Through a thickness-dependence study with an additional copper insertion layer at the interface, we identify the contributions of the spin Hall effect (SHE) and the Rashba effect to SOTs and we conclude that the dominant mechanism for the spin-orbit coupling-driven phenomena in this system is the SHE. However, there is also a distinct interface contribution, which comes from the Rashba effect.

In Chapter 4, we demonstrate that by using polar and quadratic MOKE with normal incidence light, current-driven SOTs can be detected in heavy

metal/ferromagnet bilayers. The results of this technique and ST-FMR measurements for a series of Pt/Py bilayers with different Py thicknesses agree well.

In Chapter 5, we develop a scheme to quantify the angular dependence of SOTs in heavy metal/ferromagnet/metal-oxide trilayers with perpendicular magnetic anisotropy based on the polar MOKE with field calibration.. We show that the harmonic Hall technique employed in the previous studies is inaccurate in determining the angular dependence of SOTs, particularly in the medium polar angle region ($\theta = 40 - 70^\circ$), because the fitting of the measurement curves is very sensitive to the fitting parameters like perpendicular anisotropy. The field-like torque for this sample has a larger magnitude than the damping-like torque. Both damping-like and field-like torques reach a maximum when the magnetization lies in the film plane. We observe a strong angular dependence that is different from the previous experimental observations. Based on this strong dependence, we conclude that a Rashba effect at the same interface is the dominant mechanism for the current-driven SOTs in this system.

Accurate measurements of the angular dependence of the SOTs are valuable to the study of magnetization dynamics induced by SOTs and crucial for optimizing spin-torque switching in STT-MRAM. Experiments as a function of layer thickness will be necessary to complete the study, and will require the quantification of the conductivity and other interfacial effects at the ultrathin region.

In Chapter 6, simultaneous detection of SOTs by measuring all three magnetization components m_x , m_y and m_z using a vector-resolved MOKE technique based on quadrant detection in Pt/Py bilayers over a wide range of thicknesses is presented. We compare our results with measurements using polar and quadratic MOKE without quadrant detection and find quantitative agreement between them.

The development of the spin-orbit torque magnetometer together with the Cu insertion method to isolate the interface allows quantitative determination of bulk and interface contributions in various systems. The angle dependence of DT and FT needs to be performed for further understanding of bulk and interface contributions. The vector-resolved MOKE technique can be easily extended to measure spin-orbit torques in systems with perpendicular magnetization, as well as in systems with arbitrary magnetization direction. We anticipate that MOKE magnetometry will be useful for rapid characterization of current-induced torques acting on a very wide range of materials.

Appendix A

SIGNAL OUTPUT CALCULATED USING MODIFIED REFLECTIVITIES FOR A MAGNETIC MATERIAL AND JONES MATRICES FOR OPTICAL ELEMENTS

```
(* definition of parameters:
 $\theta_0$  is the angle between the incoming beam and the surface
normal
 $\theta_1$  is the complex refractive in the magnetic material,
determined by Snell's law
x and y are in the plane of the sample, z is out of plane
 $r_{ij}$  is the ratio of the incident j-polarized electric
field and the reflected i-polarized electric field, i, j
= s, p
n0 is the index of refraction of vacuum
n1 is the index of refraction of the magnetic material
*)
Clear[n0,n1,Q]
(* define various fixed parameters *)
n0=1; (* index of refraction of vacuum *)
n1=n;
(*n1=nr+ ini; (* index of refraction of magnetic material
*)
Q=Qr+ iQi; (* magneto-optic constant of magnetic material
*)*)

(* define magnetization *)
u:={0,0,mz}; (* unit vector of magnetization, here not
normalized *)

(* reflection coefficients based on magnetic material
based on the formulae in Appl. Phys. Lett. 69 (9) 1315
(1996) *)
Clear[ $\theta_0$ , $\theta_1$ ]
rss[ $\theta_0$ _, $\theta_1$ _]:=(n0 Cos[ $\theta_0$ ]-n1 Cos[ $\theta_1$ ])/(n0 Cos[ $\theta_0$ ]+n1
Cos[ $\theta_1$ ])
rpp[ $\theta_0$ _, $\theta_1$ _]:=(n1 Cos[ $\theta_0$ ]-n0 Cos[ $\theta_1$ ])/(n1 Cos[ $\theta_0$ ]+n0
Cos[ $\theta_1$ ])-(2 i Q n1 n0 Cos[ $\theta_0$ ] Sin[ $\theta_1$ ] u[[1]])/(n1
```

```

Cos[θ0]+n0 Cos[θ1])
rps[θ0_,θ1_]:=-(i Q n0 n1 Cos[θ0] (Sin[θ1] u[[2]]-
Cos[θ1] u[[3]]))/(Cos[θ1] (n0 Cos[θ1]+n1 Cos[θ0]) (n1
Cos[θ1]+n0 Cos[θ0]))
rsp[θ0_,θ1_]:=i Q n0 n1 Cos[θ0] (Sin[θ1] u[[2]]+Cos[θ1]
u[[3]]))/(Cos[θ1] (n0 Cos[θ1]+n1 Cos[θ0]) (n1 Cos[θ1]+n0
Cos[θ0]))

(* Jones matrices *)
Clear[p,s,θ,in]
in[p_,s_]:=1/Norm[{p,s}]{p,s} (* input polarization
*)
rot[θ_]:={{Cos[θ], Sin[θ]},{-Sin[θ],Cos[θ]}}(* rotation
matrix *)
pol[θ_]:=Transpose[rot[θ]].{{1,0},{0,0}}.rot[θ] (*
polarizer *)
hwp[θ_]:=Transpose[rot[θ]].{{1,0},{0,-1}}.rot[θ] (* HWP
*)
MOKE[θ0_,θ1_]:={{rpp[θ0,θ1],rps[θ0,θ1]},{rsp[θ0,θ1],rss[θ
0,θ1]}} (* MOKE *)
field[z_]:=ComplexExpand[Abs[z]] (* function to
determine electric field of component z *)
(*
(* relation between θ0 (incident angle) and θ1 (refracted
angle) Snell's Law from Appl. Phys. Lett. 69 (9) (1996)
*)
θ1=ArcSin[n0/n1Sin[θ0]];
*)

Print["input p = 0, s = 1, hwp.MOKE.in"]
Clear[out,intp, ints,φ,φ2]
p=0; s=1; (* input polarization components *)
θ0=0; θ1=0; (* polar MOKE *)
in[p,s]
MOKE[θ0,θ1].in[p,s]
out[φ_,θ0_,θ1_]:=hwp[φ].MOKE[θ0,θ1].in[p,s] ; (* output
polarization *)
intp[φ_,θ0_,θ1_]:=field[out[φ,θ0,θ1][[1]]]^2
ints[φ_,θ0_,θ1_]:=field[out[φ,θ0,θ1][[2]]]^2
o1=out[φ,θ0,θ1]

Print["input p = 1, s = 0, hwp.MOKE.in"]

```

```

Clear[out,intp, ints]
p=1; s=0; (* input polarization components *)
θ0=0; θ1=0;(* polar MOKE *)
in[p,s]
out[φ_,θ0_,θ1_]:=hwp[φ].MOKE[θ0,θ1].in[p,s]; (* output
polarization *)
intp[φ_,θ0_,θ1_]:=field[out[φ,θ0,θ1][[1]]]^2
ints[φ_,θ0_,θ1_]:=field[out[φ,θ0,θ1][[2]]]^2
o2=out[φ,θ0,θ1]

Print["Now add HWP between BS and sample to change
polarization"]

(* Add HWP between BS and sample *)

Print["input p = 0, s = 1, hwp(π/2).hwp(π/2).in"]
Clear[out,intp, ints,φ,φ2]
p=a; s=b; (* input polarization components *)
θ0=0; θ1=0;(* polar MOKE *)
φ2=π/2;
hwp[φ2]
in[p,s]
hwp[φ2].in[p,s]
out[φ_,θ0_,θ1_]=hwp[φ2].hwp[φ2].in[p,s]; (* output
polarization *)
intp[φ_,θ0_,θ1_]:=field[out[φ,θ0,θ1][[1]]]^2
ints[φ_,θ0_,θ1_]:=field[out[φ,θ0,θ1][[2]]]^2
o2=out[φ,θ0,θ1]

Print["input p = 0, s = 1, hwp.hwp(π/2).MOKE.hwp(π/2).in"]
Clear[out,intp, ints,φ,φ2]
p=0; s=1; (* input polarization components *)
θ0=0; θ1=0; (* polar MOKE *)
φ2=π/2;
in[p,s]
hwp[φ2].in[p,s]
MOKE[θ0,θ1].hwp[φ2].in[p,s]
hwp[φ2]
hwp[φ2].MOKE[θ0,θ1].hwp[φ2].in[p,s]
out1[φ_,θ0_,θ1_]=Simplify[hwp[φ].hwp[-
φ2].MOKE[θ0,θ1].hwp[φ2].in[p,s] ];(* output polarization
*)

```

```

o1=out1[ $\phi$ , $\theta_0$ , $\theta_1$ ]
intp1[ $\phi$ _, $\theta_0$ _, $\theta_1$ _]:=field[out1[ $\phi$ , $\theta_0$ , $\theta_1$ ][[1]]]^2
ints1[ $\phi$ _, $\theta_0$ _, $\theta_1$ _]:=field[out1[ $\phi$ , $\theta_0$ , $\theta_1$ ][[2]]]^2
o1=Simplify[intp1[ $\phi$ , $\theta_0$ , $\theta_1$ ]-ints1[ $\phi$ , $\theta_0$ , $\theta_1$ ]]

Print["input p = 0, s = 1, hwp.hwp( $\pi/2$ ).MOKE.hwp( $\pi/2$ ).in"]
Clear[out,intp, ints, $\phi$ , $\phi_2$ ]
p=0; s=1; (* input polarization components *)
 $\theta_0$ =0;  $\theta_1$ =0;(* polar MOKE *)
 $\phi_2$ = $\pi/2$ ;
in[p,s]
Simplify[hwp[ $\phi_2$ ].in[p,s]]
out[ $\phi$ _, $\theta_0$ _, $\theta_1$ _]=Simplify[hwp[ $\phi$ ].hwp[-
 $\phi_2$ ].MOKE[ $\theta_0$ , $\theta_1$ ].hwp[ $\phi_2$ ].in[p,s]]; (* output polarization
*)
intp[ $\phi$ _, $\theta_0$ _, $\theta_1$ _]=field[out[ $\phi$ , $\theta_0$ , $\theta_1$ ][[1]]]^2
ints[ $\phi$ _, $\theta_0$ _, $\theta_1$ _]=field[out[ $\phi$ , $\theta_0$ , $\theta_1$ ][[2]]]^2
Simplify[intp[ $\phi$ , $\theta_0$ , $\theta_1$ ]-ints[ $\phi$ , $\theta_0$ , $\theta_1$ ]]

Print["input p = 0, s = 1, hwp.hwp( $\pi/4$ ).MOKE.hwp( $\pi/4$ ).in"]
Clear[out,intp, ints, $\phi$ , $\phi_2$ ]
p=0; s=1; (* input polarization components *)
 $\theta_0$ =0;  $\theta_1$ =0;(* polar MOKE *)
 $\phi_2$ = $\pi/4$ ;
in[p,s]
Simplify[hwp[ $\phi_2$ ].in[p,s]]
out[ $\phi$ _, $\theta_0$ _, $\theta_1$ _]=Simplify[hwp[ $\phi$ ].hwp[-
 $\phi_2$ ].MOKE[ $\theta_0$ , $\theta_1$ ].hwp[ $\phi_2$ ].in[p,s]]; (* output polarization
*)
intp[ $\phi$ _, $\theta_0$ _, $\theta_1$ _]=field[out[ $\phi$ , $\theta_0$ , $\theta_1$ ][[1]]]^2
ints[ $\phi$ _, $\theta_0$ _, $\theta_1$ _]=field[out[ $\phi$ , $\theta_0$ , $\theta_1$ ][[2]]]^2
Simplify[intp[ $\phi$ , $\theta_0$ , $\theta_1$ ]-ints[ $\phi$ , $\theta_0$ , $\theta_1$ ]]

Print["input p = 0, s = 1, hwp.hwp( $\pi/8$ ).MOKE.hwp( $\pi/8$ ).in"]
Clear[out,intp, ints, $\phi$ , $\phi_2$ ]
p=0; s=1; (* input polarization components *)
 $\theta_0$ =0;  $\theta_1$ =0;(* polar MOKE *)
 $\phi_2$ = $\pi/8$ ;
in[p,s]
Simplify[hwp[ $\phi_2$ ].in[p,s]]
out[ $\phi$ _, $\theta_0$ _, $\theta_1$ _]=Simplify[hwp[ $\phi$ ].hwp[-
 $\phi_2$ ].MOKE[ $\theta_0$ , $\theta_1$ ].hwp[ $\phi_2$ ].in[p,s]]; (* output polarization

```

```
*)  
intp[φ_,θ0_,θ1_]=field[out[φ,θ0,θ1][[1]]]^2  
ints[φ_,θ0_,θ1_]=field[out[φ,θ0,θ1][[2]]]^2  
Simplify[intp[φ,θ0,θ1]-ints[φ,θ0,θ1]]
```

Appendix B

CURRENT-INDUCED MAGNETIZATION REORIENTATION

The magnetization dynamics driven by spin-orbit interaction follows the generalized Landau-Lifshitz-Gilbert equation.

$$\frac{d\vec{m}}{dt} = -\gamma\vec{m} \times \vec{H}_{eff} + \alpha\vec{m} \times \frac{d\vec{m}}{dt} + a\vec{m} \times \vec{\sigma} + b\vec{m} \times (\vec{\sigma} \times \vec{m}) \quad (B.1)$$

where \vec{m} is the normalized magnetization vector, γ is the gyromagnetic ratio, \vec{H}_{eff} is the total effective field including the external field \vec{H}_{ex} , anisotropy field \vec{H}_a and Oersted field \vec{h}_{oe} generated from the current, α is the damping coefficient, $\vec{\sigma}$ is the spin polarization of spin current generated from charge current and is in-plane and orthogonal to the electric current, and a and b describe the field-like torque (FT) and damping-like torque (DT) induced from spin-orbit interaction, respectively. A schematic illustration of the magnetization reorientation is given in Figure B.1. For a stationary solution, the time varying term in Eq. (B.1) vanishes, leading to

$$-\vec{m} \times \left(\vec{H}_{eff} - a/\gamma \vec{\sigma} \right) + b/\gamma \vec{m} \times (\vec{\sigma} \times \vec{m}) = 0 \quad (B.2)$$

Here $(-a/\gamma \vec{\sigma})$ is the effective field of FT and $(-b/\gamma (\vec{\sigma} \times \vec{m}))$ is the effective field of DT due to SOC. The SOC-induced effective fields of FT and DT are much weaker than the applied external field. The magnetization reorientation due to the SOI can be considered as a perturbation to the magnetization that is aligned by the total effective field. It is convenient to consider the contribution of the DT term separately as a perturbation. Without the DT term, Eq. (B.2) has a trivial stationary solution that the magnetization \vec{m}_0 is aligned parallel to the total effective field $\vec{H}_{eff} - a/\gamma \vec{\sigma}$. When the

DT term is considered, one can write the magnetization reorientation as $\vec{m} = \vec{m}_0 + \Delta\vec{m}$, where $\vec{m} \cdot \Delta\vec{m} \rightarrow 0$ under the first order approximation. There will also be a change to the total effective field due to the anisotropy and demagnetizing field $\Delta\vec{H}_a = \{\Delta H_{ax}, \Delta H_{ay}, \Delta H_{az}\}$. This leads to

$$-(\vec{m}_0 + \Delta\vec{m}) \times (\vec{H}_{eff} + \Delta\vec{H}_a - a/\gamma \vec{\sigma}) + b/\gamma [(\vec{m}_0 + \Delta\vec{m}) \times (\vec{\sigma} \times (\vec{m}_0 + \Delta\vec{m}))] = 0 \quad (B.3)$$

$$\begin{aligned} & [-(\vec{m}_0 + \Delta\vec{m}) \times (\vec{H}_{eff} - a/\gamma \vec{\sigma})] - [(\vec{m}_0 + \Delta\vec{m}) \times \Delta\vec{H}_a] \\ & + b/\gamma [(\vec{m}_0 + \Delta\vec{m}) \times (\vec{\sigma} \times (\vec{m}_0 + \Delta\vec{m}))] = 0. \end{aligned} \quad (B.4)$$

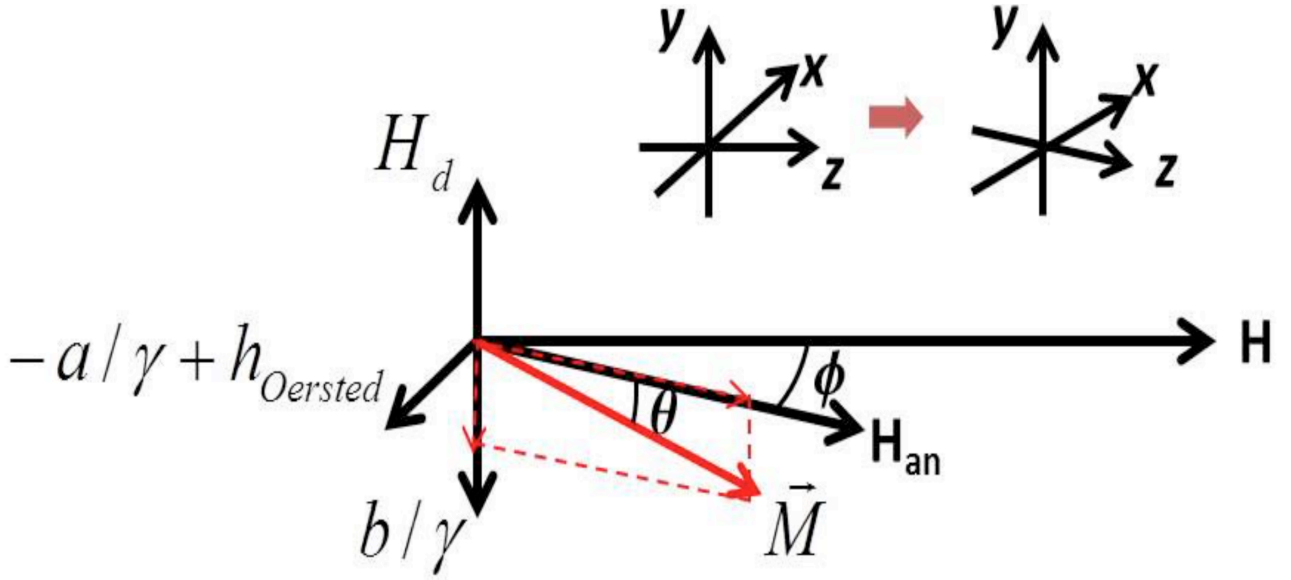


Figure B.1: Schematic of the magnetization orientation in a stationary state under an external magnetic field \vec{H}_{ex} , anisotropy field \vec{H}_a , demagnetizing field \vec{H}_d , Oersted field \vec{h}_{oe} and the effective fields of FT $(-a/\gamma \vec{\sigma})$ and DT $(-b/\gamma (\vec{\sigma} \times \vec{m}))$.

We can change the coordinates by rotating by an angle ϕ such that \vec{m}_0 and $\vec{H}_{eff} - a/\gamma \vec{\sigma}$ are in the +z direction as seen in Figure B.1. In this case, since $\vec{m}_0 \parallel (\vec{H}_{eff} - a/\gamma \vec{\sigma})$, so $[-\vec{m}_0 \times (\vec{H}_{eff} - a/\gamma \vec{\sigma})] = 0$. Then Eq. (B.4) becomes

$$\begin{aligned}
& \left[-\Delta\vec{m} \times \left(\vec{H}_{eff} - \frac{a}{\gamma} \vec{\sigma} \right) \right] - (\vec{m}_0 \times \Delta\vec{H}_a) - (\Delta\vec{m} \times \Delta\vec{H}_a) \\
& + \frac{b}{\gamma} (\vec{m}_0 \times (\vec{\sigma} \times \vec{m}_0)) + \frac{b}{\gamma} (\Delta\vec{m} \times (\vec{\sigma} \times \vec{m}_0)) \\
& + \frac{b}{\gamma} (\vec{m}_0 \times (\vec{\sigma} \times \Delta\vec{m})) + \frac{b}{\gamma} (\Delta\vec{m} \times (\vec{\sigma} \times \Delta\vec{m})) = 0.
\end{aligned} \tag{B.5}$$

Eq. (B.5) can be reconstructed by neglecting second order and higher order terms as

$$-\Delta\vec{m} \times \left(\vec{H}_{eff} - \frac{a}{\gamma} \vec{\sigma} \right) - \vec{m}_0 \times \Delta\vec{H}_a + \frac{b}{\gamma} \vec{m}_0 \times (\vec{\sigma} \times \vec{m}_0) = 0. \tag{B.6}$$

$\vec{\sigma} = \begin{pmatrix} -1 & 0 & 0 \end{pmatrix}$ is rotated by an angle ϕ and becomes

$\vec{\sigma} = \begin{pmatrix} -\cos\phi & 0 & \sin\phi \end{pmatrix}$ After defining $H = \left| \vec{H}_{eff} - \frac{a}{\gamma} \vec{\sigma} \right|$, we can expand Eq. (B.6)

into

$$\begin{aligned}
& - \begin{pmatrix} \Delta m_x & \Delta m_y & \Delta m_z \end{pmatrix} \times \vec{H} - \vec{m}_0 \times \begin{pmatrix} \Delta H_{ax} & \Delta H_{ay} & \Delta H_{az} \end{pmatrix} \\
& + \frac{b}{\gamma} \vec{m}_0 \times \left(\begin{pmatrix} -\cos\phi & 0 & \sin\phi \end{pmatrix} \times \vec{m}_0 \right) = 0.
\end{aligned} \tag{B.7}$$

The x component of this equation gives

$$H\Delta m_y - \Delta H_{ay} = \frac{b}{\gamma} \cos\phi \tag{B.8}$$

and the y component is

$$-H\Delta m_x + \Delta H_{ax} = 0. \tag{B.9}$$

Eq. (B.9) is independent of the torque term, which has a trivial solution of $\Delta m_x = 0$.

Considering a perpendicular surface anisotropy and demagnetizing field in the y-direction, ΔH_{ay} can be written as $\Delta H_{ay} = \left(\frac{2K_{\perp}}{M_s} - M_s \right) \Delta m_y$, where K_{\perp} is the effective

surface anisotropy energy. Therefore, the solution to the Eq. (B.8) is

$$\Delta m_y = \frac{b/\gamma \cos\phi}{H + M_s - 2K_{\perp}/M_s}. \tag{B.10}$$

This solution can be understood in a simple picture, in which the torque term can be viewed as an effective field in the direction of $\vec{\sigma} \times \vec{m}$, which is orthogonal to the film plane. Driven by this field, magnetization will tilt out of plane.

The derivation from Eq. (B.2) to Eq. (B.10) is done by neglecting the second order and higher order terms. Here we take more precaution in the derivation by keeping the second order term and neglecting the third order and higher order terms.

Therefore, Eq. (B.6) can be rewritten as

$$\begin{aligned}
& (-\Delta\vec{m} \times \vec{H}) - (\vec{m}_0 \times \Delta\vec{H}_a) - (\Delta\vec{m} \times \Delta\vec{H}_a) \\
& + \frac{b}{\gamma} (\vec{m}_0 \times (\vec{\sigma} \times \vec{m}_0)) \\
& + \frac{b}{\gamma} (\Delta\vec{m} \times (\vec{\sigma} \times \vec{m}_0)) \\
& + \frac{b}{\gamma} (\vec{m}_0 \times (\vec{\sigma} \times \Delta\vec{m})) = 0.
\end{aligned} \tag{B.11}$$

If we write out $\Delta\vec{m}$ and $\Delta\vec{H}_a$, we get

$$\begin{aligned}
& \left[- \begin{pmatrix} \Delta m_x & \Delta m_y & \Delta m_z \end{pmatrix} \times \vec{H} \right] - \left(\vec{m}_0 \times \begin{pmatrix} \Delta H_{ax} & \Delta H_{ay} & \Delta H_{az} \end{pmatrix} \right) \\
& - \left(\begin{pmatrix} \Delta m_x & \Delta m_y & \Delta m_z \end{pmatrix} \times \begin{pmatrix} \Delta H_{ax} & \Delta H_{ay} & \Delta H_{az} \end{pmatrix} \right) \\
& + \frac{b}{\gamma} \left(\vec{m}_0 \times \left(\begin{pmatrix} -\cos\phi & 0 & \sin\phi \end{pmatrix} \times \vec{m}_0 \right) \right) \\
& + \frac{b}{\gamma} \left(\begin{pmatrix} \Delta m_x & \Delta m_y & \Delta m_z \end{pmatrix} \times \left(\begin{pmatrix} -\cos\phi & 0 & \sin\phi \end{pmatrix} \times \vec{m}_0 \right) \right) \\
& + \frac{b}{\gamma} \left(\vec{m}_0 \times \left(\begin{pmatrix} -\cos\phi & 0 & \sin\phi \end{pmatrix} \times \begin{pmatrix} \Delta m_x & \Delta m_y & \Delta m_z \end{pmatrix} \right) \right) = 0.
\end{aligned} \tag{B.12}$$

After doing cross product multiplications and gathering x , y and z terms, we get

$$\begin{aligned}
H\Delta m_y - \Delta H_{ay} &= -\frac{b}{\gamma} \cos\phi \\
\Delta H_{ax} - \Delta m_x H &= -\frac{b}{\gamma} \Delta m_y \sin\phi \\
\Delta H_{ay} \Delta m_x - \Delta H_{ax} \Delta m_y &= \frac{b}{\gamma} \Delta m_x \cos\phi
\end{aligned} \tag{B.13}$$

The first and third equations in Eq. (B.13) lead to similar result as shown in equation (B.10). The in-plane magnetization reorientation Δm_x can be derived from the second equation in Eq. (B.13):

$$\Delta m_x = \frac{-b/\gamma}{2K_{ax}/M_s - H} \sin\phi \Delta m_y, \quad (B.14)$$

where $2K_{ax}/M_s = \Delta H_{ax}/\Delta m_x$ in a uniaxial anisotropy system. It can be understood from Eq. (B.14) that in most of cases when $b/\gamma \ll |H - 2K_{ax}/M_s|$ then $\Delta m_x \ll \Delta m_y$. When $2K_{ax}/M_s \simeq H$ is satisfied, Δm_x may be larger than Δm_y , indicating that the DT can also induce a sizable magnetization in-plane reorientation in this special situation. However, we note that the major difference between the FT induced Δm_x and the DT induced Δm_x as described by Eq. (B.14) is that the latter is quadratically proportional to the applied current. Therefore, by taking the second order transverse voltage in the experimental measurement, the contribution of DT to the in-plane magnetization reorientation is removed. Moreover, we align the easy axis of the sample along the external field direction to minimize the $2K_{ax}/M_s$ term in Eq. (B.14). We also align the current along the external field direction and carry out the analysis in the saturated regime in order to minimize $\sin\phi$ in Eq. (B.14). Based on the discussion above, we conclude that in our detection method, the first-order contribution of the DT to the in-plane magnetization is to tilt the magnetization out of the plane. Its effect on the in-plane magnetization reorientation is negligible. The in-plane magnetization reorientation that is linearly dependant on the applied current is attributed to the current-induced FT due to the SOI and the Oersted field.

The derivation above is based on the assumption that the current induced spin-orbit effective torque is small compared with the torque produced by the external magnetic field. Here we show the validity of this assumption. In a sample of

Ni₈₀Fe₂₀(2)/Pt(5), when applying a current of 50 mA through the 1 mm wide Hall bar, the current density through Pt is no more than 10^{10} A/m². Assuming the spin Hall angle of Pt is about 0.07, the DT term can be calculated as

$$\frac{b}{\gamma} = \frac{h}{4\pi e} \frac{j_c \sigma_{SH}}{\mu_0 M_s d} \approx 115 \text{ A/m}. \text{ This is equivalent to a perpendicular magnetic field with}$$

magnitude of 115 A/m applied to the film. The same current generates an Oersted field of 25 A/m. In the extraction of the current-induced effective field of FT, we consider an external magnetic field region between 2.4 kA/m and 12 kA/m, where the magnetization is well saturated. The out-of-plane magnetization reorientation angle θ

can then be calculated to be: $\frac{b}{\gamma(H_{ex} + M_{eff})} \approx 0.015^\circ$ where $\mu_0 M_{eff} = 0.55$ T is

determined by the anomalous Hall effect measurement. The in-plane magnetization reorientation angle is estimated to be $\phi = \frac{h_l}{H_{ex}} = 0.6^\circ$ with the current induced effective

field $h_l = 25$ A/m and $\phi = \frac{h_l}{H_{ex}} = 1.7^\circ$ with $h_l = 72.8$ A/m under a 2.4 kA/m external

magnetic field in the z - direction. Therefore, it is reasonable to treat the current-induced magnetization reorientation as a small perturbation.

Appendix C

USEFUL TIPS FOR MOKE MEASUREMENT SETUP

When designing a MOKE setup there are several points to be careful about. First would be the polarization state of the light. One needs to make sure that light on the sample is pure in the desired polarization. We achieve this by placing a half wave-plate and a quarter wave-plate in the optical path before the sample. The second important thing is to know where the beam hits on the sample. We use white light collimated that with the laser to obtain an optical image of the sample and the laser beam. That way by moving the sample with a 2D motion stage, we know where the beam hits the sample. Uniformity of the magnetic field is another important aspect. When placing the sample in the magnetic field, the position of the sample with respect to the magnet needs to be aligned carefully. Since the objective used and magnet is very close in the setup, a nonmagnetic objective is preferred. Optical alignment plays an important role in getting a good signal-to-noise ratio in MOKE measurements, especially in vector-resolved MOKE measurements. Light needs to pass in the middle of the optical elements and needs to be focused on the sample and collimated. For quadrant detection, mechanical stability of the quadrant detectors is also very important.

Appendix D

REPRINT PERMISSION LETTERS

Reprint permissions for chapter 3, chapter 4 and chapter 5: